KATHOLIEKE UNIVERSITEIT LEUVEN

FACULTY OF SCIENCE

DEPARTMENT OF PHYSICS AND ASTRONOMY

INSTITUTE OF ASTRONOMY

HIGH SPEED SPECTROSCOPY OF INTERMEDIATE POLARS

by

Steven Bloemen

Supervisor:	Prof. Tom Marsh, University of Warwick	Dissertation submitted to
Co-supervisors:	Dr. Roy Østensen, K.U.Leuven	obtain the degree of Master in
	Dr. Danny Steeghs, University of Warwick	Astronomy and Astrophysics

2008-2009

Acknowledgements

I consider it appropriate to start this work with words of thanks. Words of thanks to people without whose help I would never have been able to present you the text that lies under this page.

First of all, I wish to thank my supervisor and co-supervisors. Tom and Danny, this work would never have been possible without your guidance. Not only your professionalism and dedication, but certainly also your never-waning enthusiasm made it very enjoyable and enriching to work together with you. I highly appreciate that you gave me the chance to do this interesting research and to work on a publication about the findings. I'm truly convinced that you made me a better scientist. Roy, thanks a lot for the valuable discussions we had the few times that I was in Leuven and for the feedback on the draft version of this thesis.

I'd also like to express my gratitude to Prof. Keith Horne and Dr. Koji Mukai for the inspiring discussions about the intriguing nature of DQ Her.

I will never regret that I made the decision to spend my second master year abroad. I remember the moment that I went to Prof. Conny Aerts to ask her if it would be possible to spend a year in the UK. The exact location didn't really matter, no, I just wanted to go to a university where I could make a master thesis on 'something related to binary stars'. 'No problem,' she said, 'the choice is yours but I would go for Warwick'. I'm glad that I have blindly followed the advice. Once the decision was taken, I thought that it would be relatively easy to carry out the plan. At that time, I wasn't aware of the fact that Warwick is one of the top universities in the country. Consequently, getting accepted as an Erasmus student was a hassle. I owe big thanks to Conny, Roy and Prof. Jos Rogiers in Leuven and Dr. Boris Gänsicke in Warwick. They all spared no efforts to row against the flow, and that made all the difference.

My Erasmus stay in the UK was a very enriching experience. It gave me the chance to broaden my horizon, and of course to check all prejudices against the country: the endless rain showers (ever been in Belgium?), awful food (I'm afraid Alma wouldn't stand a comparative test) and undrinkable beers (they have Stella, but apart from that, true). I would like to thank the execs and members of the Erasmus society for providing due entertainment every now and then.

I have also a word of thanks for my friends. It's always dangerous to name people but I will nevertheless name a few, while the others should definitely not feel forgotten. Hans and Stijn, it is a privilege to explore countries far away (and closer, why not) together with you, to regularly meet to check whether there's something new on the Domus's beer-card and to have you as friends for life. Dries, An & Thomas, thanks for visiting me on my birthday, and Dries and Thomas for the four nice years in 'de Paus'.

I'd like to thank my fellow astronomy students in Leuven for the great time we have had in the past two years. I wasn't often around this year, but your warm welcome when I came to Leuven during the Christmas and Easter breaks made it really feel like coming home. I wish you all the best for the future and hope that we will stay in contact even though our ways are about to part.

Ilse, you are of course worth a special place in these acknowledgements as well. Living far from home can be hard sometimes, but you were always around to listen, assist, give a hug and cheer up. It was great to have your company, to share thoughts and ideas, joys and sorrows. Thanks for being a prop and stay to me, for being a great friend, my buddy.

Finally, I would like to thank my family for their continuous support. Moeke & vake, you're close to having brought me up from a baby to a Master in Astronomy. Vake, moeke, Maarten & Veerle, thank you for visiting me here on the island, for the numerous mails and calls, for adapting to my crazy plans and for missing me the whole year long.

Steven
Leamington Spa, 7 June 2009

Contents

Chapter 1

Introduction

Cataclysmic variables are close binary systems containing a white dwarf primary star that accretes matter from a Roche lobe filling secondary star. About one in four cataclysmic variables has a magnetic white dwarf (de Martino et al. 2008). Cataclysmic variables of which the white dwarf has a very strong magnetic field are called *polars*. In polars, the white dwarf spin is synchronised with the binary's orbit. In systems with moderately magnetised white dwarfs, matter is transferred from the secondary to the primary via an accretion disc. These binaries are called *intermediate polars* and don't have synchronised white dwarf spin and orbital motions.

In this work, we will study high speed spectroscopic data of two intermediate polars: DQ Her and RXJ1730. We will start with an introduction to cataclysmic variables and intermediate polars in general (Section 1.1) and to high speed spectroscopy (Section 1.2). Our efforts on DQ Her and RXJ1730 are described in detail in Chapters 2 and 3 respectively. A summary of the work and the conclusions are given in Chapter 4.

1.1 Cataclysmic variables

The majority of the stars on the sky are in reality not just single stars but multiple systems with (at least) two stars that orbit around their common centre of mass (Carroll & Ostlie 2007, Chapter 18). Binaries, i.e. systems with two components, have a special place in astrophysics because observations of their orbits are a golden key that opens the door to a variety of analysis methods that are not available for single stars. It is thus often easier to get detailed information about the characteristics of these stars.

The mutual influence of stars in a binary on each other's evolution highly depends on the type of stars involved and their separation. Most of them are far apart so that the binary components evolve as would be the case for single stars. These are called *detached* binaries.

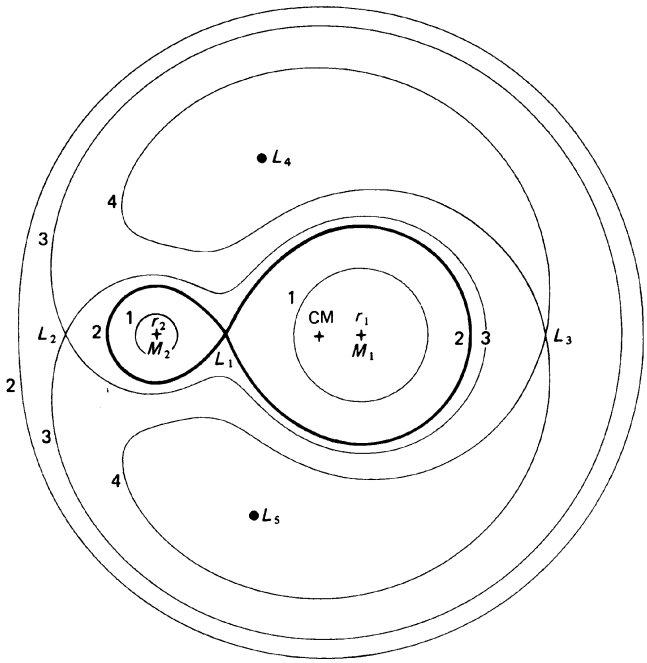

Figure 1.1: *Equipotential surfaces in the orbital plane of a binary system of two stars that are in circular orbits around their common centre of mass. The most massive star is indicated with M_1, its companion with M_2. CM is the centre of mass. The bold surface shows the Roche lobes of the two stars. If one of the stars gets bigger than its Roche lobe, it will transfer mass to the other via the first Lagrangian point L_1. Figure taken from Iben & Livio (1993).*

When the two components orbit very close to each other, a star can gravitationally deform the outer layers of its companion. The companion will then become slightly balloon-shaped. The gravitational forces of the two stars give rise to the equipotential surfaces shown in Fig. 1.1. M_1 is the most massive star, M_2 its companion. CM indicates the centre of mass. The bold equipotential surfaces of the two stars touch each other in the first Lagrangian point, L_1, and are called the Roche lobes. The evolution of such a *close binary* depends on the separation and the initial masses of the components. The star that is initially the most massive is usually called the *primary star*, the less massive star is referred to as the *secondary star* or *companion star*. Stellar evolution predicts that more massive stars have a faster evolution. If a binary is observed with one compact component (i.e. a white dwarf, neutron star or black hole, all end products of a star's evolution), this star will thus be the primary star even if it is less massive than the companion star because the faster evolution reveals that its initial mass was the highest.

The size of a star's Roche lobe depends on the masses of the two binary components and on the separation. For a separation a and a mass ratio $q = M_2/M_1$, the approximate Roche

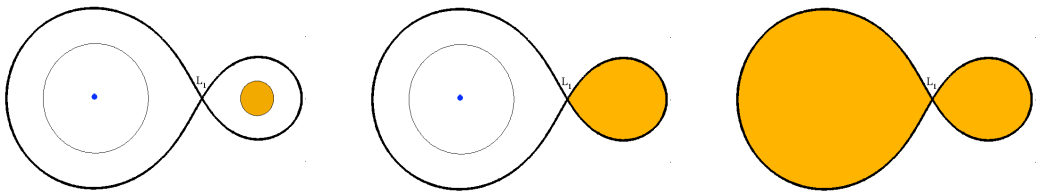

Figure 1.2: *Close binaries can be detached (left figure), semi-detached (middle) or contact binaries (right). In semi-detached binaries, the companion star (which is the left component in all three binaries shown here) fills its Roch lobe and mass flows to the primary via L_1. In a contact binary, both components fill their Roche lobes and share a common envelope.*

lobe sizes (Paczyński 1971) are $R_{L1} = a \cdot f(q)$ and $R_{L2} = a \cdot f(1/q)$ with

$$f(q) = \begin{cases} 0.38 + 0.20 \log q & \text{for } 0.3 \leq q < 20, \\ 0.462 \left(\frac{q}{1+q}\right)^{1/3} & \text{for } 0 < q < 0.3. \end{cases}$$

During the evolution of a binary, a star can fill its Roche lobe (RL) if the star expands or if the RL gets smaller due to a decreasing binary separation. If one of the stars fills its RL, mass will flow to the other star via L_1. One then speaks of a *semidetached* binary and the mass transfer is called *Roche lobe overflow*. If both stars grow larger than their RLs, the two components start sharing a common atmosphere. These systems are referred to as *contact* binaries. Figure 1.2 shows the three possible states of a close binary star. Mass transfer will alter the mass ratio q and therefore decrease the RL of the mass losing star, which helps to keep the mass transfer going. Mass transfer from main sequence stars will be unstable if $q \gtrsim 1.26$. The mass transfer will in that case be too large for the star to be able to adjust its hydrogen burning (and consequently its radius) to the new situation, the result of which is that the star will remain too large for its mass (Warner 1995, Section 9.3.1). Our work is situated in the field of semidetached binaries that have a white dwarf[1] (WD) as primary. Such a system is called a *cataclysmic variable* (CV). The RL filling secondary of a CV is a cool, late type star with a quite low mass of the order of $1 M_\odot$ (solar mass) or less.

1.1.1 Accretion via accretion discs

If the primary in a semidetached binary is small enough, as is the case for e.g. white dwarfs in CVs, the thin mass stream that originates at L_1 does not directly hit the primary's surface

[1] A white dwarf is the end product of a star with an initial mass of up to about 8 solar masses. It is a very dense object with a mass like the Sun in an Earth-like volume, composed primarily of electron-degenerate material. White dwarfs start off very hot (at temperatures of a few ten thousand Kelvin) and are then best observed in the UV.

but will go into orbit around the primary. This happens at the so called *circularisation radius*. It will form an accretion disc in the orbital plane, in which the material spreads inwards due to loss of kinetic energy by internal viscosity and outwards to ensure conservation of angular momentum. The disc formation process is depicted on Fig. 1.3. On its way to the inner part of the disc, the gas gets heated by conversion of the lost orbital energy into thermal energy. The outer disc radius is limited by the *tidal radius* at which the tidal forces of the secondary are large enough to disrupt the disc. A disc can typically extend to up to 70-90% of the RL radius (Boffin 2001).

In the disc the gas follows quasi-Keplerian orbits around the WD. In the outer regions of the disc it will orbit at a few times the binary's orbital frequency. The closer it gets to the WD the faster it will rotate. The Keplerian velocity of a particle with mass m in a disc around a star with mass M can be found by realising that it should experience a centripetal force towards the primary of $F = mv^2/r$ that is equal to the gravitational attraction by the primary $F = GMm/r^2$. This leads to the expression for the *Keplerian velocity* of a particle in a disc:

$$v_{Kep} = \sqrt{\frac{GM}{r}}.$$

The period of an orbit is $P = \frac{2\pi r}{v}$. Substituting v and generalising the equation for two masses separated by a distance a leads to Kepler's third law:

$$P_{orb}^2 = \frac{4\pi^2 a^3}{G\left(M_1 + M_2\right)}$$

which gives a relation between the orbital period P_{orb}, the masses M_1 and M_2 of the two binary components and the mean separation a, with G being the gravitational constant. Kepler's third law allows to calculate the separation of the two binary components given the masses and the orbital period. For example, the stars of a typical CV with a $0.6M_\odot$ white dwarf and a $0.3M_\odot$ companion, with an orbital period of 4 hours, would be about one million kilometers apart, which is less than one percent of the distance between the Sun and the Earth.

During a binary's evolution, angular momentum is lost from the system due to magnetic braking and gravitational wave radiation. Less angular momentum implies that the separation will decrease and the orbital period will get shorter. Mass transfer can however complicate this basic picture because angular momentum can be transferred between the spinning stars and the binary orbit.

As indicated earlier, mass that spirals inwards from the circularisation radius to the accreting object has to be accompanied by mass spreading outwards to ensure angular momentum conservation. The required angular momentum transport within the disc is one of the least understood aspects of accretion discs. Viscosity is believed to play a role, but the origin of the viscosity remains unclear. Magnetism and turbulence have been proposed as two possible responsible mechanisms. 2D hydrodynamic Roche lobe overflow simulations

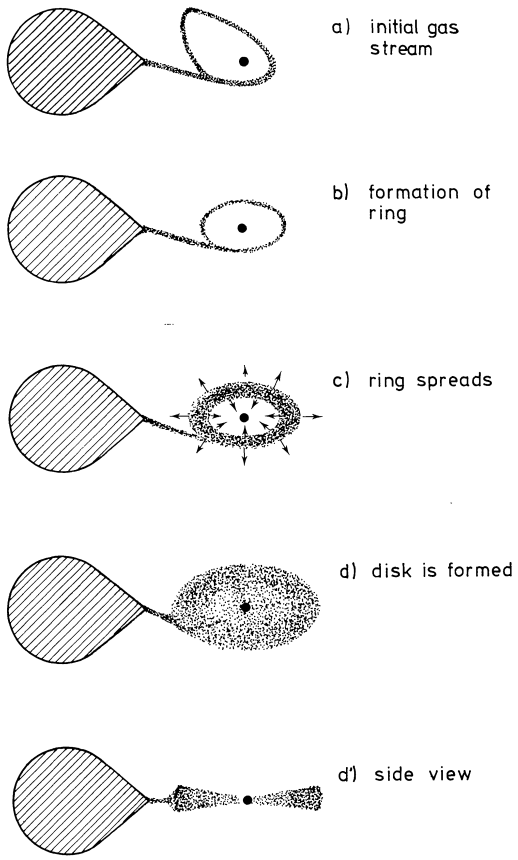

Figure 1.3: *Formation of an accretion disc in a semidetached binary with a compact primary. The secondary star on the left fills its Roche lobe and is therefore balloon-shaped. A stream of matter flows into an orbit around the primary (panel a) and circularises at the circularisation radius (panel b, the ring would be circular when viewed from above). The ring of gas spreads as matter moves inwards due to loss of kinetic energy and other particles move outwards to ensure angular momentum conservation (panel c). This way a disc is formed (panel d) which has a rather concave shape (panel d'). Figure taken from Verbunt (1982).*

by Sawada et al. (1986) however showed that tidal forces of the secondary on the outer regions of the disc can induce spiral shock waves in the disc and that these can serve as an alternative means to transfer angular momentum. Spirals have since then been established in a number of dwarf novae and nova-like CVs. We will come back to this in Section 2.3.2.

In some CVs, called *dwarf novae*, more matter is transferred than can be accreted to the white dwarf through the accretion disc. Material then piles up in the disc until it causes the disc to become unstable. At that point, the viscosity is believed to increase dramatically, supporting more matter to be accreted rapidly on the white dwarf. The result is an outburst, which is observed as a 2 to 5 magnitude difference in the light curve during a few days. After the outburst the system stays in quiescence again for a few weeks to months until enough matter is piled up to trigger a new outburst. Dwarf novae have typical accretion rates of 10^{-9} $M_\odot$/yr. *Classical novae* accrete about 10 times more material and have discs that are almost about as bright as dwarf nova discs in outburst. In these systems matter is accreted onto the WD until a thermonuclear runaway explosion occurs on its surface. Classical nova explosions repeat on a timescale of ten thousands to hundred thousands of years. Systems with an accretion rate that is a thousand times higher than that of classical novae are known as *recurrent novae* because gas is then accreted fast enough to ignite a nova explosion every few decades.

1.1.2 Magnetic CVs: polars and intermediate polars

In the majority of CVs, the magnetic field of the WD is so weak that it can be ignored, but in some cases the field is quite strong. For WDs with a high magnetic field ($B \gtrsim 10$ MG), one speaks of *polars* or *AM Herculis* stars, referring to the name of the class's prototype. In polars, torques are produced by interaction of the field with the outer envelope of the secondary. These torques synchronise the spin of the white dwarf with the orbital motion. The mass stream will almost instantly get trapped by the magnetic field lines and accretion will thus proceed without the formation of a disc. Electrons in the gas flow will spiral along the magnetic field lines and emit cyclotron radiation. The radiation is circularly polarised when observed parallel to the magnetic field lines and linearly when observed perpendicular to the field lines. This strong polarisation explains the name of the systems.

A CV with a moderately magnetised WD ($B \lesssim 10$ MG) is called an *intermediate polar* (IP) or, named to its prototype, a *DQ Herculis* star. In this case the magnetic field is not strong enough to synchronise the white dwarf spin with the binary orbit. In the past, the term IP was used for the systems with spin to orbital period ratios around 0.1 and DQ Hers for lower ratios, but since Patterson (1994) suggested that the physical nature of the systems is not really different, the two names are nowadays usually used as synonyms. Two intermediate polars, DQ Her and RXJ1730, are the subject of this work.

Since polarised light has also been observed in some IPs, the separation of the polars and

IPs is now based on the synchronisation between spin and orbital frequencies. The border between the two classes is however not totally clear, because polars have now been found with a slight asynchronism in the frequencies (Mason 2004). Since polars typically have orbital periods below 2 hours and IPs mostly have (much) longer orbital periods, it has been suggested that IPs might evolve into polars (see e.g. Norton et al. 2004). At the moment, around 35 intermediate polars and 80 polars are known[2] (Downes et al. 2006).

An overview of the characteristics of IPs can be found in the review articles Berriman (1988), Patterson (1994) and Hellier (1996). Some textbooks give a good introduction to IPs as well, e.g. Warner (1995, Chapter 7) and Hellier (2001, Chapter 9).

In IPs the magnetic field of the white dwarf is coupled to the material of the accretion disc because fields affect the motion of charged particles and orbiting charged particles generate magnetic fields. Far from the WD the energy of the interactions of the particles with the field is lower than the kinetic energy of the material in the orbit in the disc. The field is there dragged by the matter. Closer to the WD, within the Alfvén radius at which the ram pressure of the gas in the disc equals the magnetic pressure ($\rho v^2 = B^2/2\mu_0$), the field will win over the flow. This region is called the *magnetosphere*. Outside the magnetosphere, the accretion disc is comparable to the disc in a CV with a non-magnetic WD. Inside, the disc is disrupted and the matter is accreted along the field lines. The gas is there forced into corotation with the WD. Simply speaking, the spin of the WD tends to synchronize with the motion of the matter just outside the magnetosphere. A higher field strength will in general produce an IP with a longer WD spin period, because the larger magnetosphere implies synchronisation with matter in a larger, and thus slower, Keplerian orbit. The transition region (also called *threading region*) is poorly understood.

Polars are thus similar to IPs in origin, but have a WD with a magnetic field that is so high that the magnetosphere extends to or beyond the circularisation region of the disc and therefore no disc is formed.

The presence of a substantial WD magnetic field highly complicates the mass transfer process. Within the magnetosphere, the material follows the magnetic field lines on its way to the magnetic poles of the WD. The geometry of the accretion flow has been proposed to be curtain-like. An artist impression of an IP with accretion curtains in shown in Fig. 1.4. In the end, the matter falls approximately radially onto the WD. The infall velocity will then easily exceed the sound speed in the gas. A shock front will appear above the WD surface and the infalling gas will release some energy in the form of hard X-rays. Most energy however seems to bypass the shock and burrows into the white dwarf directly, thereby heating the surface (Patterson 1994). As a result, soft X-rays will be emitted from the hot spot on the pole. This is depicted in Fig. 1.5. When the magnetic axis and rotation axis of the white dwarf are not aligned, one sees an oblique rotator. The X-rays from the poles of the (rapidly) spinning white dwarf create a lighthouse beam effect and, if the axis angles are

[2]The exact number of confirmed IPs and polars depends on how much proof one desires to consider the nature of the system as confirmed.

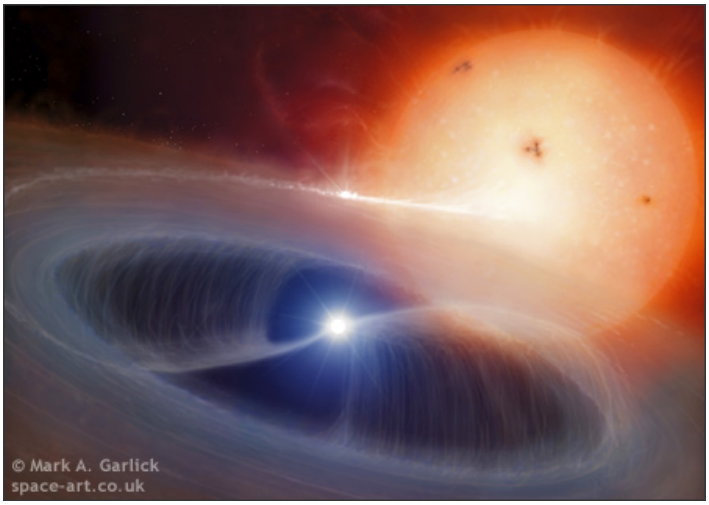

Figure 1.4: *Artist impression of an intermediate polar. The red dwarf secondary star transfers mass to the accretion disc of the white dwarf. The gas accretes from the disc onto the white dwarf along the magnetic field lines, which gives rise to so called accretion curtains. Figure used with permission of the artist, Mark A. Garlick; all rights reserved.*

favourable, the beam can illuminate the disc. A simplified sketch of an IP with lighthouse beams from the poles sweeping over the disc is shown in Fig. 1.6. The RL filling secondary star loses mass through L_1. The primary accretes the matter via an accretion disc. Where the gas stream hits the disc, a thicker structure is formed, called the *bright spot*.

Reprocessing of the X-rays in the disc is observed as pulses in the light curve of IPs. The periodicity reveals the *spin frequency* ω_{spin} of the WD and is extremely stable on short timescales, which makes its presence a good criterion to identify an IP from a light curve. If the compact object would not be a WD but a neutron star, the spin frequency would be far less stable because a neutron star has a much lower moment of inertia.

The lighthouse beam can also illuminate structures that orbit around the WD at the *orbital frequency* ω_{orb} of the binary system. Assuming that the spin is prograde to the orbit, this will result in a so called *beat frequency* in the light curve at $\omega_{beat} = \omega_{spin} - \omega_{orb}$.

Patterson (1994) lists observational criteria for CVs to be recognised as DQ Hers, since it is of course impossible to resolve these systems so accurately as to be able to see an image like Fig. 1.6. The basic criterion is (as historically developed) a highly coherent periodicity in the light curve of the CV, with a shorter period than the orbital period. Patterson (1994) presented 5 extra clues to recognise IPs. Together with the one just mentioned, this results in the following list:

- a stable optical period with $P < P_{orb}$ and usually $P << P_{orb}$;
- X-ray pulsations at the same, or very similar, period;

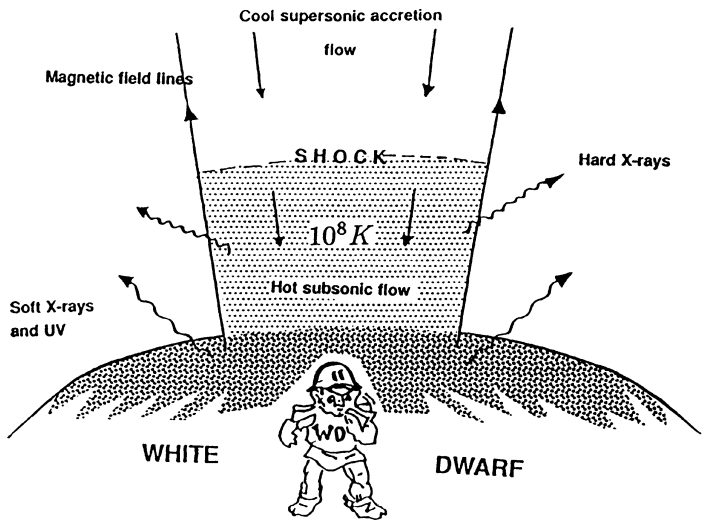

Figure 1.5: *Schematic picture of the accretion onto a magnetic pole of a white dwarf in an intermediate polar. The gas falls in radially via the magnetic field lines and encounters a shock when it gets accelerated to velocities larger than the local sound speed. It emits part of its energy in hard X-rays. These X-rays and the energy that is still in the gas after the shock heat the white dwarf surface, which starts to radiate soft X-rays and UV photons. Figure taken from Patterson (1994).*

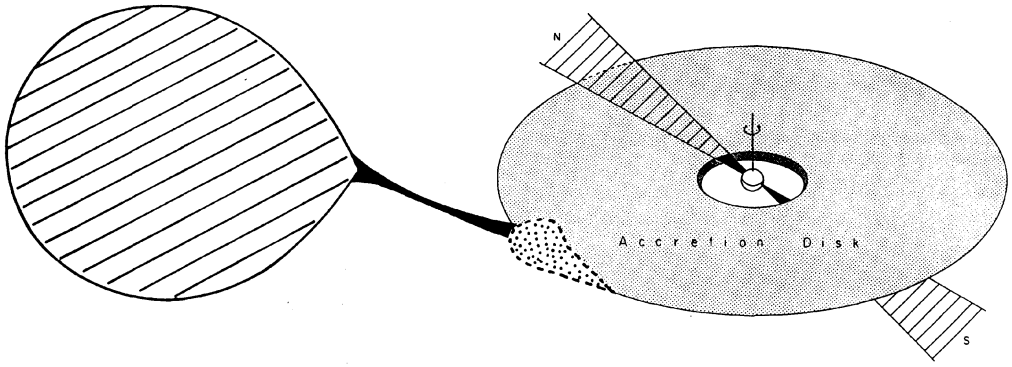

Figure 1.6: *Sketch of an intermediate polar. A late type main-sequence star (left) fills its Roche lobe and transfers mass onto a white dwarf primary star via an accretion disc (right). Where the gas stream hits the disc a blobby structure, called the bright spot, is formed. The white dwarf is moderately magnetic and disrupts the inner part of the disc. The material gets trapped by the magnetic field lines and will fall onto the white dwarf. X-rays and UV photons emerge from the magnetic poles and sweep around like lighthouse beams at the spin period of the white dwarf. Figure taken from Patterson (1994).*

- pulsations in the He II emission lines, which almost certainly arise from photoionization by the central X-ray source;
- circular polarization;
- the existence of a 'sideband period' in optical and X-ray light, usually on the low-frequency side of the main signal, e.g. at the beat frequency;
- a very hard X-ray spectrum, often with a strong signature of low-energy absorption.

Not all these criteria should be satisfied for every intermediate polar, but they give good indications that one is dealing with an IP-like system.

1.1.3 The broad picture of studying intermediate polars

Discs play an important role in astrophysics. They are for example found in quasars, in which they feed monster black holes. In quasars, the accretion discs outshine the rest of the galaxy. These systems are however the farthest objects we can see and this huge distance is a serious drawback for observations. Discs are also formed when a new star is born out of a gas and dust cloud. As in CVs, the disc then transports angular momentum away, here to allow the inner part of the cloud to collapse. In the discs around such T-Tauri stars, planets are formed as well. Unfortunately, the cloud itself hides most of this highly interesting process from our view, which creates the need to study similar discs in other astrophysical systems.

Intermediate polars, and CVs in general, are great systems to study the physics of matter transfer and (accretion) discs. They are relatively easy to observe and have many characteristics in common with the above mentioned astrophysical disc structures. As outlined earlier, vitally important processes like angular momentum transport in discs are far from understood. The same holds for the threading of the plasma-like gas in the inner disc by the magnetic field lines in polars and intermediate polars.

Another important phenomenon where cataclysmic variables come into play are supernovae of Type Ia. These are believed to be exploding white dwarfs that become more massive than the Chandrasekhar limit for electron degenerate material ($\approx 1.4 M_{\odot}$) allows. One possibility to make a white dwarf cross this border is by accretion of material from a comparison star like in a CV. Nova explosions are however believed to undo much of the mass increase by blasting most of the accreted matter into space. Another way to get a supernova of Type Ia is the merger of the two white dwarfs in a double white dwarf binary. Since Type Ia supernovae are used as standard candles in cosmology, a clearer picture of their nature is certainly desirable.

New research on magnetic and non-magnetic CVs is thus certainly justified because it will also lead to new insights in many other fields of astronomy that are more difficult to find elsewhere.

1.2 Fast optical spectroscopy of cataclysmic variables

In observational astronomy, a whole range of possibilities exist to study celestial bodies. Different chunks of the electromagnetic spectrum will reveal emission and absorption lines of a variety of elements and trace objects with different surface temperatures. Fortunately for our health, the Earth's atmosphere blocks radiation in many wavelength regimes, but this also limits our possibilities for ground-based observations. UV and X-ray studies for example are therefore performed with satellites. Among the light frequencies that do reach the surface of our planet is of course the so called *visual* light.

The most popular observing techniques performed with ground based telescopes are imaging, photometry and spectroscopy. In imaging, images of the sky are taken with CCDs, which allows for example to study the spatial structure of galaxies. In photometry, the flux of an object is measured in broad wavelength bands, to be compared with the flux in other colors or to study its variation in time. Spectroscopy is in a certain sense photometry at many wavelengths. Light from the star is dispersed, usually by a grating, and photons of many different wavelengths are collected in different pixels on a CCD. Emission and absorption lines that are present in a spectrum usually tell a lot about the nature of the system. Apart from standard spectroscopy with relatively long integration times, time-resolved is spectroscopy used to study dynamical properties of objects.

1.2.1 Spectral features of CVs

In this work high speed spectroscopic data of two intermediate polars, taken in the visual wavelength range, are studied. The most prominent spectral features of an IP, and of CVs in general, are the emission lines from the accretion disc. The disc gives rise to a double peaked line profile, as depicted in Fig. 1.7. On the left a CV is shown with a mass ratio $q = 0.15$. On the accretion disc around the white dwarf, lines of equal radial velocity[3] (RV) are drawn, assuming a Keplerian velocity profile. Material at all these positions in observed with equal Doppler shifts from below the figure. The resulting line profile is shown on the right. The shaded regions on the two figures show which parts of the disc contribute to which parts of the line. Material that is in front of or behind the white dwarf has a zero RV and therefore appears without a wavelength shift. Material in the inner regions of the disc has the highest Keplerian velocities and will thus contribute at the highest blue- and redshifted wavelengths when the material moves in the direction of the line of sight. The greater part of the disc has a moderate RV and is responsible for the two peaks.

Though the accretion disc dominates the continuum light level and the strongest emission lines, it is not the only component that can be observed. If the white dwarf is not hidden

[3]Radial velocity is the velocity component in the direction of our line of sight. This component gives rise to Doppler shifts and can thus be inferred from spectra.

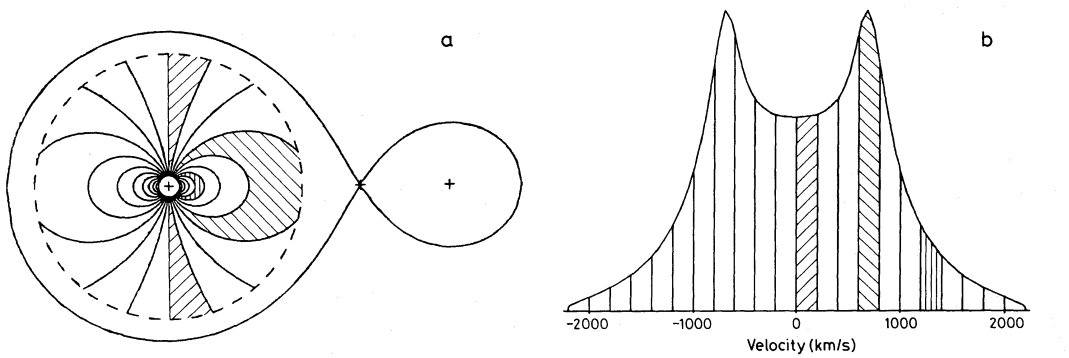

Figure 1.7: *An accretion disc gives rise to double peaked emission line profiles. In panel a, the Roche lobes of a CV with mass ratio $q = 0.15$ are shown, as well as the accretion disc around the white dwarf with lines like a dipole field that indicate locations with constant radial velocity of the disc material as observed from the bottom of the page. The radial velocities give rise to Doppler shifts, which result in the line profile shown in panel b. The shaded bins indicate the parts of the disc from which the emission originates. Figure taken from Horne & Marsh (1986).*

by the disc (which occurs at high inclinations), it will be visible as well. With a typical temperature of 15000K, Wien's displacement law (see e.g. Carroll & Ostlie 2007, Chapter 3) indicates that the white dwarf spectrum peaks in the UV:

$$\lambda_{max} \approx \frac{0.0029}{T}\,\mathrm{m} \approx 200\,\mathrm{nm}.$$

The secondary star is relatively cool with a temperature of around 4000K, and can be found at redder wavelengths:

$$\lambda_{max} \approx \frac{0.0029}{T}\,\mathrm{m} \approx 725\,\mathrm{nm}.$$

In some cases the gas stream from the first Lagrangian point to the disc can be seen as well. We will come back to this in the discussion of our own spectra.

The maximum radial velocity at which the primary star of a binary (in this case the white dwarf) is observed is usually referred to as K_1 and is equal to $V_1 \sin i$ in which V_1 is the velocity of the star in its orbit and i the inclination angle under which we observe the system. The equivalent radial velocity amplitude of the secondary star is indicated with K_2.

1.2.2 Fast spectroscopy with CCDs

When spectra are taken for e.g. abundance studies, they are usually exposed for several (tens of) minutes. In high speed spectroscopic applications, exposure times of the order of seconds or even less are used. This makes it possible to study variations in the lines on very short timescales, like for example the orbital period or the spin period of IPs which is

typically only of the order of minutes. Traditional CCDs have two major shortcomings when it comes to high speed applications. The first is that after an exposure the chip has to be read out. This can easily take of the order of a minute. It is not difficult to realise that a huge amount of precious telescope time gets lost during these overhead periods if one wants to takes many shortly integrated images. The second problem is the readout noise that is added in the conversion from the charge that is collected in each pixel to an output voltage. This noise factor is independent of the number of photons that was captured in a pixel, and thus starts to dominate when the signal is very low, as is often the case when spectra are taken with very short exposure times.

One possible solution to lower the impact of these CCD limitations is to limit the number of pixels that are used. By *windowing* the CCD, one can avoid reading out unused pixels to limit the readout time. By *binning* the CCD, pixels can be grouped such that fewer pixels have to be read out and more signal is collected per effective pixel which helps to overcome the readout noise. The drawback of binning is that it lowers the resolution of the image. Though windowing and binning can ramp up the efficiency of standard CCDs quite a lot, the result is sometimes not satisfying for high-speed spectroscopy, certainly of faint targets. Therefore more sophisticated techniques and CCDs were used for the observations presented in this work. In Chapter 2, the dead time between exposures of DQ Her is limited by the use of a clever readout strategy. In Chapter 3, RXJ1730 data are analysed that are taken with a fairly new type of CCD, a Low Light Level CCD (L3CCD), by which both the readout time and the readout noise are incredibly reduced as compared to standard CCDs. The work on RXJ1730 is therefore a bit more experimental in nature and focusses a bit more on technical aspects.

Chapter 2

DQ Herculis

The first intermediate polar we will look into is DQ Herculis. In Section 2.1, an introduction to DQ Her and an overview of relevant literature is given. In Section 2.2 our high speed spectroscopic data and the reduction process are discussed. The data are then analysed by Doppler tomography in Section 2.3 and a study of the variations in the lines in Section 2.4. In Section 2.5, we look at the peculiar nature of the Hα lines.

2.1 Introduction

DQ Her was the first intermediate polar to be discovered and was the only member of its class for about 24 years (Patterson 1994). It was studied intensively over the past fifty years but is still poorly understood. A nova outburst took place in the system in 1934. It is therefore known as 'Nova Her 1934' as well. Besides being the founding member of the DQ Herculis class, it is also the prototype of slow novae which display a dip in their decline light curve due to dust formation. After DQ Her was found to be eclipsing in the 1950s, it became a key system for understanding CVs. The binary has an orbital period of 4h39 and is viewed at an inclination $i \approx 89^\circ$ (Petterson 1980). The spin period of the white dwarf is still under debate. Most papers favour a 71s period, but some prefer a double beam at a 142s spin period.

2.1.1 Photometry and modelling of the first intermediate polar

As mentioned before, one of the observational characteristics of an IP is a very coherent periodicity in the light curve at a frequency much higher than the orbital frequency. Walker (1954, 1956) first reported a periodic 71s variation in DQ Her's light curve. Since no IPs were known at that time, the source of the periodic variations was very much debated. Walker (1958) suggested that they would be produced by radial oscillations of the white

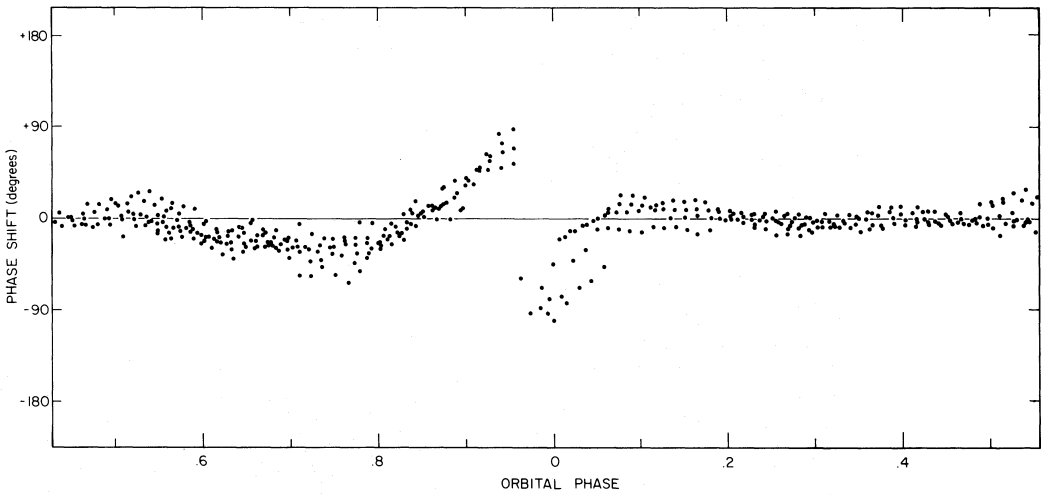

Figure 2.1: *Phase shifts in the 71s pulsation of DQ Her as found by Patterson et al. (1978). A phase shift of up to 90° is found near eclipse, which corresponds to a quarter of a 71s cycle. See text for further details.*

dwarf. From spectroscopic observations, Greenstein & Kraft (1959) concluded that a disc should be present in the system.

Further understanding came after Warner et al. (1972) reported a phase shift in the pulsations[1] during eclipse, which was later confirmed by independent studies, e.g. Patterson et al. (1978) and Zhang et al. (1995). The phase shifts are illustrated in Fig. 2.1, taken from Patterson et al. (1978). Phase shifts of up to 90 degrees are observed, which is equivalent to a time delay or advance of a fourth of a 71s spin cycle, thus about 18s. In the late 70s and early 80s, models were developed to explain these phase shifts, see e.g. Chanan et al. (1978), Chester (1979) and Petterson (1980). It was suggested that the 71s variations were produced by disc reprocessing of a beam of X-rays from the spinning white dwarf, much like our current image of intermediate polars. In this framework, the phase shifts during eclipse can be understood by considering for example the model of Petterson (1980) shown in Fig. 2.2. The six sketches depict successive orbital phases during eclipse. Imagine that we don't see the front side of the disc because this is blocked by its own thick outer rim (a disc is not flat but rather concave). Out of eclipse, the mean phase of pulse maximum of the 71s pulsation would then be when the beam points to the middle of the back side of the disc. As the disc gets eclipsed, the mean phase of pulse maximum shifts to earlier phases when the beam points to the left back side of the disc. After mid-eclipse, the pulsation shows up again with a retarded phase, because the mean phase of pulse maximum is now reached when the beam points to the right of the disc. The assumption that the

[1]In the literature the 71s periodicity in the light curve of DQ Her is often described as the 71s *pulsation*. This term can cause confusion because there is no pulsating component in the system, as is for example studied in asteroseismology. *Pulsation* here only refers to the pulses in the light curve, not to the physical source of these.

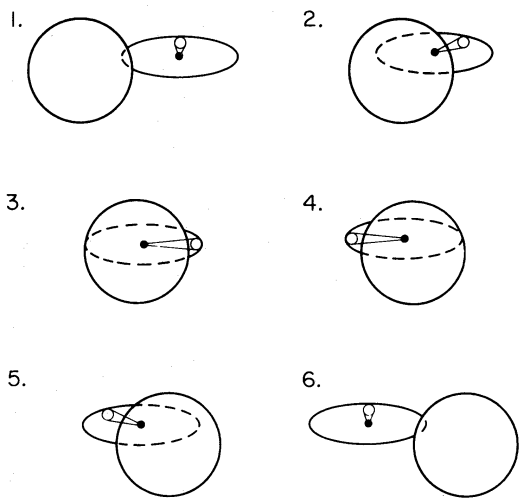

Figure 2.2: *Simple model that can account for the phase shifts in the 71s pulsation of DQ Her during eclipse. The pulsation is believed to be reprocessed light from the white dwarf's lighthouse beam on the back side of the disc. Out of eclipse (Fig. 1), the mean pulse phase occurs at the middle of the back side of the disc. As eclipse sets in, the left part of the disc becomes hidden from view, which shifts the mean pulse to earlier phases (Figs. 2 and 3). At eclipse egress, the opposite phase shift is seen as the emission of the right part of the disc is blocked (Figs. 4, 5 and 6). Phase shifts up to 90 degrees can be explained by this model. Figure taken from Petterson (1980).*

back side of the disc is seen and not the front side is inferred from the phase shifts. If only the front side of the disc would contribute, we would see the opposite phase shifts. A slightly different model presented by Chanan et al. (1978) is depicted in Fig. 2.3. It does not require the front side of the disc to be blocked from view, but only considers reprocessing of X-rays on the inner side of the disc. The result for the phase shifts during eclipse is identical.

The phase shifts out of eclipse are still not well understood. If the disc would be purely symmetrical, the only phase difference that can be present is due to light travel time differences. The radius of the primary's orbit in DQ Her is only about 1.3 light seconds (Wood et al. 2005), so another explanation has to be found.

Patterson et al. (1978) reported amplitude variations in the pulsations over the orbital cycle. The amplitude peaks around orbital phase[2] 0.2 and has a minimum around phase 0.7, which they explained by light that is being blocked by the thick bright spot on the disc

[2]For an eclipsing binary, the orbital phase is usually defined as 0 when the secondary eclipses the primary and then running up to 1 (which is the same phase as 0) with 0.5 the point when the primary eclipses the secondary. For non-eclipsing binaries, the definition can be used in a similar manner by defining 0 as the point where the secondary is closest to us and 0.5 when the primary is at our side of the binary.

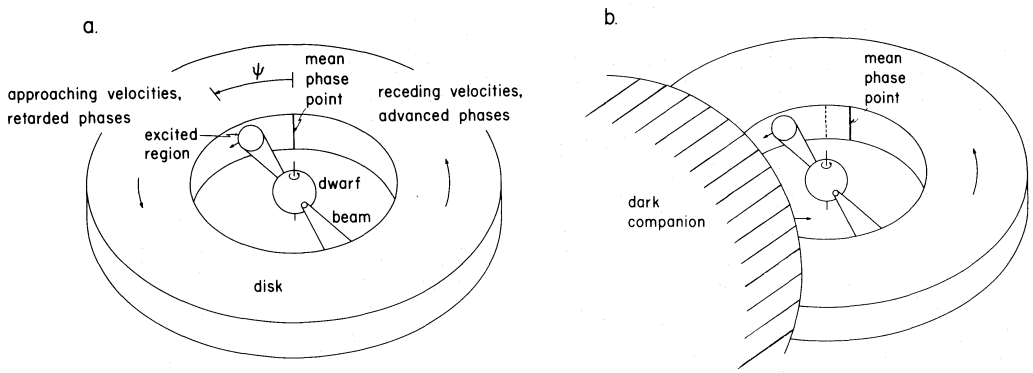

Figure 2.3: *Model to explain the phase shifts in the 71s pulsation of DQ Her during eclipse that is similar to the model presented in Fig. 2.2. In this version, the pulsation arises from reprocessed X-rays at the inner side of the accretion disc instead of at the surface. The phase shift is however explained in an analogous way. Figure taken from Chanan et al. (1978).*

when it is in our line of sight towards the white dwarf. From their multicolor photometry, they also concluded that the colors of the oscillation are approximately identical to the colors of the disc's continuum. This implies that a large part of the disc is involved, but was later contested by Zhang et al. (1995). More detailed studies of the phase shifts and amplitude variations outside eclipse were performed by e.g. Chester (1979) in an attempt to infer the rim structure from there observations by considering the amount of light certain structures would absorb. Wood et al. (2005) used smoothed particle hydrodynamical (SPH) simulations to calculate a suitable equilibrium structure of the disc that can reproduce the observations. The result is a disc with a low-density bulge (bright spot). Only the inner regions of the disc would have a direct line of sight to the white dwarf, so pulsed radiation would only come from that region.

2.1.2 Spectroscopy revolves the pulses in the spectral lines

All initial studies were done with photometric observations, which study the flux variability in broadband filters. Chanan et al. (1978) presented the first optical spectroscopy of DQ Her. They studied HeII λ4686 and discovered that it is more strongly modulated than the continuum. This can be understood by extra (photo-)ionisation of HeII by high energy photons of the WD beam, followed by electron capture and subsequent decay in which the line is produced. They report a phase shift as a function of wavelength across the line. Given the fact that the beam will first illuminate the redshifted part of the line (coming from the part of the back half of the disc that is receding from us) and then sweep to the blueshifted part (originating from the disc region that approaches us), this is not a surprise and gives extra credibility to the disc reprocessing model.

Follow-up spectroscopy by Martell et al. (1995) confirmed the phase shift with wavelength

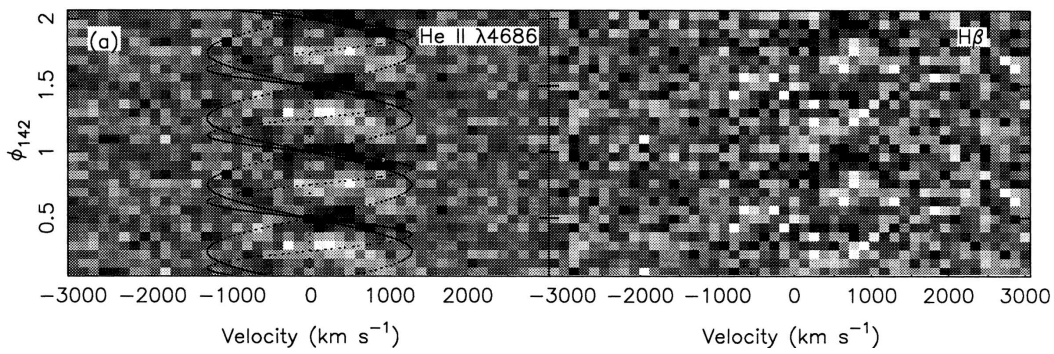

Figure 2.4: *Trailed spectra of DQ Her folded on the spin period with the mean spectrum subtracted. In the HeII* λ4686 *trail variations are clearly seen in the red wing of the line. Spectral line transitions can be triggered by UV- and X-ray photons from the lighthouse beam of the white dwarf when it sweeps over the accretion disc. The effect is seen when the beam sweeps from the side (right side on Fig. 2.3) to the middle of the back of the disc. During the next quarter of the spin cycle, the beam should illuminate blueshifted material (left back side of the disc) but this is not seen. Illumination of the front side of the disc isn't observed either. In H*β *no variations are seen above noise level. Slightly modified figure from Martell et al. (1995).*

in HeII λ4686. Their time resolution was good enough to resolve the pulsation pattern of the beam sweeping through the disc. They normalised all the spectra such that the continuum level is at 1 regardless of the spin phase, folded all the data on the spin period, averaged all spectra in 15 bins and subtracted the mean of all spectra. The result is shown in Fig. 2.4 for a wavelength region around HeII λ4686 and Hβ. Note that two spin periods are shown for clarity and that a 142s spin period was used rather than the more commonly adopted 71s. This ambiguity in the spin period will be discussed below. The HeII spin trail shows a pulsation pattern in the redshifted (positive velocities) part of the line. The sine curves that are plotted on top of the image show the predicted pattern for a 142s and a 71s period (sine with double frequency). If we keep Fig. 2.2 in mind, the pattern seems to 'show' the light beam going from the right edge of the disc (high redshift) to the middle of the back side (zero redshift). In the middle of the back side, the beam seems to disappear. It is not visible when it points to the blueshifted side (left on Fig. 2.2) of the disc, nor when it points towards the front. The absence of reprocessed light from the front side of the disc is easily understood if one looks back at the phase-shift models presented above, where the light of the front part of the disc was blocked from our view by the disc rim. The fact that no pulsations are seen in the blueshifted part of the line is not easily explained and as a matter of fact even not yet known. A rather hand-waving explanation was given by Martell et al. (1995). We will come back to this when we look at the effect in our data in Section 2.4.1.

2.1.3 UV and X-ray observations

UV spectroscopy with the Hubble Space Telescope's Faint Object Spectrograph is presented in Silber et al. (1996a,b). DQ Her shows variability in the UV that is comparable to the optical light curves. Lyα is found to pulse with a phase lag of $+0.27 \pm 0.04$ (later) relative to the continuum just before eclipse ingress. This might indicate that the true period of pulsation is slightly different from the continuum pulsation. During eclipse, the continuum drops to zero so the emitting region must be fairly compact, e.g. the disc. Lines like CIV and NV drop by only 75 % so these should partly be produced by a region that is not eclipsed when the white dwarf and its accretion disc are hidden by the secondary. HeII and SiIV stay visible as well. The same has been found in the optical, where the Balmer lines and HeII are deeply eclipsed but not completely (Martell et al. 1995).

The *mass loss rate* of the secondary is estimated to be at least 10^{-8} $M_{\odot}$/yr (Nather & Warner 1969; Patterson 1994), which is among the higher rates observed for intermediate polars. Because X-rays originate from the infall of material on the white dwarf, one expects to measure a high hard X-ray flux from DQ Her. Several X-ray studies (Cordova et al. 1981; Cordova & Mason 1984; Silber et al. 1996b) made clear that DQ Her is not the strong *hard* X-ray source it is supposed to be. This can be understood by considering the obscuration of the white dwarf by the accretion disc. Mukai et al. (2003) detected *soft* X-rays from DQ Her with the Chandra satellite, exhibiting a partial eclipse. They suggest that these soft X-rays are scattered X-rays from the WD, most likely in an accretion disc wind.

2.1.4 71s or 142s spin period?

For decades a debate has gone on as to whether the true spin period of the white dwarf is 71s or rather 142s. If reprocessed light from two magnetic poles contributes to the pulsations, a double 142s periodicity would be produced which could show up as a 71s pulsation in broad band photometry. To completely hide any 142s periodicity, the two poles would however have to be identical to a high approximation, which is physically difficult to achieve.

Kemp et al. (1974) and Swedlund et al. (1974) reported a 142s periodicity in their polarimetric data, but doubt was thrown upon the statistical significance of their claim that the 142s period was to be preferred (Patterson 1994; Zhang et al. 1995). Butters et al. (2009) present new polarimetry and also mention a 142s periodicity but once again without compelling evidence. The time resolution of their observations was not high enough and the data were too noisy to find a 71s periodicity, even if the true period would be 71s (Butters 2009, private communication).

In photometry, usually no power is found in the Fourier transform at 142s (e.g. Kiplinger & Nather 1975; Wood et al. 2005). Some photometric 142s modulation was found by Nelson (1975) and Schoembs & Rebhan (1989) but the evidence was not conclusive. The phase

shifts during eclipse can also give an indication. The observations and models presented in the late 70s and early 80s preferred a 71s period, but did not rule out a 142s period (e.g. Patterson et al. (1978)). Zhang et al. (1995) however found a better agreement with their observations for a 142s model than for a 71s model and concluded that 142s must be the true spin period. The data used were undoubtedly of good quality but one can question the validity of the model that was used, which was less elaborate than the earlier efforts.

Spectroscopy so far permitted both 71s and 142s spin periods (Chanan et al. 1978; Martell et al. 1995). The most recent insight was given by Saito & Baptista (2009), who claim to have ruled out the 142s possibility in favour of 71s by eclipse mapping of the spectra of Martell et al. (1995). Their story is even more complicated however, because they believe that the 71s period is not the spin period but the beat period (resulting from irradiation of the bright spot) which would imply a spin period of 70.8s. We will come back to this in detail in Section 2.4.2.

All things considered, the unlikeliness of having two extremely highly symmetric beams seems to be a strong enough reason not to believe the weak indications for a 142s period at the moment.

2.1.5 Stellar and orbital parameters

The most recently updated optical ephemerides are found in Wood et al. (2005). The linear *orbital ephemeris*, indicating the phase 0 points as defined earlier, was calculated using 126 eclipse timings spanning 50 years:

$$T_{min}^{orb} = HJED\ 2,434,954.94363(\pm 16) + 0.193620919(\pm 3)E$$

in which all numbers are expressed in HJED[3] and E is the eclipse cycle count. A quadratic ephemeris was published as well but the linear version was preferred by the authors. The 71s *spin ephemeris* indicating the times of maximum amplitude is:

$$\begin{aligned} T_{max}^{spin} &= HJED\ 2,439,628.771793(\pm 14) + (8.22518320 \pm 0.00000002) \cdot 10^{-4}E \\ &\quad -(2.629 \pm 0.007) \cdot 10^{-16}E^2 + (2.80 \pm 0.04) \cdot 10^{-24}E^3. \end{aligned}$$

[3]HJED stands for Heliocentric Julian Ephemeris Date. The basic calender in astronomy is the Julian Date (JD), which counts the time as a decimal number of days since 1 January, 4713 BC Greenwich noon. Reduced Julian Date (RJD) is JD-2400000. Modified Julian Date is approximately the same but starts at midnight: JD-2400000.5. Heliocentric Julian Date is JD corrected for the changing position of the Earth in the orbit around the Sun. It places the reference point in the centre of the Sun. HJD and JD can thus differ up to 8.3 minutes (the light travel time from the Sun to the Earth). Since these times are all connected with the standard UTC (Temps Universel Coordonné; Coordinated Universal Time), they suffer from incontinuities every now and then when leap seconds are introduced to keep UTC approximately synchronised with the mean solar time (UT1). HJED is the continuous version of HJD. The difference in seconds depends on the number of leap seconds introduced.

For the spin, a cubic ephemeris was used to fit the small variations in the spin period. During the evolution of a CV, the mass transfer rate $\dot{M}$ changes slightly, e.g. due to the decreasing mass of the secondary and the changes in the orbital period because of angular momentum loss. The mass loss rate influences the extent of the disc and since the spin adapts to the Kepler orbits in the region of the magnetisation radius it also triggers variations in the spin frequency.

The *distance* to DQ Her can be estimated from the size of the expanding nova shell using the parallax method. Ferland (1980) found a distance of 420 ± 100 pc. Later studies indicate slightly larger distances: Herbig & Smak (1992) found 561 ± 19 pc and Vaytet et al. (2007) estimated the distance at 525 ± 28 pc.

From radial velocities and the rotational broadening of NaI λλ8183,8195, which comes from the secondary star, Horne et al. (1993) derived the masses and the radial velocity amplitudes of the two stars: $M_1 = 0.60 \pm 0.07 M_\odot$, $M_2 = 0.40 \pm 0.05 M_\odot$, $K_1 = 140 \pm 10$ km/s and $K_2 = 227 \pm 10$ km/s.

2.1.6 Our science case

With new high speed spectroscopic data, we want to study the 71s pulsation pattern. Our data should allow to check whether the pulsation pattern in HeII λ4686 is really only visible in the redshifted part of the line, as described in Section 2.1.2 and whether this pattern is variable over the orbit of the binary. A variability over the orbit would suggest that obscuration, e.g. by disc structures, would be the reason for the absence of the pulsation in the blueshifted part of the line. Maybe we can also detect a variation in a pulse trail of other lines than HeII, which might give new insights in the structure of the system. Any new elements in the discussion on the true spin period would be welcome as well.

2.2 High speed optical spectroscopy of DQ Her

2.2.1 Observations with drift mode CCD readout

High speed optical spectroscopy was obtained during the nights of 8-10 July 1998 with the 4.2m William Herschel Telescope (WHT) of the Isaac Newton Group of Telescopes, located at the Observatorio del Roque de los Muchachos, La Palma, Spain. Approximately 3 orbital periods were observed using the Intermediate dispersion Spectrograph and Imaging System, ISIS for short. ISIS is a double-armed, medium-resolution spectrograph suitable for high speed long slit spectroscopy which saw first light in 1989. Its blue and red arms permit one to take spectra in two wavelength regimes simultaneously.

Back in 1998, ISIS was equipped with 1 megapixel CCDs on both arms. Using their full area, CCDs easily suffered dead times between two exposures of around 10s for chip clearing, shutter control, file creation and system communications. Furthermore it took tens of seconds to read out the CCD. These overhead times render high-speed spectroscopy very difficult. Time can be gained by windowing the CCD (i.e. only using a small part of the chip) or by binning (i.e. lowering the resolution by merging pixels), but speed cannot be improved as dramatically as one would want to observe phenomena that change on second to minute timescales. In addition, for exposure times of the order of one second or less, effects introduced by the relatively slow mechanical response of the shutter are non-negligible, resulting in a variable exposure across the CCD.

To allow time critical work, the WHT introduced *drift mode readout* in 1997. Instead of reading out the full or windowed CCD in one go, the readout in this mode occurs in smaller steps. During this process, the shutter remains open. In practice, one just uses a few rows of pixels, which are rapidly shifted to other, unused, areas of the chip after an exposure. Shifting the charge can be done much more rapidly than reading out the data. The next exposure can thus start without having to wait until the previous image is processed. A few exposures are in this way stored on the CCD, and readout can already start while part of the CCD is being exposed, contrary to standard CCD clearing schemes in which the next exposure only starts after the whole chip is read out. Since the chunks of data that have to be read out are much smaller because of the windowing, readouts and exposures can normally keep on going simultaneously until the data buffer of the system gets saturated. This allows for hundreds of images to be taken with a dead time of only a few tenths of a second, the exact value depending on the extent of the area of the CCD that is used and on the specialised readout mode that is chosen. The most important drawback of drift mode readout is that some smearing occurs because the image area of the CCD keeps on being illuminated whilst the previous image is vertically being shifted. Some of the object flux thus mixes with sky flux. The shorter the exposure times as compared to the readout time, the more important this effect. Of course, an enormous progress has been made in CCD design over the last decade. In Chapter 3 we will have a look at an example of a state of the art CCD with a lower noise contribution and an even faster readout.

Our dataset consists of 7392 blue spectra and 2858 simultaneously taken red spectra. The blue images are taken with the `R1200B` diffraction grating, which has 1200 lines per millimeter. They have an integration time of 5s, a spectral resolution of 1.9Å and a wavelength range of 4200-5000Å. The spectral resolution is determined by the FWHM of a gaussian fit to a strong spectral line on an arc calibration spectrum. The red spectra are made with the `R600R` grating which has 600 lines per millimeter. They are exposed for 15s, have a spectral resolution of 0.8Å and cover a wavelength range of 6320-6710Å. The deadtime between two exposures is about 0.6s. The spectra were taken with a slit width[4] of 1.5 arcseconds. The blue arm's CCD adds a readout noise of 5.6 electrons per

[4]The spectra were taken with a slit-shaped aperture on the sky. Light that falls at different positions along the slit is spread over the spatial direction of the CCD. Light at different positions along the width

Date	UT	Instrument	Grating	Exp. time	Number
08-09/07/1998	22:32 - 04:19	ISIS blue arm	R1200B	5.1s	2419
		ISIS red arm	R600R	15.1s	908
09-10/07/1998	22:48 - 05:25	ISIS blue arm	R1200B	5.1s	3181
		ISIS red arm	R600R	15.1s	1170
10-11/07/1998	00:06 - 04:35	ISIS blue arm	R1200B	5.1s	1792
		ISIS red arm	R600R	15.1s	780

Table 2.1: *Summary of our DQ Her dataset. The observations where performed with the 4.2m William Herschel Telescope operated at the Observatorio del Roque de los Muchachos, La Palma, Spain.*

pixel and has a gain[5] of 1.7. The CCD of the red arm has a readout noise of 6.3 and a gain of 1.6. An overview of the observations is given in Table 2.1. The data were stored on tapes, which nicely illustrates that ten years is as an eternity on the IT timescale. All spectra taken during one drift mode operation end up on one big image, a piece of which is shown in the left part of Figure 2.5. On the right, an enlarged segment is shown on which the spectra are clearly visible as lines running vertically over the image. The darker region around the spectra is illuminated by sky photons. Light of different wavelengths is thus dispersed over the vertical axis of the image, while light from different positions along the slit on the sky (in a 1D approximation) is separated in different pixels over the horizontal axis. The regions on the top and the bottom of the CCD are not illuminated at all. These overscan regions are called *bias regions* and will be important during the data reduction. One datafile contains of the order of a hundred spectra.

The rather small spatial extent of the frames speeds up the readout process but makes it difficult or even impossible to observe a second star in the slit. Observations of such a comparison star, which should be non-variable on the time scale of the observations, make it possible to correct for variations in the observed luminosity due to changes in the atmospheric conditions and to correct for slit losses, i.e. light that gets lost because the star is not always perfectly centered in the slit, similar to the techniques used in differential photometry. The lack of a comparison star makes it difficult to study variations in the continuum light level.

Apart from the object spectra, a lot of auxiliary images are taken that are necessary to process the data afterwards. The most important types of images that are usually taken are the following:

- *object* or *science* frames: Spectra of the object one wants to study, in this case

of the slit is (to first approximation) combined in the same pixels.

[5]The gain of a CCD expresses the number of ADU that are counted during the readout per photon that was incident on a pixel.

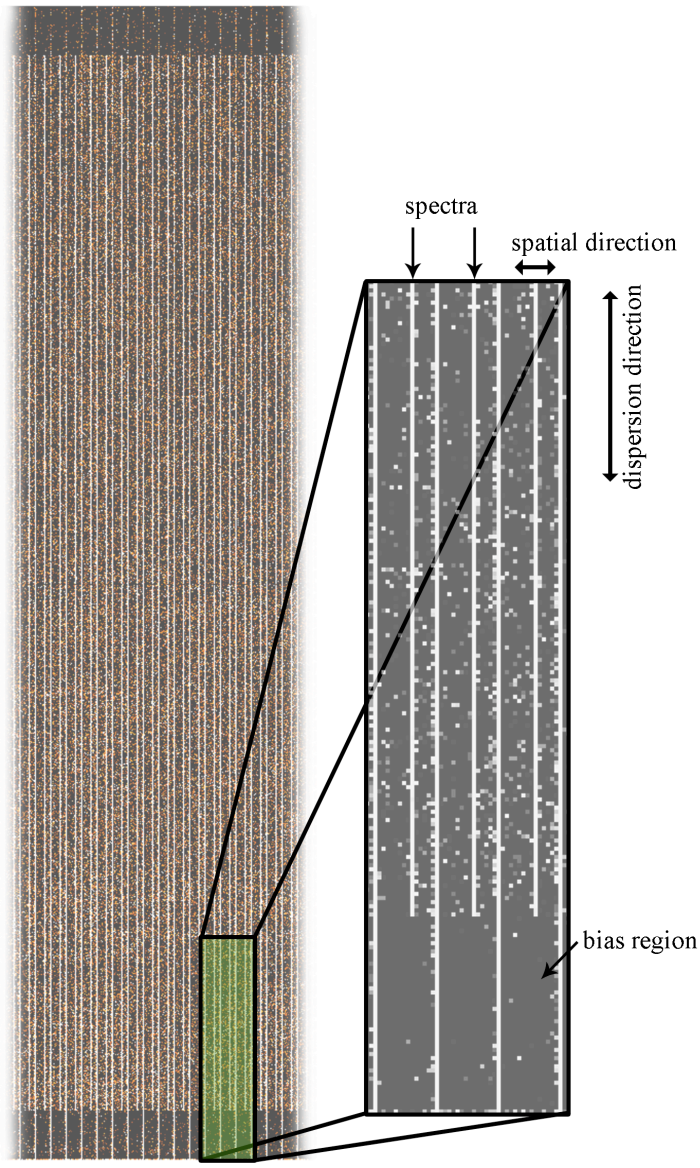

Figure 2.5: *Example of a science frame with spectra of DQ Her taken with the ISIS spectrograph at the WHT, operated in low smear drift mode. The image on the left shows a part of an image file which contains hundreds of spectra. On the right an enlarged section is shown on which three spectra can be seen. The light of different wavelengths is spread over the vertical dispersion axis. The horizontal direction represents the axis along the slit of the spectrograph and resolves light that originates from different positions in the slit, e.g. the spectrum line which comes from the star and darker regions on the left and right which are illuminated by the sky around the star. The bias or overscan regions on the top and the bottom of the spectra are not illuminated and are used to determine the zero level of the CCD.*

spectra of the intermediate polar DQ Her. These look like the example shown in Fig. 2.5.

- *flatfields*: Images of a fully illuminated CCD that are used to correct for sensitivity differences of the pixels due to e.g. the optical instruments used, the CCD construction or dust in the optical path. They are typically taken at the beginning and end of each night, and additionally whenever the telescope setup is being changed during the night, e.g. if one would replace the grating. Two types of flatfields are commonly used:
  - *lampflats*: Flats taken by pointing the telescope at a screen in the telescope dome that is illuminated by a lamp which has a more or less continuum spectrum (i.e. without spectral lines in the wavelength range under consideration). Tungsten lamps are often used to make this kind of flatfields.
  - *skyflats* or *twilight flats*: Flats taken by pointing the telescope at the sky during twilight. These have the advantage of being more uniformly illuminated along the slit than lampflats, but show the solar spectrum.
- *arcs*: Spectra of a lamp with well known spectral lines, used afterwards to find the relation between pixels on the CCD and the wavelength of the light that is dispersed on them. Since the pixel-wavelength variation changes all night long e.g. due to the movement of the telescope, arcs are usually taken about once an hour. Additional arcs are taken when a new target is chosen, at both the final position of the first star and the initial position of the next star.
- *bias* frames: Image of a non-illuminated CCD taken with zero integration time, used to determine the bias level of the CCD pixels, i.e. the value they return when no photons are captured. Biases are typically taken every night, but are often omitted when the CCD is known to have a very flat bias level because the bias level can then be determined from the small, not illuminated, overscan region(s) on each science frame.
- *dark* frames: Similar to bias frames, but taken with a non-zero integration time, used to get insight in the thermally-induced noise.

Bias and *dark* frames are not available in our dataset of DQ Her, but will be important in Chapter 3. Datafiles come in the usual `.fits` format, which is a file type that can contain multiple image data arrays and headers. The latter are lists with useful parameters like the integration time, the time the exposure started, the name of the observer and so on. Because of the peculiar nature of the frames – containing multiple spectra on one image – separate timing files were available. These are in fact just lists of the UTC times at the beginning of each exposure and have to be matched with the individual spectra during the data reduction stage.

2.2.2 Data reduction

2.2.2.1 Introduction

In the case of spectroscopic observations, the term *data reduction* embraces all actions that are required to extract a one-dimensional spectrum from each two-dimensional image as observed at the telescope, with propagation of errors. Basically, we thus want to transform a 2D image into a table with wavelengths and corresponding observed fluxes plus an error estimate for all these flux values. This procedure is further explained in the following sections. In brief, it kicks off with manipulating the 2D image: the bias level has to be removed (since these counts in the pixels do not result from photons) and a correction for the response of the CCD pixels has to be made by dividing the image through a normalised flatfield. Next, the region containing the object light (the spectrum trace) has to be defined and the sky around the trace has to be interpolated across the object region to allow the sky background to be subtracted. One-dimensional spectra can then be extracted along the defined trace. Apart from the science frames, also the arcs have to be extracted. Then, a wavelength scale can be determined on the arc spectra by assigning wavelengths to the observed spectral lines, through comparison with template spectra of the same type of lamp, and by fitting a polynomial wavelength scale to these. Linear interpolation between arcs bracketing the spectra then allows to define the wavelength scales of the science spectra. Unfortunately, no comparison star and flux calibration stars are available in the dataset we consider here, so we will end up with a spectrum in electron or photon counts rather than in flux units. For information on a flux calibration procedure, I refer to Chapter 3.

2.2.2.2 Reduction software

The software packages and applications `STARLINK` (containing `FIGARO` and `KAPPA`), `PAMELA`, `MOLLY` and `PYTHON` have been used intensively for the data reduction.

`STARLINK`[6] is a suite of data reduction packages that has been developed in the UK between 1979 and 2005 by a group of astronomers, spread over more than 30 universities. Since 2006, the software has been maintained by the Joint Astronomy Centre in Hawaï. The suite includes `KAPPA`, a collection of tools to process images and to manipulate data files, and `FIGARO`, a package for data reduction that is mostly renowned for spectroscopic applications.

`PAMELA` and `MOLLY`[7] are developed by Tom Marsh to reduce and analyse spectroscopic data in conjunction with the above mentioned `STARLINK` software. The aim of `PAMELA` is to reduce 2D spectra to 1D spectra with full propagation of errors. It implements the optimal

[6] `STARLINK` can be obtained from `http://starlink.jach.hawaii.edu/starlink`.

[7] `PAMELA` and `MOLLY` are available for download at `http://deneb.astro.warwick.ac.uk/phsaap/software/`

extraction method presented in Horne (1986) and the revised version of Marsh (1989) for tilted or curved spectra. MOLLY is a program for analysis of 1D spectra, specialised in handling large numbers of spectra and more specifically time series of spectra.

PYTHON is a high-level programming language that is rapidly gaining popularity these days in the astronomical community. During the preprocessing of the rather peculiarly formatted low smear drift spectra, the pyfits module was used to load, manipulate and save the raw data files, together with numpy which is intended to perform calculations on data arrays.

2.2.2.3 Manipulation of 2D files

Since all standard reduction software expects to find one object spectrum per datafile, the large frames (as shown in 2.5) were first cut into individual spectrum files using PYTHON. At this point, the timings were taken from the separate timing lists and added to the headers of the single spectra files. Because the drift mode was still in an experimental phase at the time of the observations, several header problems had to be fixed, including missing timings in the timing files. Once this hurdle was cleared, the images were converted from .fits to STARLINK's *.sdf* format and the dataset was split into different groups. Spectra of the blue and red arm, of different nights and with different dimensions (window and binning parameters) were separated. The binning and the number of pixels in the spatial direction were varied during the observations, which is a complicating factor when one tries to set up an automated reduction procedure. Because the twilight flats taken during the third night had different binning and windowing parameters than the science frames of that night, the flatfields were rebinned and sliced to the right dimensions whilst making sure that the same pixels on the chip were retained as were used for the science images. In the further reduction steps, these groups of files will always be treated separately, i.e. the reduction parameters are tweaked for these groups individually.

The arc spectra deserve an extra preparation step in their PYTHON script. Arc spectra are typically taken every hour or so, this way bracketing the science frames to be able to determine the wavelength scale of a science spectrum by linear interpolation between two arcs. The arcs are taken in drift mode as well. Sometimes, just one arc exposure was made. In that case, we just retain this image. When however two or more arcs are taken, we can do a better job than just choosing one. As well as science images and twilight flats, arcs can suffer from cosmic ray hits. Cosmic rays are highly energetic particles (mostly protons from the Sun) that hit the CCDs from time to time and thereby cause extremely high counts (up to saturation) in a few pixels. With more than one arc at hand, one is able to detect these cosmic hits by doing a pixel by pixel comparison of all the available arcs. When at least 3 arcs are available, it is safe to adopt a median image as the final arc. A cosmic hit on one of the images will then easily be rejected because 2 or more other frames have a normal pixel value, thus dominating the median. When exactly 2 arcs are available, one can use

the lowest pixel counts (to reject the higher pixel value that can possibly be a cosmic ray), but a better decision can be made on a statistical basis. A mean image was taken instead of a median image, except for pixels of which the highest value of the two arcs exceeded the mean by more than $4\sigma = 4\sqrt{\sigma_1^2 + \sigma_2^2}$, with $\sigma_i^2 = \left(\frac{RN}{G}\right)^2 + \frac{arc_i - bias}{G}$ in which RN is the readout noise of the CCD, G the gain of the detector, arc_i the pixel value of the first or second arc and $bias$ the bias level determined from the overscan regions.

The twilight and lamp flats were also combined into single images of the highest possible quality by taking a median of the flats available per group of images (i.e. nights and different dimensions separated). This time, a scaled median was used, in which all flats were scaled to the same average pixel value as the first in the series, because the average illumination level of individual flats can be different, e.g. of two flats taken after each other on the sky during sunrise.

2.2.2.4 Debiassing

Normally, all images should then be debiassed by subtracting a bias image to correct for pixel to pixel differences and consequently adding or subtracting a constant, determined by taking the mean of the pixel values in the overscan regions of each frame, so that the median overscan pixel ends up at 0. This way, we get rid of the electrons that are counted but that do not originate from photons. The remaining pixel values thus correspond, at least within the errors, to real photon events. There are however no bias images available in the dataset, but the bias levels of the CCDs used for these observations are known to have a quite flat bias level. We therefore only subtracted the constant from each frame, which is common practice nowadays for good quality CCDs.

2.2.2.5 Flatfielding

The next step is to create a master flatfield, again for all groups of files separately. Skyflats are taken on the sky and are considered to have a flat illumination profile in the spatial direction, because the small piece of sky the telescope is pointed at is equally bright all over. We thus want to use the spatial profile we observe in skyflats (only flat in an ideal case, not with a real detector) to correct object images. To adjust for pixel to pixel variations in sensitivity of the CCD we rely on lamp flats, because skyflats contain spectral lines of the atmosphere, whilst the tungsten lamps used for lamp flats don't have spectral features. These lamp flats are however not expected to have a flat illumination in spatial direction. Moreover, a lamp illumination shows a (featureless) blackbody-ish profile in dispersion direction, not at all a flat profile.

We therefore use a median tungsten flat W and a median twilight (sky) flat T, both created as described for the arcs in Section 2.2.2.3. We collapse W on the spatial axis to get a 1D

frame that basically shows the spatial profile of W, and we remove the spatial profile from W by dividing W through this 1D frame, to get W'. Then, we make a 1D frame of the spatial profile of T by collapsing T on the spatial axis and we multiply W' by this profile to create a flatfield W''. Collapsing W'' on the dispersion axis gives us a flatfieldspectrum S. We fit a polynomial (3rd order in this case) to S, and divide W'' by this fit to remove the variations in the flux of the lamp (the blackbody-profile) on large wavelength scales, to be left with W''' which contains pixel to pixel variations in the wavelength direction and the spatial profile of the twilight flats in the spatial direction. Finally we rescale W''' so that it has a mean value of 1 and we invert the image to produce the so called *balance* frame. During the further reduction process, every arc and object frame will be multiplied by this balance frame to correct for the large scale spatial profile variations and for the pixel to pixel sensitivity variations of the CCDs. The corrections that are applied to the pixel values typically amount to a few percent.

2.2.2.6 Extraction of 1D spectra

All spectra are then extracted (i.e. a 1D version is made from the 2D frame) by using `PAMELA` commands. If the spectrum is not properly aligned with the pixel columns of the CCD, i.e. if it is tilted or curved, then we start off by determining the trace of the spectrum by fitting a polynomial to it. The `track` routine is built for this purpose. For the current dataset it turns out to be redundant but this procedure will be used in Chapter 3.

The second step is to determine the columns of the CCD that contain the pixels that are illuminated by the star (the *object region*), and neighbouring columns (preferably regions at both sides of the spectrum) that contain just sky illumination (the *sky regions*). This is done with the `regpic` script.

The sky regions are then used to calculate the sky background level in the object region. Only the flux above this level will be considered as coming from the star. The background illumination comes from, among others, the Sun and the Moon, aurorae, light pollution and unresolved astronomical background objects. The interpolation is done by fitting a low order polynomial to the skyregions, for every row of pixels separately, with `skyfit`. Only the sky pixels with a value below a reasonable threshold were used, because cosmic hits can cause spurious high values which could not be excluded as usual on statistical basis due to the very small number of sky pixels in the narrow sky regions around the spectrum. Because skylines – which are produced by atoms and molecules in the atmosphere like OI and OH – are equally present in the sky and in the object region, their contribution to the object's spectrum will be interpolated quite accurately and therefore removed from the final spectrum.

The last step is the actual reduction. A first way to do this is the so called *normal extraction*, in which the flux in all columns of the object region is summed per row of pixels, with the routine `extnor`. A more intelligent way is given by the *optimal extraction* algorithm

implemented in `optext`. In optimal extraction, developed by Horne (1986), the simple sum over the spatial profile is replaced by a weighted sum, in which the weight of each column is equal to the the ratio of its signal to its variance. The weighting profile is calculated by fitting a low order polynomial to the values of each pixel column. In the iterative fitting procedure, pixels that differ too much (typically by more than a few tens times σ) from the fit are rejected. This way, cosmic hits can be easily recognised and masked. Extractions were done using both methods in order to be able to check the result of the optimal extraction by comparison with the normally extracted spectrum.

As soon as the above processes are well set up, the only step that still requires human interaction is the identification of the sky and object regions. The position of the star in the slit of the telescope is not perfectly constant, which causes the spectrum to drift over the spatial axis of the CCD. The region identification step is however also automated by automatic determination of the shift of the spectrum location in spatial direction, and shifting the manually determined regions accordingly. This is done with the routine `skymov`.

2.2.2.7 Wavelength calibration

Once the 1D spectra were extracted, the spectra were read into `MOLLY` and a heliocentric correction was applied to the timings to correct for the light travel time differences due to our motion around the Sun. Next, the pixel scale had to be linked to a wavelength scale, since we want to know the wavelength of the light that has been collected in every pixel as accurately as possible. To this end, spectra were taken from a calibration lamp, in our case a copper-neon lamp. These *arc* spectra have a well known pattern of lines. Since there is usually a drift in the wavelength scale during the night because of movements of the telescope while it is following the motion of the star, new arc spectra are typically taken every hour. The pixel-wavelength relation also varies at different locations on the chip and thus depends on the extract position (the trace) of the extracted object spectrum. Therefore, calibration spectra have to be extracted for each object spectrum independently, using the same pixel columns (in this case) or spectrum trace (in Chapter 3), from the arcs that were taken the closest in time before and after the object frame.

With the extracted arc and science spectra at hand, the actual wavelength calibration can be done using `MOLLY`. By comparison of the observed arc spectrum with template spectra, one can determine the wavelength of a certain number of pixels at which clear lines are observed that can be matched with peaks on the template. By fitting a polynomial relation to those pixel-wavelength pairs, a wavelength calibration for the whole pixel range can be interpolated and extrapolated. This process of matching observed lines with template lines is an iterative process. One usually starts off by assigning a wavelength value to a small number (say, about 5) of the highest peaks. Fitting a first or second order polynomial then leads to an estimate of the pixel-wavelength relation, which helps to identify weaker lines.

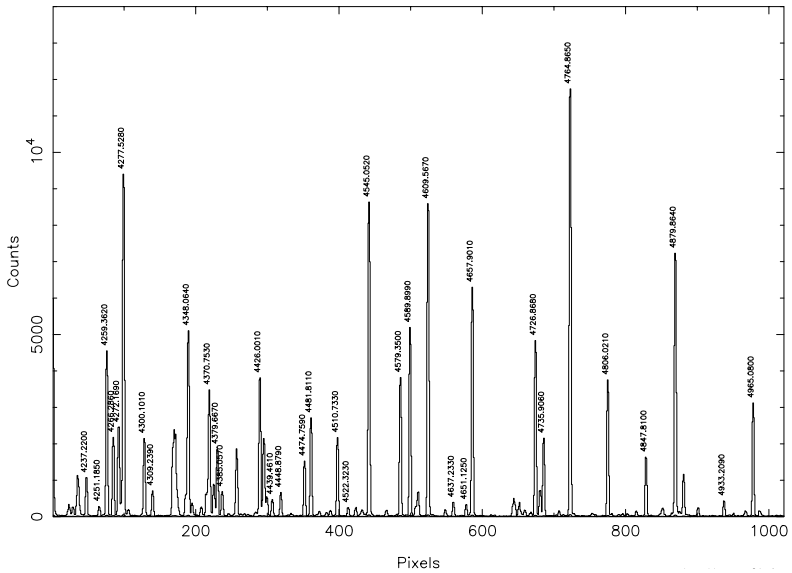

Figure 2.6: *Example of an arc spectrum of a He-Ne-Ar lamp taken with the blue arm of ISIS. By identifying as many non-blended lines as possible, one can define a polynomial relation between the pixel number of the spectrum and the wavelength of the photons. This plot is made within* `MOLLY` *during the wavelength calibration.*

Erroneous matches are possible of course, but they are usually easily identified because of their large deviation from the wavelength determined from a fit to a large number of correct lines. The software offers the possibility to assign a larger weight to stronger lines such that weaker lines can be safely included in the fit, without giving these noisier lines too much influence. Let us for example consider the blue arcs. Fig. 2.6 shows a blue arc spectrum with 34 identified line wavelengths. A typical fourth order polynomial fit to the identified lines is shown in Fig. 2.7. The uncertainty on the wavelength scale is less than 0.02Å. This error range is – as it should be – negligible as compared to the spectral resolution (1.9Å) of the spectra. As soon as all arc spectra are wavelength calibrated, one is ready to calibrate the object frames. This is done by linear interpolation of the wavelength scales of the arc spectra taken before and after each object spectrum, to account for the arc drift. That this drift can be really substantial is illustrated in Fig. 2.8. On the plot, the wavelength drift is shown for the blue spectra of the second night. A drift of up to 1Å is present.

2.2.3 Discussion of the extracted spectra and trails

On Figures 2.9 and 2.10 an example of a fully extracted blue and red spectrum are shown. The spectrum is shown in green, the error estimates in red. The blue spectra have a signal to noise (S/N) ratio of around 3, the red have a S/N of approximately 6. Figures 2.11 and 2.12 show the average spectra for each wavelength range. The spectral lines that are

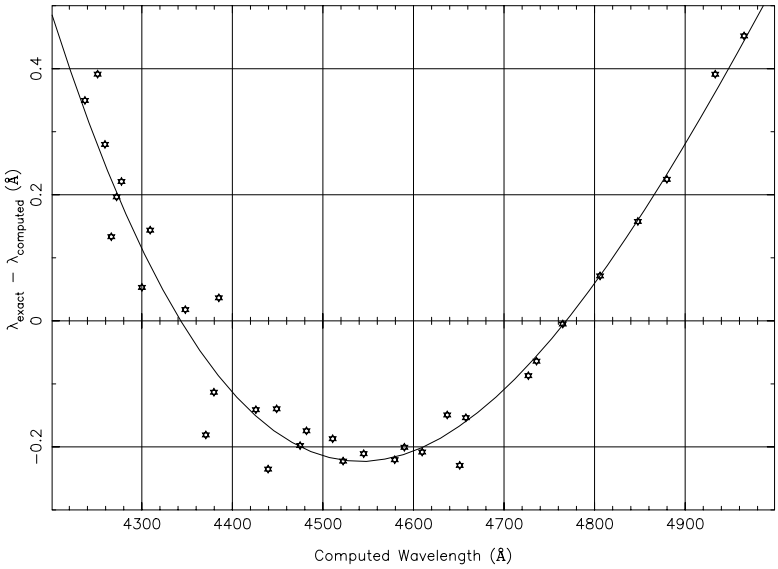

Figure 2.7: *Fourth order polynomial fit to the pixel-wavelength relation of the arc spectrum shown in Fig. 2.6. This plot is made within* `MOLLY`*. The first order term has been subtracted.*

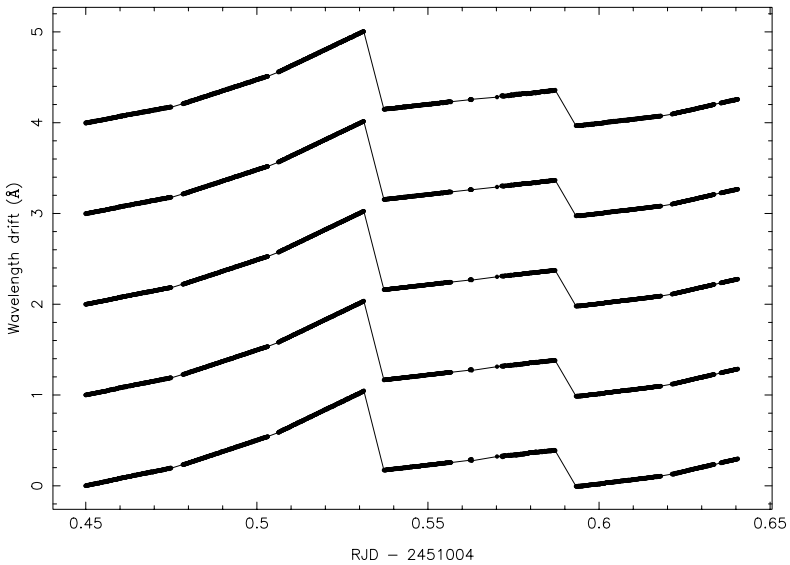

Figure 2.8: *Drift of the wavelength calibration relation on the blue arm spectra during the second night of our observations. On the horizontal axis the time of the spectra is shown in days. On the vertical axis the drift is indicated in angstroms. The wavelength scales of science frames are interpolated between the wavelength relations of two surrounding arc frames, which results in the partially linear behaviour of the drift plot. The smooth drift results from slight changes in the optical path due to movement of the telescope. Substantial jumps are due to changes in the telescope setup.*

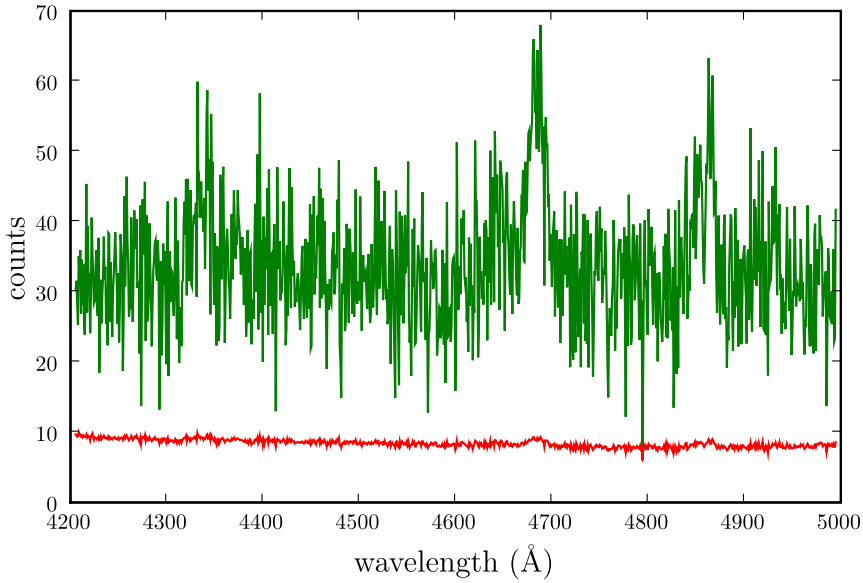

Figure 2.9: *Example of a fully extracted and wavelength calibrated spectrum of DQ Her taken with the blue arm of ISIS. The spectrum is shown in green, the error estimates in red. The exposure time is 5s and the resulting S/N in the continuum about 3.*

visible are listed in Table 2.2.

Because there was no non-variable comparison star in the slit, we could not correct for variability in the sky conditions (seeing) and the position of the star in the slit (slitlosses) during the observations. The number of counts in the continuum of the spectra thus exhibits fluctuations that do not originate from the star. The spectra have therefore been normalised by subtracting a low order polynomial fit to the continuum regions. It is common practice, e.g. in abundance studies, to normalise spectra by dividing through a fit instead of subtracting. By using a subtraction, we do remove all instrumental and conditional effects from the continuum and lines, as well as continuum variability that is characteristic for the star itself, but we manage to leave the star's intrinsic effects on the line shapes and strengths untouched. From here on only the continuum subtracted spectra will be used in this chapter.

Due to the orbital motion of the binary system, lines of both the WD-accretion disc system and the donor star are broadened by Doppler shifts. When a component is receding its light gets redshifted, when a component is approaching us its light shows up blueshifted. On an average spectrum, all orbital phases are combined which results in smearing of the lines. Figures 2.13 and 2.14 show trails of all the (normalised) spectra, which show the variations of the lines in time. Keep in mind that these trails show all spectra of the three nights just on top of each other. The lines are mostly produced in the accretion disc. Therefore they will disappear during eclipse, which is clearly visible on the trails, e.g. on Fig. 2.13 around spectra 1500, 3900 and 6000.

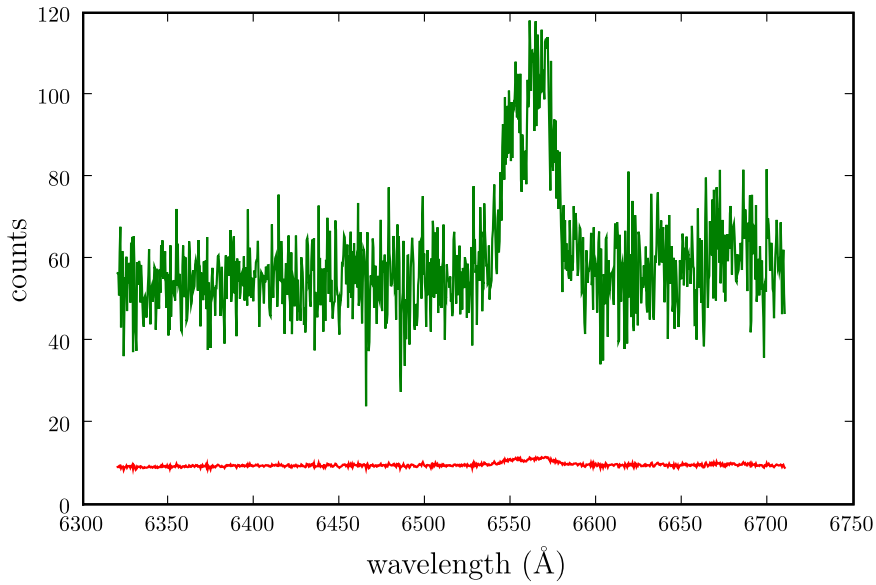

Figure 2.10: *Example of a fully extracted and wavelength calibrated spectrum of DQ Her taken with the red arm of ISIS. The spectrum is shown in green, the error estimates in red. The exposure time is 15s and the resulting S/N in the continuum about 6.*

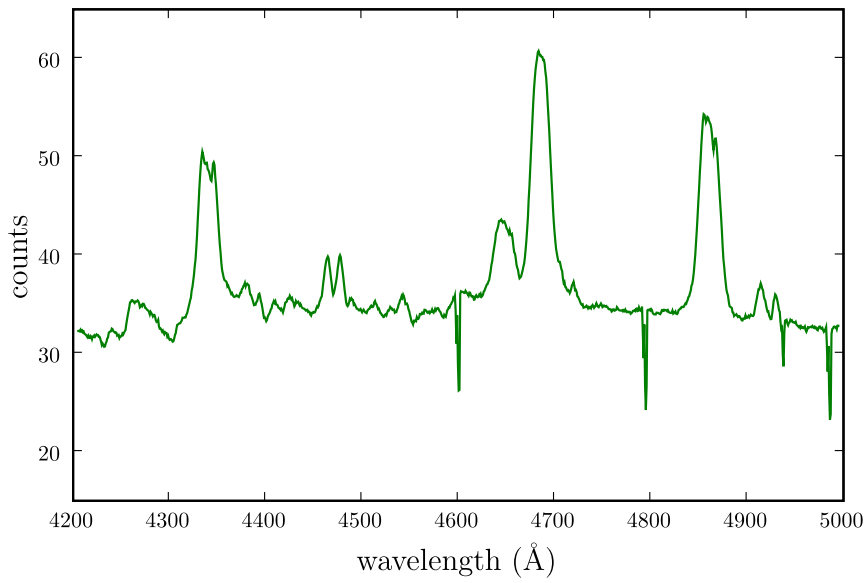

Figure 2.11: *Average blue arm spectrum of DQ Her. The most important spectral lines are listed in Table 2.2. The absorption features around 4600Å, 4800Å and 4990Å are not real but arise from bad CCD columns. The double peaked line profile that is expected from an accretion disc is smeared out because spectra from all over the orbital period were averaged without correcting for the radial velocity of the WD and accretion disc.*

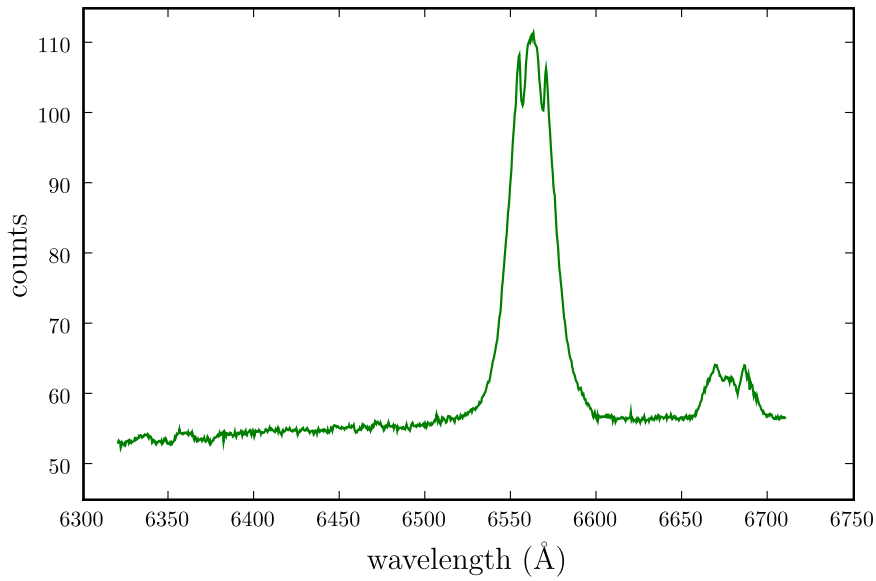

Figure 2.12: *Average red arm spectrum of DQ Her. The two spectral lines that can be seen are Hα λ6563 and HeI λ6678. The triple peaked nature of the Hα line is peculiar. We believe that the outer peaks are caused by extra line emission from the nova shell, see Section 2.5 for a detailed discussion.*

ISIS arm	Source	Wavelength (Å)
blue	CII	4267.261
	Hγ	4340.465
	HeI	4387.928
	HeI	4471.681
	HeII	4541.7
	Bowen blend	≈4640
	HeII	4685.750
	HeI	4713.20
	Hβ	4861.327
	HeI	4921.929
red	Hα	6562.760
	HeI	6678.149

Table 2.2: *Spectral lines in the spectra taken with the ISIS blue and red arms. The Bowen blend is composed of NIII at 4634.12Å, NIII at 4640.64Å and CIII at 4651.35Å.*

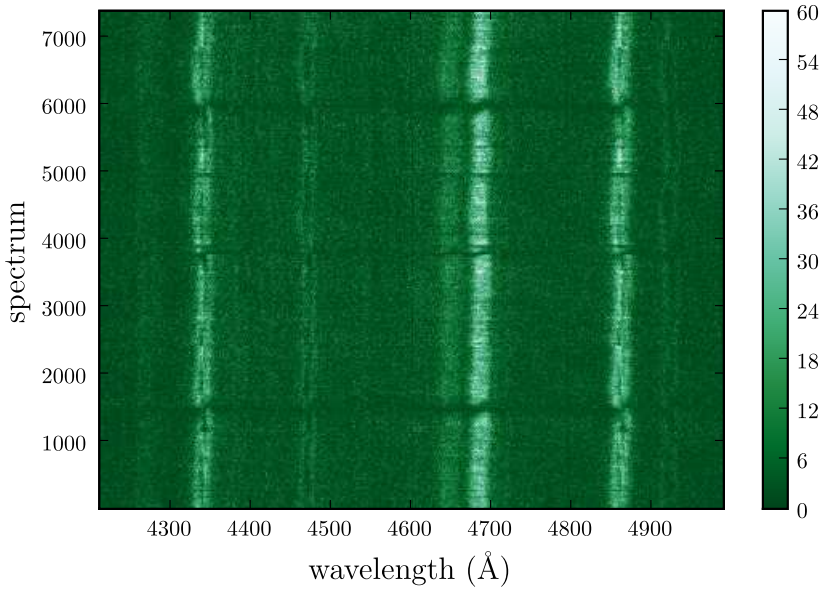

Figure 2.13: *Trail of all normalised blue arm spectra of DQ Her taken during three nights. Eclipses are seen around spectra 1500, 3900, 6000. The spectral lines that are seen are listed in Table 2.2.*

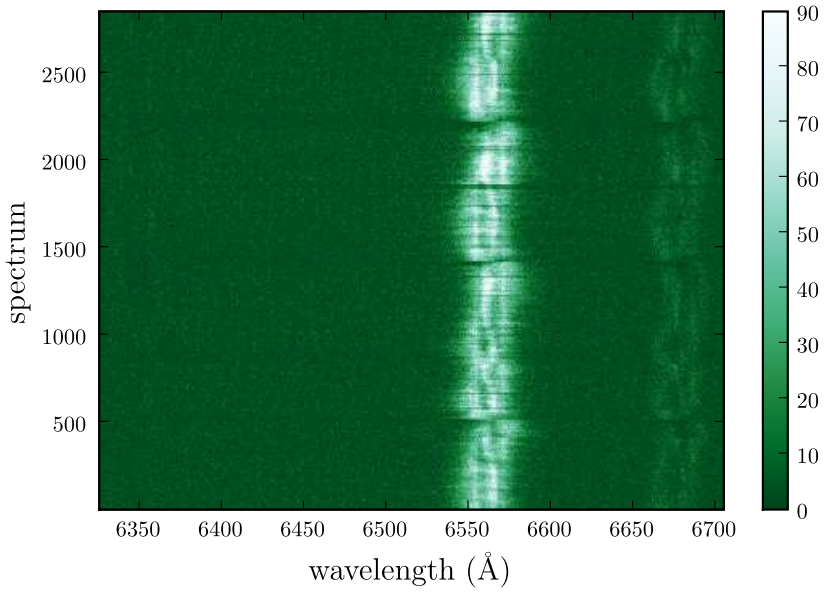

Figure 2.14: *Trail of all normalised red arm spectra of DQ Her taken during three nights. The Hα line at 6563Å and HeI line at 6678Å can clearly be seen.*

To study the spectra and trails further we will phase bin the spectra, such that we e.g. sum or average different spectra that are taken when the binary was in the same orbital position if we want to see variations over the orbit. Phase binning is a useful technique to gain in terms of S/N when one wants to study an effect that is only weakly visible or not visible at all on single spectra. Since we want to study the variations over the orbital period and over the spin period of the white dwarf (assuming that this spin causes the famous 71s pulsations), we want to adopt orbital and spin ephemerides. As mentioned in Section 2.1.5, the most recent ephemerides were published in Wood et al. (2005). They were calculated using photometric observations made both before and after our spectra were taken and should thus be quite reliable to interpolate the ephemerides to the summer of 1998. To compare our observation timings with the ephemerides expressed in HJED, 63.2 seconds were subtracted from the zero points of the ephemerides. This number is the sum of the constant difference in the definition between HJED and UTC (32.2 seconds) and the number of leap seconds introduced up to the summer of 1998 (31). Using these predicted eclipse times and maximum spin flux times, we assigned an orbital phase and spin phase to every spectrum. The orbital phase is defined as explained before with phase 0 at eclipse. The spin phase is defined in a similar way but with 0 at maximum spin pulsation amplitude in the continuum.

To have a detailed look at the orbital variations in the lines, the spectra were phase-binned on the orbital phase in 250 chunks of 0.004 cycles each. The behaviour of Hγ is depicted in Fig. 2.15. Two identical orbital cycles are shown. White lines are plotted for empty phase bins, i.e. phase chunks in which no spectra are taken. Though DQ Her was 'continuously' observed for hours every night, uncovered phases still appear because of technical downtime during the observations. It is a pity that exactly the eclipse phase is poorly covered, because this limits our capability to compare spectra in and out of eclipse. The broadest components of the line, stretching out to around 1000 km/s, are produced by the receding and approaching inner parts of the orbiting disc at positive and negative velocities respectively. The S-shape of the broad components is due to the velocity of the disc as a whole in the orbit around the centre of mass of the binary. The velocity amplitude of this S-wave is K_1 as defined in Section 1.2.1. The component in the middle of the trail, with lower velocities than the disc, has velocity components that are opposite to the motion of the disc, suggesting that this emission comes from the secondary star. This will be proven by studying Doppler maps in Section 2.3. The clear appearance of the secondary's emission gives a flavour of the results we can expect from this dataset as compared to Martell et al. (1995), because on their corresponding trail, the secondary is only slightly visible at phase 0.5.

The orbital trail of HeI λ4472, Fig. 2.16, is similar but does not show clear emission of the secondary star. The trail of HeII λ4686 in Fig. 2.17 looks different though. The line does not have a double peaked structure as one would expect from the emission of an accretion disc, but the overall motion is equivalent to the one seen in the other trails. This suggests that the light comes from the disc regardless the absence of the expected peaks, but at least

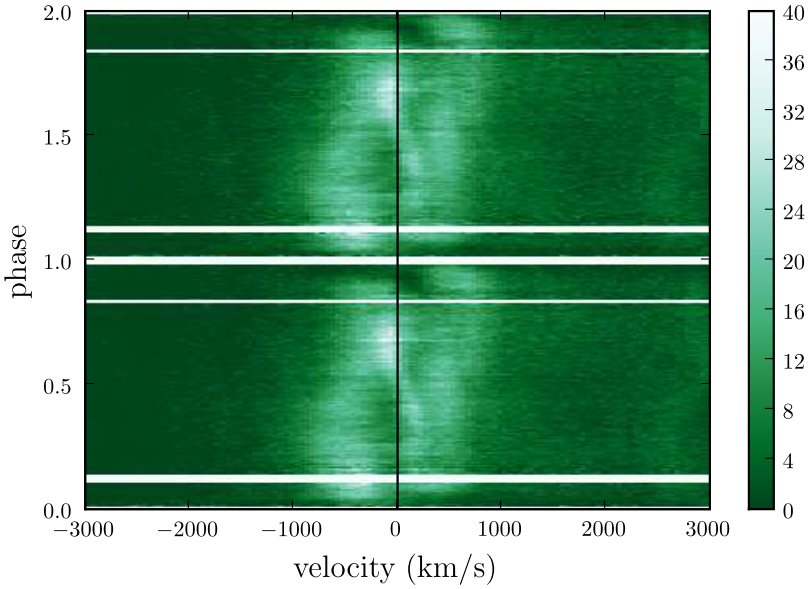

Figure 2.15: *Trail of Hγ λ4340, folded over the orbital phase. Two phases are plotted for clarity. The eclipse is situated around phases 0, 1 and 2. White lines are shown when the orbital phase was not covered due to technical downtime of the telescope during the observations. The broad component shows the double peaked emission line from the accretion disc around the white dwarf. The component that is anti-phased to the white dwarf is emission from the secondary star.*

partly from regions that do not follow Keplerian orbits. A contribution of material whose Keplerian orbits are disturbed by interactions with the magnetic field, e.g. the threading region or an accretion curtain, would be able to produce velocity components that are not expected on a Keplerian basis. When we recall the basic image of the system, with a donor star orbiting in the same direction as the disc around the white dwarf, we understand that the blueshifted part of the disc will be hidden behind the red dwarf before the red part is eclipsed. This effect is known as *rotational disturbance*. Zooming in on the eclipse (see Fig. 2.18), we find out that this effect can actually be observed: the blueshifted light gets eclipsed first and is also the first to reappear at eclipse egress.

The Hβ emission on Fig. 2.19 shows a pattern that is equivalent to the one observed for Hγ. We again see the high velocity components produced by the disc and the secondary in anti-phase with the overal disc motion. Zooming in on the eclipse (Fig. 2.20), the rotational disturbance is again evident and appears to set in at earlier phases than in the case of HeII. This means that HeII mostly sits in the inner part of the WD-accretion disc system, which fits the hypothesis given above that a large part of the HeII emission arises from the threading region or accretion curtains.

The appearance of Hα on Figs. 2.21 and 2.22 is more puzzling. The broad disc components and the secondary's emission are present once again, but there are also features around

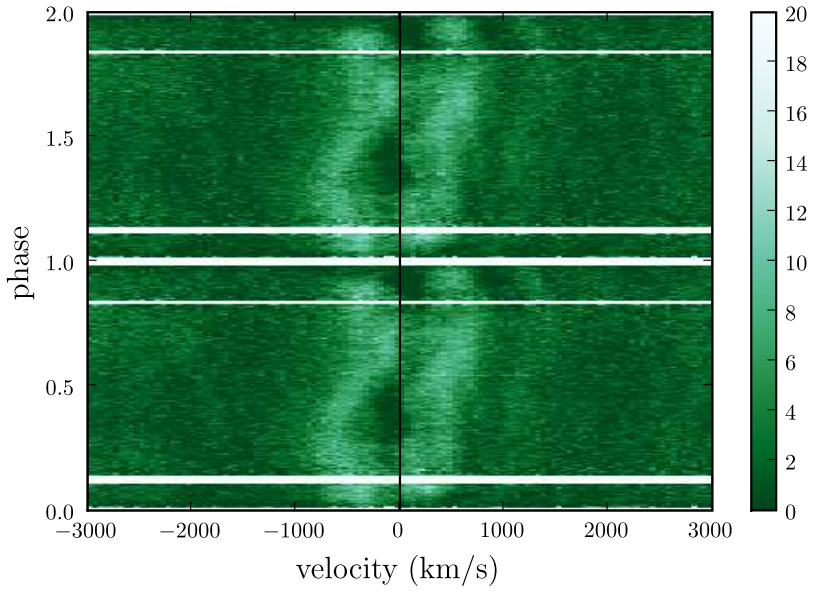

Figure 2.16: *Orbital trail of HeI λ4472. The line is less strong than Hγ but shows the same emission components (see Fig. 2.15). The maximum amplitude of the color scale is half that of the other orbital trails.*

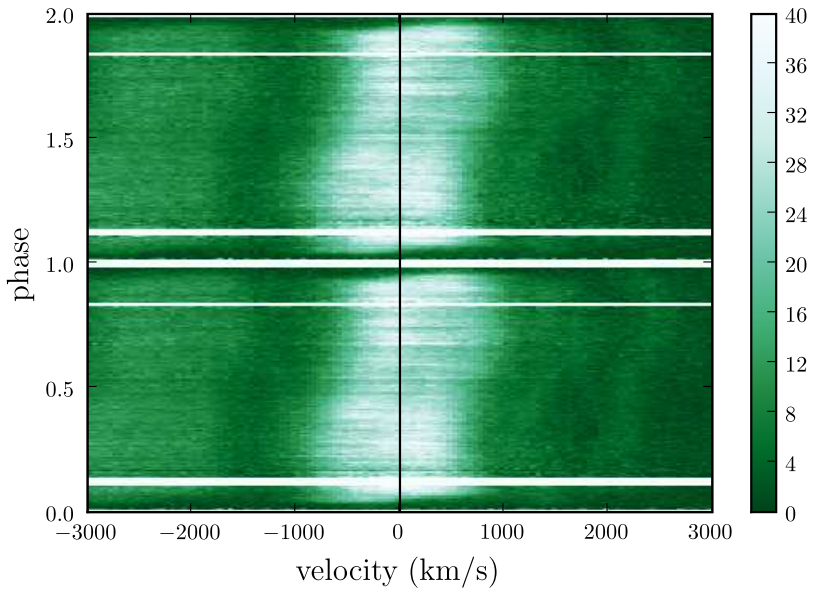

Figure 2.17: *Orbital trail of HeII λ4686. A broad emission component can be seen that is likely to come from the accretion disc, but contrary to what is observed in the Balmer lines and HeI lines, the line is not double peaked. This suggests that the line emitting region has a strong non-Keplerian component, like e.g. an accretion curtain. The weaker line around -1500 km/s is the Bowen blend.*

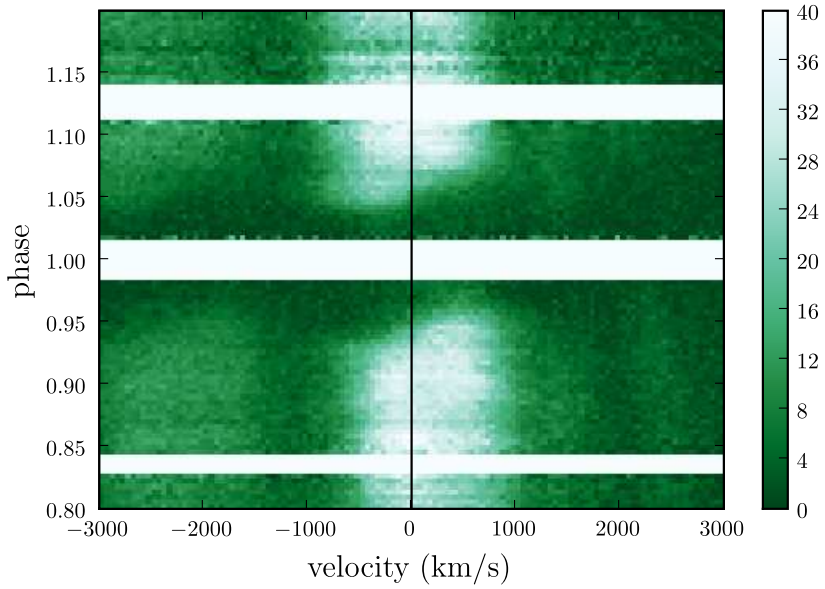

Figure 2.18: *Zoom on the eclipse phases of the HeII trail shown in Fig. 2.17. The blueshifted light gets eclipsed first and reappears earlier than the redshifted light. This effect is called rotational disturbance and is a consequence of the accretion disc that gets eclipsed by a progradely orbiting secondary star, which will first eclipse the blueshifted part of the disc and then the redshifted part.*

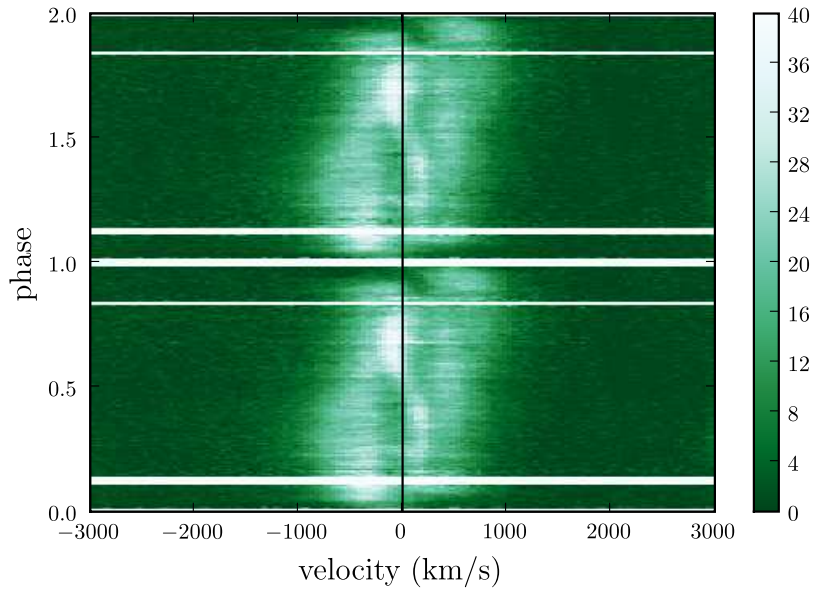

Figure 2.19: *Orbital trail of Hβ λ4861. The emission pattern is completely equivalent to the one of Hγ shown in Fig. 2.15.*

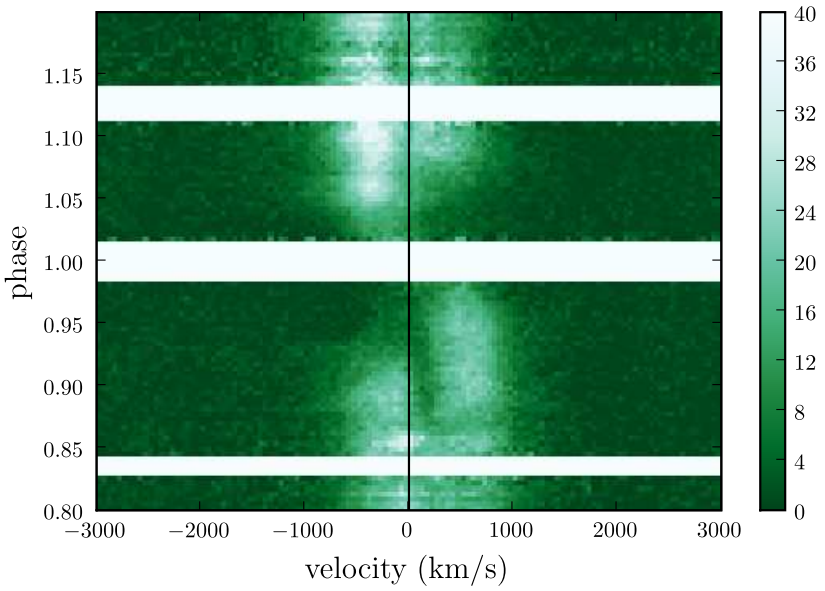

Figure 2.20: *Zoom on the eclipse phases of the Hβ trail shown in Fig. 2.19. The rotational disturbance is clearly seen. The eclipse set in earlier than for the HeII line shown in Fig. 2.18, which suggests that Hβ is formed further out in the disc than HeII λ4686.*

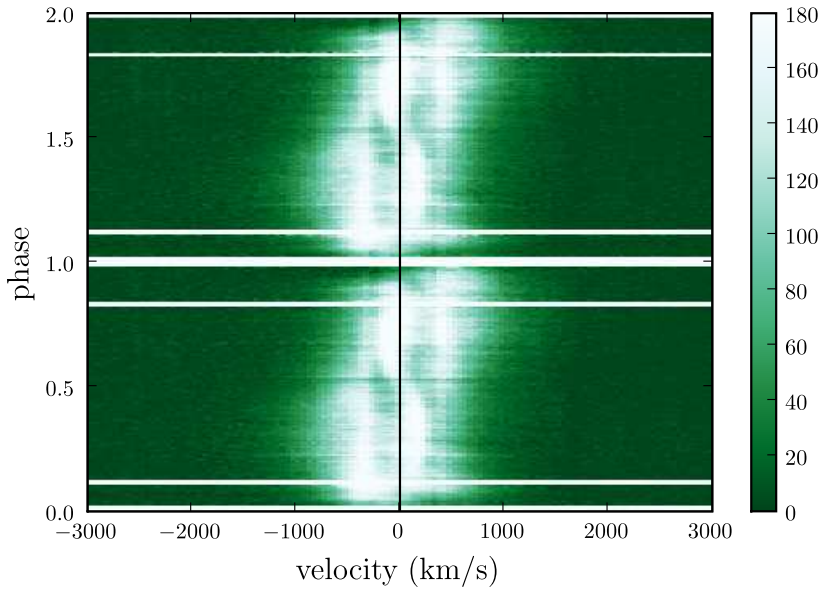

Figure 2.21: *Orbital trail of Hα λ6563. Besides the usual CV components like the disc and the secondary there are stationary components visible around -400 and +400 km/s. These are discussed in Section 2.5.*

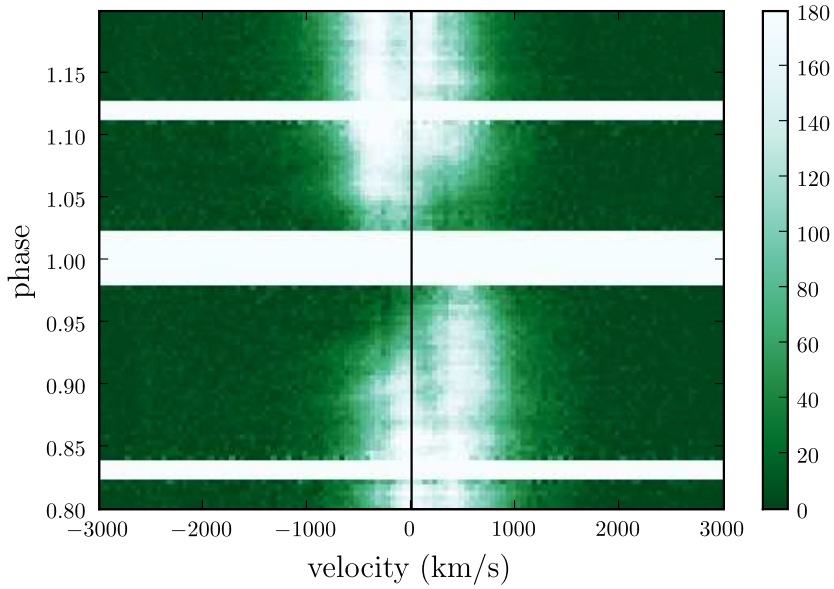

Figure 2.22: *Zoom on the eclipse phases of the Hα trail shown in Fig. 2.21. The rotational disturbance pattern is comparable to that observed in Hβ (see Fig. 2.20).*

-400 km/s and +400 km/s that do not move at all. They can thus not be associated with the disc, nor with the donor star. This phenomenon is discussed by Bianchini et al. (2004), who find a stationary component around zero velocity as well. We will come back to this in Section 2.5. Bianchini et al. (2004) report the same triple peaked line feature in HeI λ6678. On Fig. 2.23 we indeed see a weak component around +400 km/s, but the zero velocity and negative velocity components are less clear. The disc and secondary again show up as expected.

2.3 Doppler tomography of DQ Her

2.3.1 Introduction to Doppler tomography

Apart from the crude interpretation of the spectrum trails, one can also use Doppler tomography to gain insight in the sources that contribute to a spectral line. Doppler tomography was put forward as a means to make images of binary systems with accretion discs by Marsh & Horne (1988). If all material in a disc would follow Keplerian orbits, we would be able to define a one-to-one relation between velocity and position of matter. Unfortunately, contributions from matter in non-circular orbits, from the accretion stream or the secondary star shut the door to defining such a relation. Doppler tomography therefore aims to make an image of the emitting regions in velocity space rather than spatial coordinates.

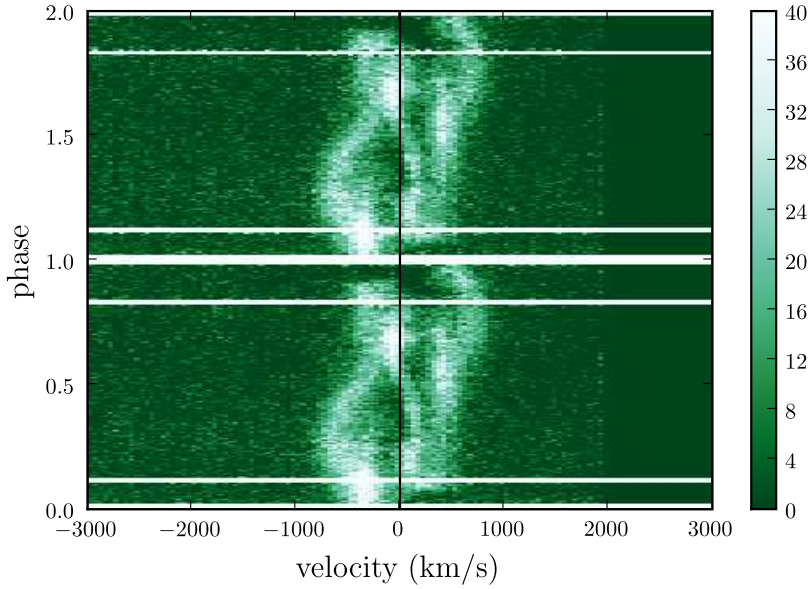

Figure 2.23: *Orbital trail of HeI λ6678. The secondary is visible as in the other lines but the disc gives rise to a very peculiar line profile that is more complicated than simple double-peaks.*

To get an idea of the image we can expect from a system like DQ Her, let's consider Fig. 2.24. On the image in position coordinates, the white dwarf with its accretion disc is located at the left with the origin of the coordinates at the position of the WD, and the donor star on the right. The whole system is moving counterclockwise around its centre of mass. The y-axis thus points in the direction of motion of the secondary in this position. The donor star consequently has no velocity in the x-direction and a positive velocity in the y-direction. In velocity coordinates (left figure) the star is indicated with a cross on the V_y axis. Material in the disc follows a quasi-Keplerian orbit, with a velocity $V \propto R^{-1/2}$. Material on the outer edge of the disc (in position coordinates, e.g. point B) will thus have the lowest velocity and will appear closest to the origin, on the inner edge of the disc, in velocity coordinates. Matter that is orbiting closer to the central object will have a higher speed and will appear further away from the origin in the velocity image. The disc therefore appears inside out in velocity coordinates. Note also the flow of the accretion stream from the first Lagrange point to the disc and its appearance in velocity coordinates.

The fact that the system orbits gives us the chance to observe the projected Doppler image from all sides, i.e. at all orbital phases. This is illustrated in Fig. 2.25. At phase 0.25, one would observe the spectrum shown on the right of the image. At this phase, the spot is receding from the observer and thus visible at a redshifted wavelength. The spectrum on the bottom of the figure is seen at phase 0.5. At this point, the spot is slightly blueshifted. The two peaks on the sides show the familiar double-peaked line profile of an accretion disc viewed at a high enough inclination. Both spectra are effectively projections of the image in velocity coordinates, along the indicated directions. Theoretically, spectra at two different

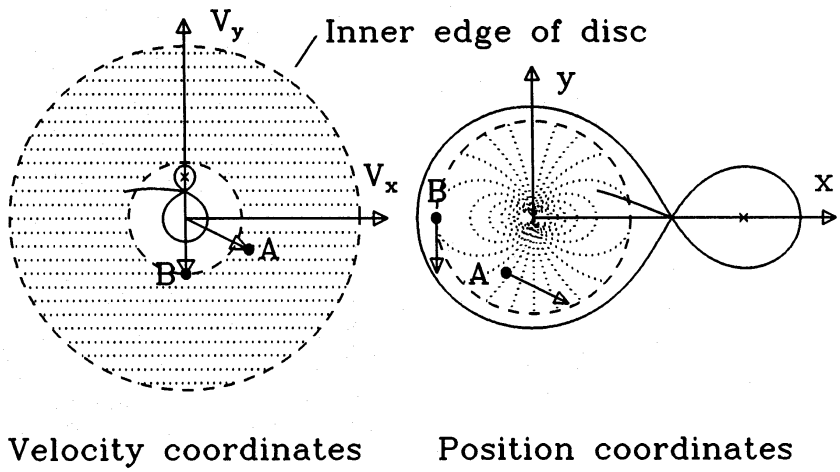

Figure 2.24: *Cataclysmic variable in velocity coordinates on the left and in position coordinates on the right. Doppler tomography allows to create an image in velocity coordinates from spectra taken over the orbital period of the CV. See text for more details. Figure taken from Marsh & Horne (1988).*

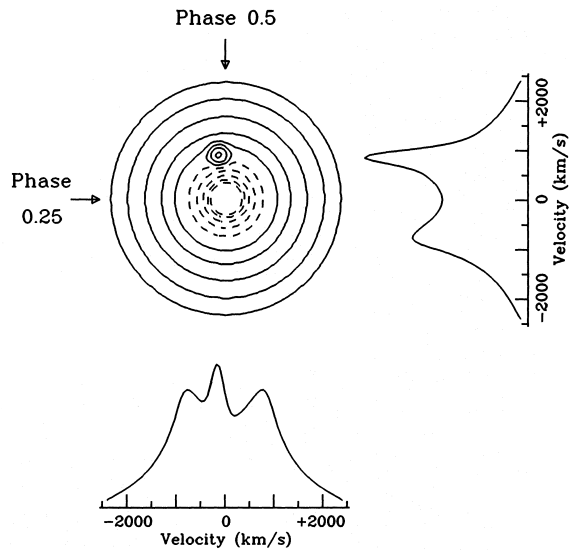

Figure 2.25: *The two spectra effectively show projections of the image in velocity coordinates at two different orbital phases. This way, orbital motion allows to probe the projected Doppler image from all directions, which enables to reconstruct the velocity image using Doppler tomography from spectra that cover the orbital period. Figure taken from Marsh & Horne (1988).*

phases (and not exactly separated by half the orbital period) are sufficient to uniquely locate the spot on the disc. The phase coverage of the spectra together with the radial velocity indications on the spectra due to the Doppler shifts therefore contains all information that is necessary to reproduce a two-dimensional map in velocity coordinates.

In reality, one faces of course a more difficult job because the data are not at all perfect. The approach to restore the image from an incomplete and noisy data set that is presented in Marsh & Horne (1988) is the *maximum entropy method*. As we just explained, it is possible to calculate the orbital trail that would be observed for a certain image in velocity space by calculating the appropriate projections. By a χ^2 statistics the goodness of fit of the predicted trail to the observed trail can be measured. One then tries to reduce the χ^2 by setting up an iterative procedure that slightly changes the image. The clue is however not to try to minimise χ^2 but to stop at a certain value, since from a certain point on one tries to fit the noise rather than the real light contribution of the system. Many solutions with a certain χ^2 exist, from which one tries to choose the one with the highest entropy, i.e. the least structured map that fits the data as well as required. In the paper, the effects of a number of possible noise and error sources are checked, e.g. what would happen if we use a wrong ephemeris zero point (the image would just be rotated) or what the effect of a wrongly set systemic velocity γ would be (the image would be blurred).

2.3.2 DQ Her in the velocity plane: spiral arms in the accretion disc

The maximum entropy method for Doppler tomography is implemented in Tom Marsh's software package DOPPLER[8]. It has been used to compute Doppler maps for all the line trails shown in Section 2.2.3. Choosing the χ^2 value the scripts have to aim for while iterating the map, is to some extent a matter of taste. From a certain point, further χ^2 minimisation starts to introduce sharp features in the image, and especially in the accretion disc, because the procedure then starts to fit noise. The minimal χ^2 value that is reachable highly depends on the S/N of the dataset. The easiest way is to force the routine to go a bit too far, and then relax the χ^2 constraint so that it gets the chance to work on the entropy maximisation, which starts off as soon as the χ^2 goal is reached. Only spectra taken out of eclipse are used.

The resulting Doppler images for the Balmer lines are shown in Fig. 2.26, for the HeI lines in Fig. 2.27 and for HeII λ4686 in Fig. 2.28. A systemic velocity of $\gamma = -60 \pm 8$ km/s (Hutchings et al. 1979) has been adopted. Using the optgam routine from the DOPPLER package, the sharpest Doppler maps were achieved for systemic velocities between -30 and -70 km/s. This confirms that the adopted γ is sufficiently accurate. As mentioned above, a wrongly set γ would blur the images (Marsh & Horne 1988). The size of the Roche lobe of the secondary star as well as the estimated gas stream path from L_1 to the disc are shown in black.

[8]DOPPLER can be obtained from http://deneb.astro.warwick.ac.uk/phsaap/software/.

On the Balmer maps, we find the emission from the secondary star as a dot around $(V_X, V_Y) \approx (0, 200)$ km/s, consistent with the $K_2 = 227 \pm 10$ km/s found by Horne et al. (1993). The accretion disc is also apparent, centered around the white dwarf which has a velocity of $K_1 = -140 \pm 10$ km/s according to the latter paper. The white dwarf itself is not observed because it is not a source of Balmer lines and it is additionally hidden by the disc due to the high inclination. The Hα map is somewhat perturbed by stationary components in the line wings which do not come from material in orbit with the binary. The nature of these components will be discussed in Section 2.5.

The two HeI maps reveal two spiral arms in the disc, which are also present on the Hγ tomogram. The pattern was not observed before in DQ Her, and to our knowledge not in other intermediate polars either, but is almost identical to the one found in a number of dwarf novae during outburst and in novalike CVs. It was first discovered in dwarf novae IP Peg in outburst (Steeghs et al. 1997). In the latter paper, it is shown that spirals in velocity space map onto spirals in positional coordinates as well. A review of the observations of spirals in CV discs can be found in Steeghs (2001). Spirals in accretion discs of CVs are believed to arise from tidal forces from the secondary on the outer regions of the disc, which creates two regions with overdensity and two with underdensity, comparable to the influence of the Moon on the Earth's oceans. Because the material in the disc gradually spirals inwards to orbits with a higher Keplerian velocity, the density structures result in a double spiral arm. Systems in which spirals are seen have a high mass transfer rate and thus a large accretion disc which fills most of the Roche lobe of the white dwarf, which is necessary for the secondary to have a large enough tidal effect. The disc of DQ Her extends up to at least 87% of the white dwarf's Roch lobe (Harrop-Allin & Warner 1996, determined from the eclipse duration). In dwarf novae, the spirals are only observed during outburst when the mass transfer rate is temporarily higher, i.e. for only a few days in an outburst cycle of the order of months. This makes them particularly difficult to observe because the outburst moments are difficult to predict. Since the mass transfer in DQ Her is believed to be in a fairly equilibrium state, the spiral structure is very likely to be permanently visible. This makes the system a good candidate for further research on the spirals in accretion discs.

As mentioned earlier in Section 1.1.1, angular momentum transport in accretion discs is very poorly understood. The famous α-description by Shakura & Syunyaev (1973) explains the momentum transport by a (further not understood) viscosity effect. Spiral arms are of notable astrophysical interest because spiral shocks are believed to be an alternative (or complementary) means to transfer angular momentum. A review of theoretical efforts on spiral shocks is presented in Boffin (2001). The establishment of spiral waves in an accretion disc of an IP also re-enforces the findings by Murray et al. (1999) that tidally induced spirals can propagate sufficiently far into the disc of an IP such that they can modulate the accretion rate onto the white dwarf. This could explain the sidebands of the spin frequency that are often found in X-ray and optical light curves of IPs. These sidebands are thought to be a sign of mass accretion via a direct mass stream from the first

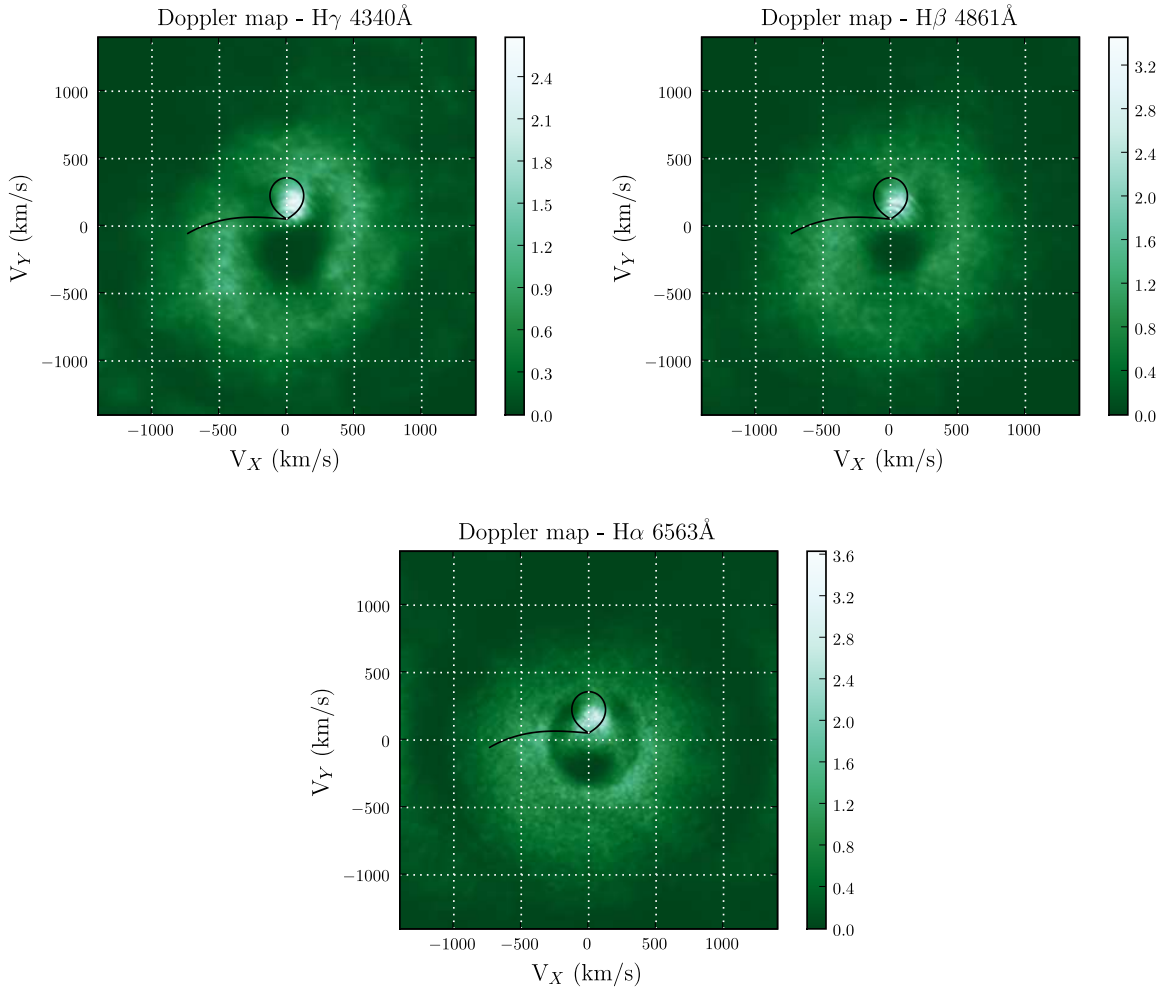

Figure 2.26: *Doppler maps of the Balmer lines. The maps show the secondary star around* $(V_X, V_Y) \approx (0, 200)$ *km/s and the accretion disc. The Roche lobe of the secondary and the estimated gas stream path are shown in black. The white dwarf is not visible because it is occulted by the front part of the disc. On the Hγ map (top-left), the disc shows two spiral components, which are even more clear on the HeI maps on Fig. 2.27. The Hα map is somewhat perturbed by the stationary components we saw earlier in Fig. 2.21 because the tomography algorithm assumes that all emission comes from material that orbits at the orbital frequency around the centre of mass of the binary.*

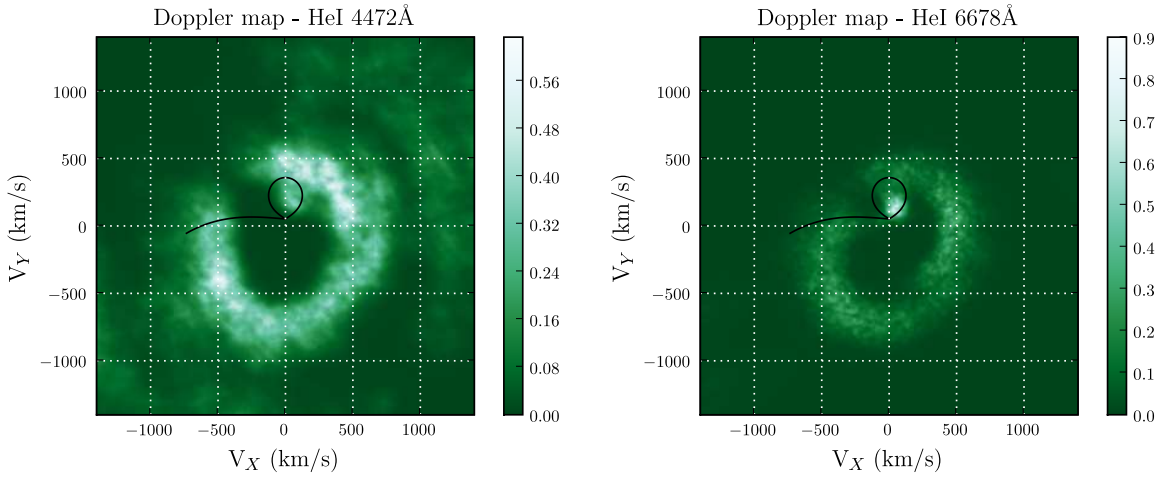

Figure 2.27: *Doppler maps of the HeI lines. The maps show clear spiral components in the accretion disc. These spiral waves are induced by tidal effects of the secondary star on the outer regions of the disc. It is the first time that spiral waves have been observed in an accretion disc of an intermediate polar.*

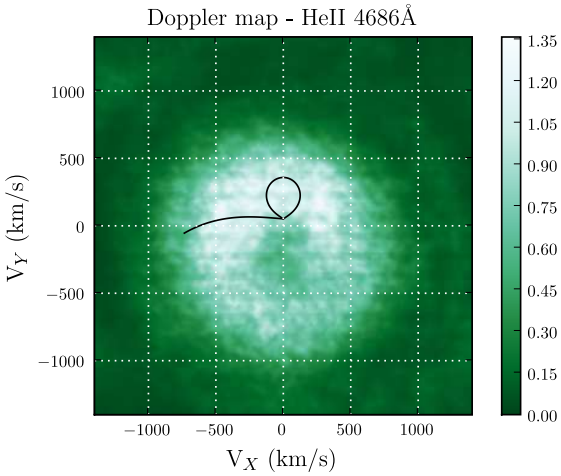

Figure 2.28: *Doppler map of HeII λ4686. The filled ring corresponds to the absence of a double peaked line profile in the trail (see Fig. 2.17). The line is very likely produced in the inner part of the disc in a region that is influenced by the magnetic field of the white dwarf, e.g. in an accretion curtain, and therefore a substantial non-Keplerian emission component is present which explains the emission at very low velocities which would otherwise not be expected.*

Lagrange point to the white dwarf rather than via an accretion disc and have been used to discriminate between systems that have only disc accretion, only stream accretion or a mixture of both (see e.g. Norton et al. 1996 for a model of the X-ray powerspectrum and Hellier 2007 for a review on accretion in IPs). If spirals can cause the sidebands as well, the conclusions drawn on this basis will have to be revisited. Furthermore, spirals in accretion discs seem to be small scale versions of spirals observed in galaxies like our Milky Way and research in one of the fields might contribute to a better understanding in the other.

The map of HeII λ4686 shows a filled ring. As Martell et al. (1995) already pointed out, this reflects the absence of a double peaked line profile which was already visible on the trail for that line, see Fig. 2.17. The HeII λ4686 line is formed after electron capture by HeIII. The ionisation energy of HeI is 24.6 eV and further ionisation of HeII requires 54.4 eV. High temperatures are needed to make this possible, which are only found in the inner regions of the disc. In this region, the material has high Keplerian velocities. The presence of a lot of emission at lower velocities shows that the line has a much higher non-Keplerian component than the other lines. We therefore consider it very likely that a substantial part of the line is produced in a region that is highly influenced by the magnetic field, like the accretion curtains, because material that gets trapped by magnetic field lines gets a larger than usual velocity component towards the white dwarf as well as a non-negligible component in the direction perpendicular to the disc. We will come back to this in Section 2.4. We can also confirm the notice by Martell et al. (1995) of high emission regions on the upper half of the map. The higher emission in the disc part $V_X < 0, V_Y > 0$ can be associated with the accretion stream (see also Fig. 2.24), but the high emission at $V_X > 0$ is not easily explained.

In an attempt to find the variations in the light curve due to the reprocessed X-rays of the white dwarf in the disc or on the secondary star, Doppler maps were also created for different phases in the spin period and the beat period, but no significant variations were found that could be associated with the light house beam.

2.4 DQ Her's 71s oscillations

As described in Section 2.1.6, we want to study the oscillations in DQ Her's light curve with a period of 71s or 142s (see Section 2.1.4 for a discussion on this uncertainty). This pulsation is due to X-rays from the white dwarf that are reprocessed by (some parts of) the accretion disc (e.g. Patterson et al. 1978; Chanan et al. 1978; Wood et al. 2005). The 71s/142s period then refers to the spin period of the white dwarf. A less favoured explanation is that the 71s pulsation is in fact the beat period ($\omega_{beat} = \omega_{spin} - \omega_{orb}$), which would be the case if the vast majority of reprocessing is done in the bright spot where the accretion stream hits the disc (e.g. Saito & Baptista 2009) or on the surface of the secondary star, since both orbit at the orbital frequency.

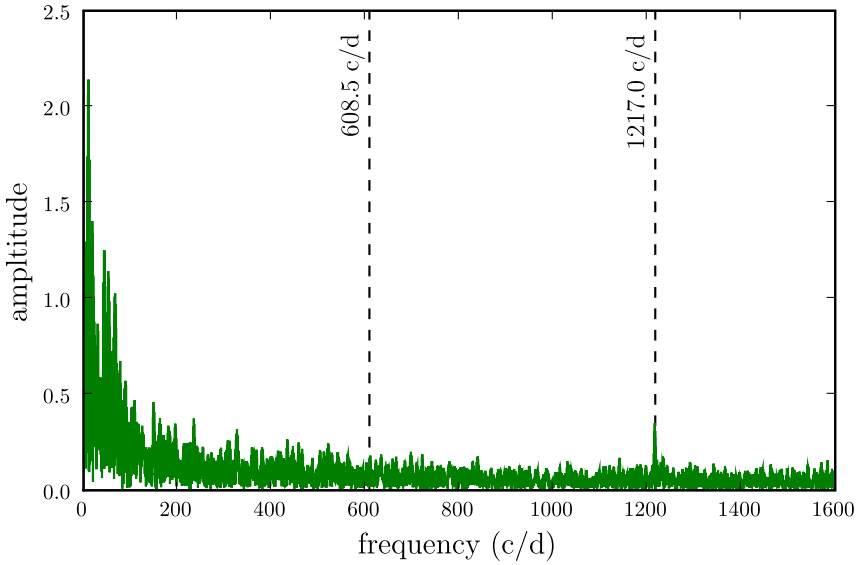

Figure 2.29: *Periodogram of the flux in the HeII λ4686 line. The peak at 1217 c/d corresponds to the 71s periodicity that is believed to be the spin period of the white dwarf. No significant amplitude is found at 142s (608.5 c/d). The peaks at low frequencies are noise due to the relatively short baseline (a bit more than 2 days) and the frequency and spacing of the observations.*

Since our spectra were taken without a comparison star in the slit, we could not correct for variations in the observed intensity that are due to atmospheric conditions and slit losses. We thus work with normalised spectra and limit our study of the oscillations to the flux in the emission lines. These can fluctuate more than the continuum level if the high energetic UV and X-ray photons of the WD beams trigger extra line transitions. The standard method to find a periodicity is to calculate a Fourier transform of the light curve. Such an amplitude spectrum is shown in Fig. 2.29 for the flux in the HeII λ4686 line and in Fig. 2.30 for Hβ λ4861. In HeII λ4686, a peak is found around 1217 cycles per day (c/d), which is equivalent to a period of 71s. No pulsation amplitude is found at the 142s period (608.5 c/d). This result is in line with the outcome of most photometric studies which find the white dwarf spin period of 71s, as described in Section 2.1.4. In Hβ, no pulsation frequencies are found above noise level. The line transition in which these photons are emitted is thus not strongly influenced by the beam photons or the emitting region is not easily reached by the beam.

Another method, which is more suitable for spectroscopy, is folding the data on the period under consideration and subtracting a mean spectrum. This way, only the deviations from the mean value are shown, and these are exactly the pulsations we want to study. We followed the same approach as Martell et al. (1995). Our spin trails should thus be comparable to their trails, shown earlier in Fig. 2.4. Only spectra taken at orbital phases from 0.1 up to 0.9 are used, i.e. spectra taken during eclipse are omitted.

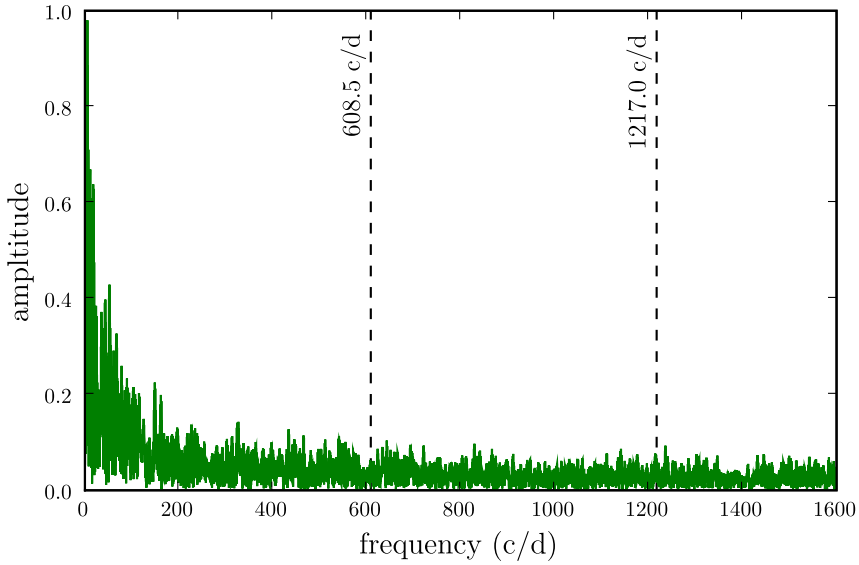

Figure 2.30: *Periodogram of the flux in the Hβ line. Neither of the 71s or 142s periodicities are detected above noise level.*

2.4.1 Spin trails

In Fig. 2.31 a trail of HeII λ4686 is plotted after folding on a 71s period, repeated 4 times for clarity. The white sine curve shows the path of the pulsation that should be seen when the reprocessing region is a small part of the disc that follows a circular orbit. Figure 2.32 shows how a beam that sweeps over an accretion disc gives rises to such an S-wave on a trail of spectra that are folded on the spin period of the white dwarf. On Fig. 2.33 the 71s trail is repeated, now showing 2 cycles, side by side with a trail of one cycle for a 142s period to allow comparison between the two possible spin periods. For a 71s spin period, one reprocessing region is needed. For a 142s spin period, one needs two regions to produce the observed periodicity.

We can confirm, with greater significance, the observation of Martell et al. (1995) that the pulsation is visible in HeII λ4686 when the beam illuminates the redshifted part of the back side of the disc, but invisible when the beam points to the front side or the blueshifted part of the back side. The absence of fluctuations in the light coming from the front side of the disc is not surprising: the inclination is close to 90° and since a disc is not flat but rather concave, our view of the front part might well be blocked by the thick edge (the rim) of the disc. The fact that no fluctuations are seen in the blueshifted part of the back side of the disc is more puzzling. Martell et al. (1995) propose that the pulsation comes from the threading region, i.e. the region at the inner edge of the disc where the material gets trapped by the magnetic field of the white dwarf. If this region is optically thick, a velocity gradient in the direction of our line of sight will result in an enhanced emission (Horne 1995).

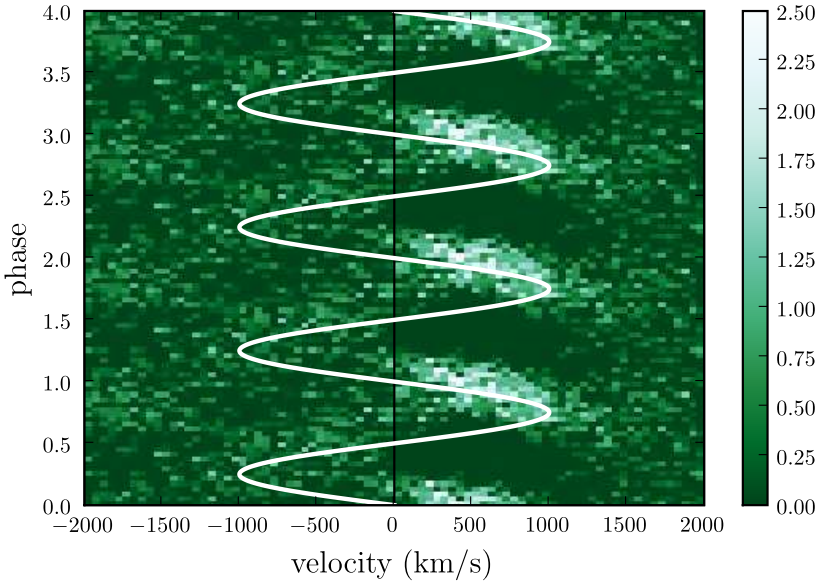

Figure 2.31: *Spin trail of HeII λ4686 folded on the 71s period with the average spectrum subtracted, repeated 4 times for clarity. The sine wave shows a basic model for the pulsations if they arise from a part of the disc that is in a circular orbit around the white dwarf. Variations in the line are seen in the redshifted part but not in the blueshifted, and only when the beam points to the back side of the disc. See text for a more detailed discussion.*

Another possible explanation is that the X-rays are reprocessed by (optically thick) accretion curtains. An artist impression of an accretion curtain in an intermediate polar was presented earlier in Fig. 1.4. Imagine that the top X-ray beam from the white dwarf only illuminates the bottom side of the top curtain, which is not implausible because of the curtain's curvature, and assume that the curtain is optically thick (contrary to the artist's impression), then it might be the case that we see the bottom side of the curtain when it is receding from us and the non-illuminated top side when it is approaching us. Such a scenario would produce variations in the redshifted part of the line, but no fluctuations in the blueshifted part. This proposition is quite ad hoc and should be checked thoroughly by modelling but this was too complex to be done in the time span of this work.

The spin trail of He II λ4686 also potentially offers a means to conclude the discussion on whether the spin period is 71s or rather 142s with two spots contributing to the pulsation. The slope of our very simplistic model clearly fits the 142s trail (Fig. 2.33, right) better than the 71s trail (left). We believe that our model would be fairly correct if a small part of the disc at semi-Keplerian orbits, e.g. the inner part of the disc, reprocesses the X-rays of the WD poles. If that is the case, a 142s spin period is to be preferred. If however reprocessing in accretion curtains is in play, a simple S-wave is too simple and a more detailed model would be required to draw a conclusion. As discussed in Section 2.3.2, the Doppler map of the line (Fig. 2.28) shows a large non-circular component, which suggests that such a

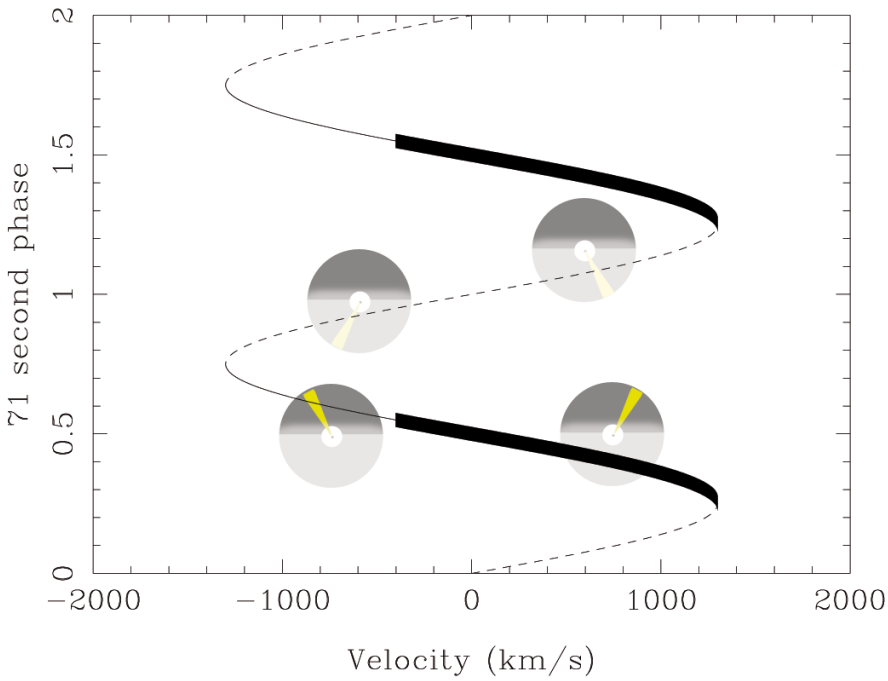

Figure 2.32: *A simple model of a single beam from the white dwarf that sweeps over the accretion disc at the WD's spin frequency gives rise to an S-wave on the trail of the spectra, folded on the spin period. The surface of the front part of DQ Her's disc is likely to be hidden by the rim of the disc, which makes the reprocessed light invisible at phases 0.75 to 1.25 (dashed line). Reprocessed light of the beam is expected to be visible when the beam points to the back side of the disc, between phase 0.25 and 0.75 (bold and thinner full line). On the spin trails of DQ Her, the reprocessed light is however only visible from the redshifted part of the disc. This observation cannot be explained by the simple model we present here.*

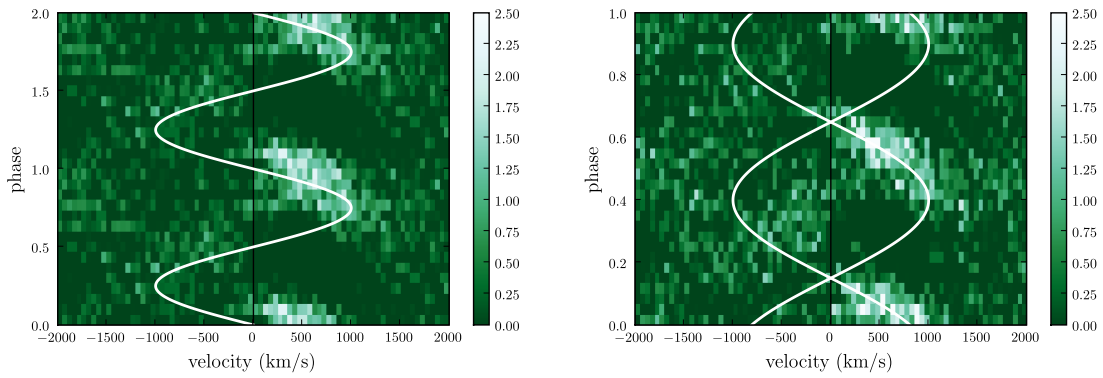

Figure 2.33: *Trail of mean subtracted spectra for HeII λ4686 folded on a 71s period (left, two cycles shown) and on a 142s period (right, one cycle shown). The simple sine model for the pulsations fits the slope of the pulsation profile better for the 142s period, but it is likely that reprocessing of X-rays in an accretion curtain or in the threading region plays a significant role, in which case a more sophisticated model would be necessary.*

curtain contribution is very likely to be present. The fact that we don't see any significant difference between the first half and second half of a 142s cycle confirms earlier predictions that if the spin period is really 142s, the two poles would have to be almost identical.

Given the much higher S/N of our data compared to the spectra used by Martell et al. (1995), we were able to check the variability in the pulsation of the HeII λ4686 line over different orbital phases. Figure 2.34 displays the spin trails (folded on the 71s period) for orbital phases 0.1-0.5 on the left and 0.5-0.9 on the right. The amplitude of the pulsation in the redshifted wing of the line seems a little lower at the later orbital phases but the variability is still obvious. This indicates that most of the pulsation originates from the (inner regions of) the disc, and not from the bright spot or the secondary star. The latter two would result in a 71s pulsation if the spin pulse is in reality 70.8s. The 71s pulsation in the redshifted wing at orbital phases where the possible beat frequency contributors (the bright spot and the secondary) are in the blueshifted part of the line rules out the possibility that the spin period would be 70.8s, with the dominant 71.0s pulse being the beat period. The time baseline of the observations is long enough to resolve the difference between a 70.8s pulsation period and a 71.0s period. This is clearly seen on movies of the spin trails for even finer orbital phase chunks. On the 71s trails, the pulsation profile in the redshifted part of the line stays at the same phase, while for 70.8s it shifts over 1 spin phase in 1 orbital cycle. This is illustrated on Fig. 2.35 which shows the trails folded on the 70.8s period for the same orbital phase chunks as Fig. 2.34. The shift of the pulsation in the red wing is clearly visible, which also strengthens our believe that if a 70.8s periodicity is present at all, it is certainly not dominant over the 71s period.

Traces of a pulsation are also visible in the trails of the Balmer lines, which are shown for the 71s period on Fig. 2.36 for Hγ and on Fig. 2.37 for Hβ. The amplitude is only

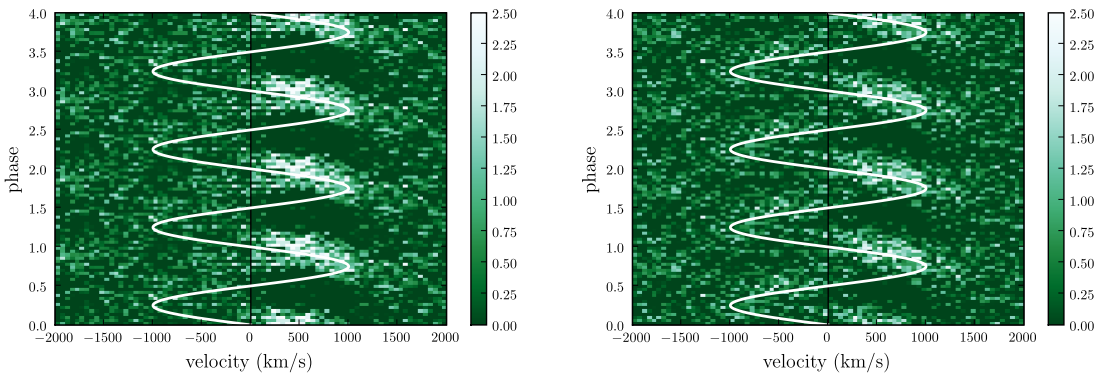

Figure 2.34: *Trails for HeII* λ4686 *from data at selected orbital phases, folded on a 71s period. For the left figure spectra taken at orbital phases 0.1 to 0.5 have been used and for the right figure phases 0.5 to 0.9. In both figures variations are seen in the redshifted part of the line. If reprocessing would mostly occur in the bright spot, no pulsation should be visible in the redshifted part of the line on the right figure because the hot spot is at blueshifted wavelengths at these phases.*

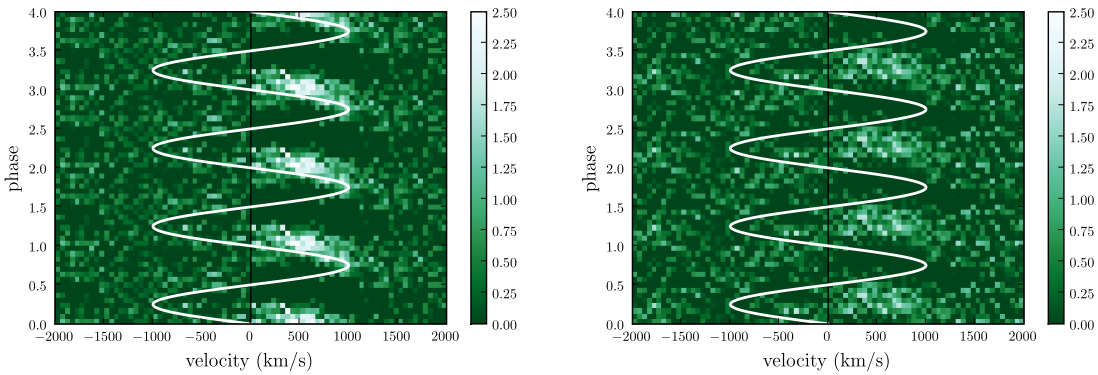

Figure 2.35: *Trails for HeII* λ4686 *from data at selected orbital phases, as in Fig. 2.34, but now folded on a 70.8s period. This would be the true spin period if the 71s period is the beat period. The pulsation in the red part of the line clearly doesn't stay in phase with the sine model which proves that the 70.8s periodicity cannot be dominant.*

marginally above noise level, but it seems that there is a fluctuation visible in the blue parts of the Balmer lines as well. The red wings seem to show a pattern that is different from the one seen in HeII λ4686. The pulsation is not well fitted by the simple 71s pulse model, but the same holds for the 142s model (not shown). This suggests that the more complicated accretion curtain reprocessing scenario is to be favoured.

The pulsations in the He I lines are too weak to be detected on the spintrails, see Fig. 2.38.

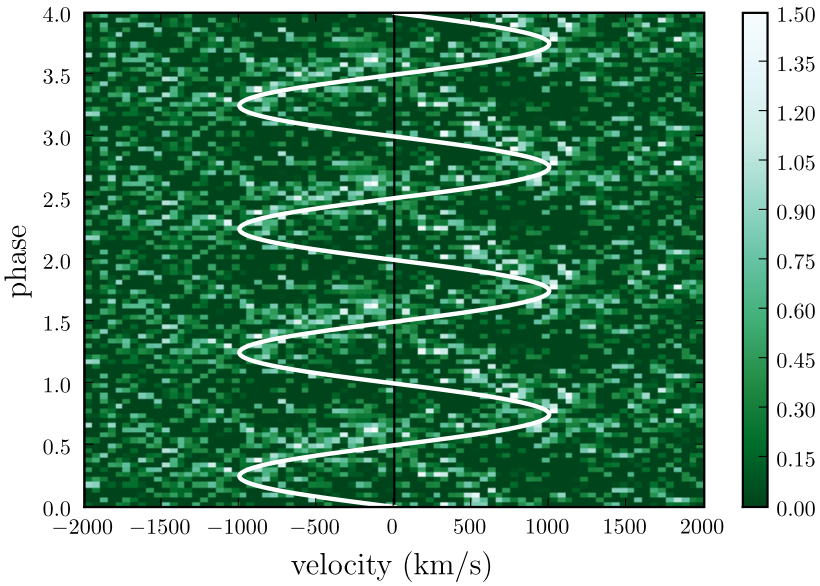

Figure 2.36: *71s spin trail for Hγ. A weak pulsation component seems present in the blue part of the line, which fits well with the 71s model. The variations in the red wing of the line have a different slope and are not well fit by either the 71s model shown here or a 142s model. One should however be careful when drawing conclusions from this trail because the variations are hardly above noise level.*

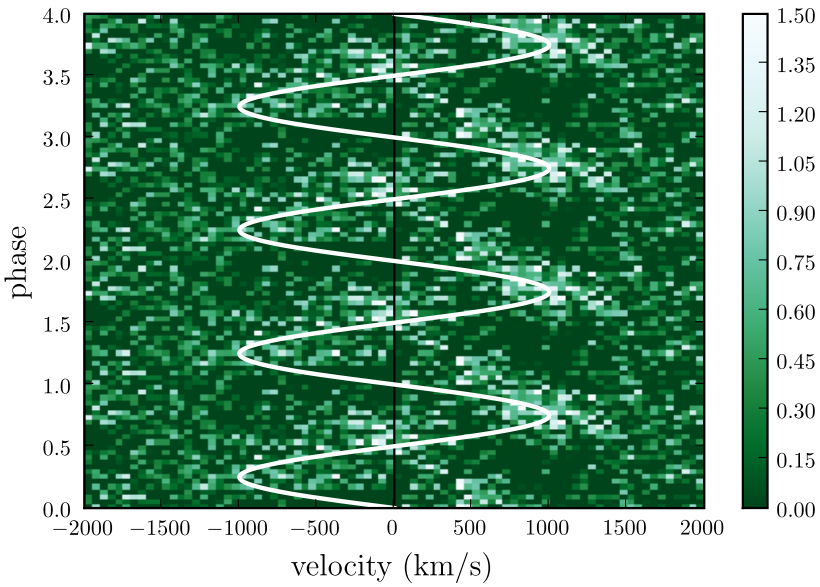

Figure 2.37: *71s spin trail for Hβ, which is almost identical to the Hγ trail shown in Fig. 2.36.*

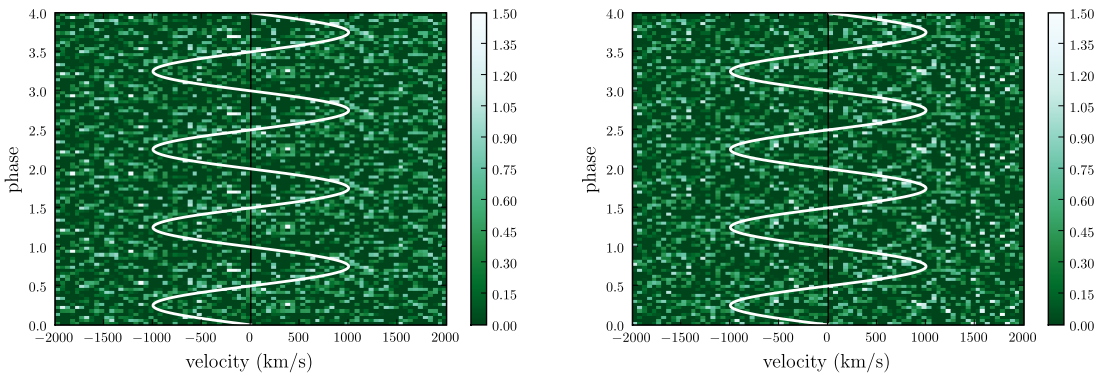

Figure 2.38: *71s spin trail for HeI λ4472 on the left and HeI λ4925 on right. No variations are detected above noise level.*

2.4.2 Optically thick accretion curtains and the bright spot involved?

A few weeks after we started thinking of the possible importance of accretion curtains, their existence was 'shown' by Saito & Baptista (2009). They used the dataset formerly used by Martell et al. (1995) for eclipse mapping. The latter technique has similarities with Doppler tomography but uses exactly those spectra that are dropped when producing Doppler maps: the spectra taken during eclipse. The general idea is that the evolution of the line flux during eclipse ingress and egress traces the structure of the disc by sequentially blocking light from other parts of the disc. The spectra taken during eclipse phases were divided into four spin phase groups, in an attempt to find fluctuations in the disc's emission due to the X-ray beams sweeping through it. Their maps for different spin phases with the mean map subtracted are given in Fig. 2.39. The eclipse maps on top (shown for 4 different spin phases) suggest that there is a rotating component at the inner radius of the disc, which can be associated with an accretion curtain, and pulsating emission from the bright spot in the top right part of the disc. They conclude that mostly the bright spot and to a lesser extent accretion curtains contribute to the 71s fluctuations, and that the observed frequency should be the beat frequency instead of the spin frequency because of the larger contribution by the bright spot. If the latter would be true, the pulsation should not be visible on a 71s period in the redshifted part of the line on orbital phases when the bright spot is in the blueshifted part of the disc. The pulsation is however still there, as explained in the previous section. Given this contradiction and the fact that eclipse mapping is much less constrained than Doppler tomography because it only uses data taken during eclipse, during which part of the disc remains hidden from view, we believe that further evidence is necessary to confirm that the HeII-pulsation arises from the curtains. The bright spot might contribute as well, but probably not as much as derived from the eclipse maps because we can rule out the possibility that 70.8s is the true spin period, which would be necessary if the bright spot is the dominant source of the pulsations (see Section 2.4.1).

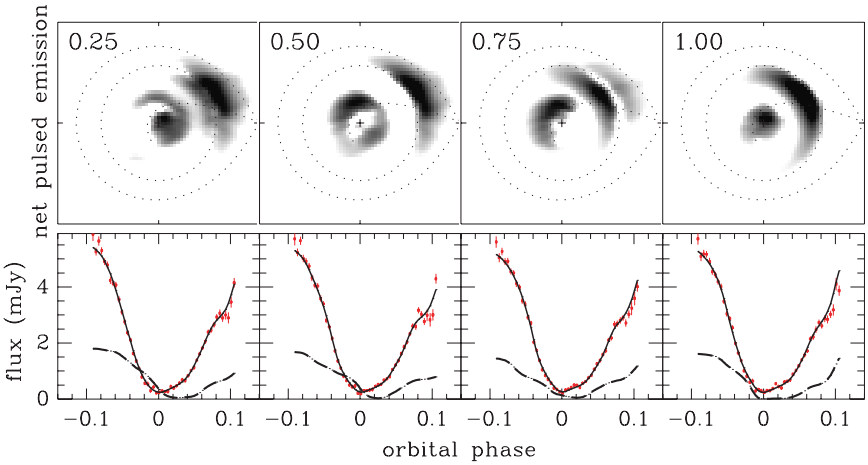

Figure 2.39: *Eclipse mapping of HeII λ4686 by Saito & Baptista (2009). The top row shows eclipse maps with a mean map subtracted for 4 different spin phases. On the bottom row the fluxes in the line are shown. The variations between the different spin phases are hardly visible by eye.*

Figure 2.40: *Red end of a median of a few hundred red arm raw CCD readouts. At the left emission from the nova shell is visible. The position coincides with the wavelength of Hα and explains the stationary components in the orbital trail shown in Fig. 2.21.*

2.5 The triple peaked line profile of Hα

Bianchini et al. (2004) reported stationary components in the wings and the centre of Hα. We found the same emission components in the wings of the line (see trail on Fig. 2.21). The component in the centre of the line is less obvious because it is very close to the emission of the secondary. On the average spectrum, the blueshifted component appears at a radial velocity of -388 ± 2 km/s and the redshifted component at $+337 \pm 2$ km/s.

Contrary to the findings of Bianchini et al. (2004), we do see emission from the nova shell, that results from the nova outburst of 1934, on our spectra. This is illustrated in Fig. 2.40. The position of the nova shell in the dispersion direction coincides with the wavelength of Hα, which suggests that the stationary components result from the nova shell. Figure 2.41 shows the average red spectrum of the first night (in green) together with the average spectrum of the sky on the same CCD frames. Because the sky spectra are taken in the regions around the object spectrum, the contribution of the shell that is visible in the sky spectrum is slightly different compared to the contribution of the shell at the position of the object spectrum. Therefore, the sky subtraction step that is part of the data reduction process cannot accurately remove the shell contribution from the DQ Her spectra. At some wavelengths the shell contribution is not completely removed and at some other wavelengths too much flux is subtracted. Estimating the shell contribution is further hindered by the shell's fairly complex brightness structure. This can be seen on the high resolution spectrum of Vaytet et al. (2007) which is shown in Fig. 2.42.

If we adopt a nova shell expansion speed of ≈ 370 km/s as was found by Vaytet et al. (2007), the approximate radius r of the shell in 1998, 64 years after the nova, would be 7.5×10^{11} km, or about 5000 AU[9]. At a distance of 525 pc (Vaytet et al. 2007), this would result in an angle of about 10 arcseconds. The radius of the shell on our frames (in spatial direction, so from top to bottom on the figure) is about 8 pixels. The spatial scale of the CCD is 0.35 arcsec/pixel. Taking into account a binning factor of four in the spatial direction, that means that the radius of the shell is around 11 arcsec, which is consistent with our rough size estimate and thus confirms that it is really the nova shell that can be seen on our images.

[9]An Astronomical Unit (AU) is equal to the mean distance between the Earth and the Sun, approximately 150 million kilometres.

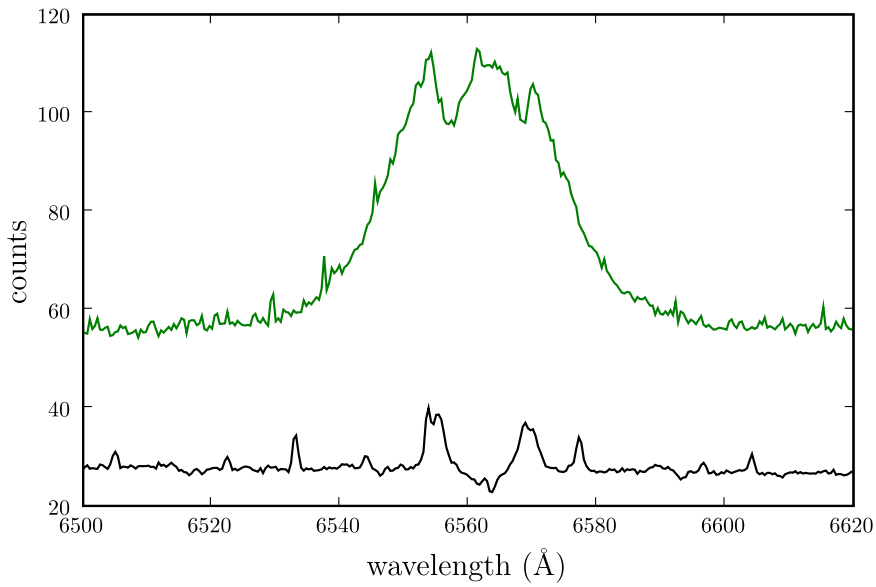

Figure 2.41: *Average spectrum of all (sky subtracted) red DQ Her spectra taken during the first night in green and the average sky spectrum, which is taken in the CCDs regions next to the DQ Her spectrum, in black. The sky spectrum shows emission components at the blue and red sides of Hα λ6563 which are contributions from the nova shell. The other peaks are genuine skylines. Since the position in the nova shell at which the sky spectrum is taken is different from the position of the DQ Her spectrum, the sky subtraction does not accurately remove the nova contribution and even introduces artefacts by subtracting flux at wavelengths where the nova shell contributes to the sky spectrum but not to the DQ Her spectrum.*

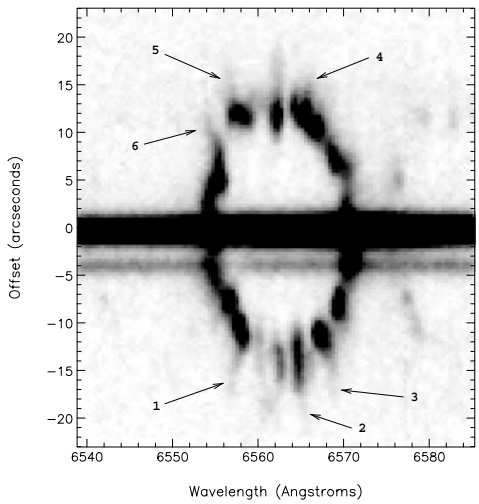

Figure 2.42: *High resolution spectrum of DQ Her, taken from Vaytet et al. (2007). The Hα emission from the nova shell is clearly visible and shows the same pattern as the one we observed (see Fig. 2.40).*

Chapter 3

RXJ1730

3.1 Introduction

Our second target, 1RXS J173021.5-055933 (also known as RXJ1730), was identified as an intermediate polar by Gänsicke et al. (2005). They determine the orbital period $P_{orb} = 925.27$ min and the spin period $P_{spin} = 127.99991(5)$ s, which makes it an IP with a very extreme spin to orbital period ratio. According to the list of known IPs that is maintained by Koji Mukai[1] only one IP has a longer orbital period (GK Per, $P_{orb} = 2875$ min) and only two IPs have a faster spinning white dwarf (AE Aqr, $P_{spin} = 33$ sec, and possibly DQ Her, $P_{spin} = 71$ or 142 sec). The only IP with a lower P_{spin}/P_{orb} ratio, AE Aqr, is known as a propeller system, in which most of the material that flows from the secondary to the white dwarf is flung away by the field lines instead of accreted on the white dwarf. This justifies our attempt to study RXJ1730 via fast spectroscopy. Gänsicke et al. (2005) conclude that it is likely that the white dwarf is not rotating at its equilibrium period, which would imply that the system is in a short-lived phase in its evolution. In a periodogram both the white dwarf spin period and the first harmonic are found, which suggests that the two magnetic poles contribute to the light curve.

X-ray, UV and new optical observations were presented by de Martino et al. (2008). The X-ray light curve was found to modulate at the spin frequency of the white dwarf. No modulation was detected in the far-UV light curve. In the near-UV and optical light curves, the first harmonic of the spin frequency dominated. They estimate the inclination of this non-eclipsing system between 50° and 70°.

Butters et al. (2009) recently looked into the polarisation of the light of RXJ1730. They reported the strongest variability in the circular polarisation over the spin period that is

[1] K. Mukai's IP webpage `http://asd.gsfc.nasa.gov/Koji.Mukai/iphome/iphome.html` lists all known IPs and candidates with a rating on a scale of 1 to 5 that expresses the certainty level that the star is really an IP. In the period comparison presented here, the list of July 2008 was used and only IPs with a rating of 5 ('ironclad', 24 systems) or 4 ('confirmed', 9 systems) are considered.

measured in an IP to date (about 8% peak-to-peak in the B-band) and conclude that the system is likely to have a very a high magnetic field.

3.2 The quest for photons of RXJ1730

3.2.1 Introduction to L3CCDs

Since RXJ1730 has a B-magnitude of only 16.3 (Gänsicke et al. 2005) – around 2 magnitude fainter than DQ Her – we run into trouble when we want to do high speed spectroscopy with a 4m-class telescope like the WHT. With a standard CCD, the signal level would be buried under the readout noise (RN). The RN is added in the last step of a CCD readout by the output amplifier, which converts the small charge in each pixel into a voltage. An extra disadvantage of standard CCDs is the readout time between two exposures, which can easily be tens of seconds. Possible solutions using standard CCDs are binning and windowing, as discussed earlier in Section 1.2.2. Another possibility to tackle the limitations set by RN is to use Low Light Level CCDs (L3CCDs) which have been developed in the last couple of years.

An L3CCD resembles a standard CCD but has two important additional components. The first is a frame transfer buffer, which already appeared in other CCD designs prior to L3CCDs as well. It allows on chip storage of an image so that as soon as an exposure is finished, it can quickly be shifted to the buffer and the next exposure can already start while the previous one is still being read out. This strategy reduces the dead time between two exposures to less than a tenth of a second to avoid the loss of precious telescope time that one encounters when using standard CCDs. The more innovative extra component is an electron multiplication part. L3CCDs are therefore regularly called EMCCDs. The electron multiplication part consists of a series of serial stages in the output register that are clocked with a higher voltage than is necessary for simple charge transfer. In these stages, the charge-carrier electrons are accelerated by the large electric fields such that additional electrons can be generated by impact ionisation. A single electron can thus lead to an avalanche of hundreds to thousands of electrons, which will make the RN that is added afterwards negligible. Even single photons will now tower over the RN. A schematic representation is given in Fig. 3.1.

The disadvantage of an L3CCD is that the gain of the system, which is in this context defined as the number of electrons that is read out by the CCD for one initial photo-electron, does not have a constant value. Because each electron has a certain probability, say P, to create an extra electron in a certain stage of the multiplication process, the gain is stochastic in nature. If we consider a multiplication register with r stages, the mean gain g equals

$$g = (1 + P)^r \,.$$

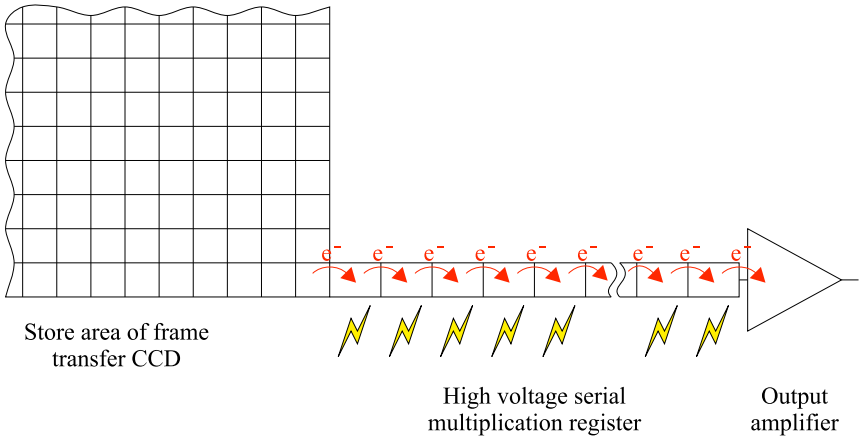

Figure 3.1: *Schematic representation of an L3CDD. After an exposure has been taken, the image is shifted from the exposed CCD area (not shown) to an on chip buffer (left) so that the next image can be exposed while the previous is being read out. The charge in every pixel gets amplified in a multiplication register such that even a one photon input signal will result in a much higher final signal than the readout noise added in the output amplifier. Figure taken from Tubbs (2003).*

The real gain can lie anywhere in the range from 1 up to 2^r. The probability p is usually of the order of 1% and can be controlled by adjusting the voltages that are applied in the multiplication register. The variance of the gain increases the variance of the output, which is a factor 2 larger than when a normal CCD is used (see e.g. Marsh 2008). The S/N in one pixel is

$$\frac{C}{\sqrt{(R/g)^2 + 2C}}$$

with C the number of photons detected in the pixel and R the readout noise. For a normal CCD this would be

$$\frac{C}{\sqrt{R^2 + C}}.$$

This shows that the extra variance that is introduced by the stochastic gain is equivalent to a drop of 50% in quantum efficiency. The gain g is usually large (hundreds or even thousands) which leads to the conclusion that an L3CCD will be more efficient once $C < R^2$. In such a low light regime, a normal CCD will also have lost a factor 2 or more in S/N due to the non-negligible RN contribution. Mind that for large g, the S/N of an L3CCD does not get worse for lower C. This makes it a suitable device to observe in the photon counting regime, where only 1 to a few photons are expected per pixel. This is exactly what one needs to do ultrafast spectroscopy.

The gain variability leads to a probability distribution of possible count values on the CCD.

For an input of n photo-electrons, the final distribution is approximately

$$p(x) = \frac{x^{n-1} \exp(-x/g)}{g^n (n-1)!}$$

(Basden et al. 2003).

Another property of L3CCDs is that clock induced charges (CICs), which are produced in all CCDs, are now visible due to the large gain. CICs originate from spuriously created electron-hole pairs during the clocking process in the CCD readout. The effect is that several bright pixels will be randomly distributed over the chip.

3.2.2 L3CCD observations of RXJ1730

The ISIS spectrograph of the WHT has recently been equipped with two almost identical L3CCDs: QUCAM2 on the blue arm and QUCAM3 on the red arm. These chips[2], with 1k by 1k pixels, can transfer a full frame to the buffer in 20ms, allowing to observe sequences of hundreds of frames with essentially no dead time. They are tuned for observations with exposure times of up to 15s. The active part of the CCD is continuously illuminated, also when an exposure is being shifted to the buffer. The shutter remains open all the time, because such high shutter speeds could potentially damage the shutter and to avoid unequal illumination as mentioned in Chapter 2.

RXJ1730 was observed with ISIS during the nights of 11-13 July 2008. It was the first science run which made use of the QUCAM2 detector. At that time, QUCAM3 was not yet installed, so the red arm of the spectrograph was operated using the normal CCD. Our dataset consists of 13992 blue spectra with an exposure time of 1.4s to 2.0s and 556 red arm spectra with an integration time of 32s to 64s. A summary of the observations is given in Table 3.1. The blue spectra are taken with the R1200B grating. They have a spectral resolution of 1.5Å and cover a wavelength range of 4300-4700Å. The red spectra are made with the R600R grating, have a spectral resolution of 0.45Å and a wavelength range of 6100-6950Å. The data were stored in one `.fits` file per exposure. An exposure is defined as the group of spectra that are taken between two shutter closures. Typically, a few hundred frames are taken in each run. An example of a frame is shown in Fig. 3.2. This time, not only the target is observed, but also a nearby (invariable) field star. This field star will be used like a comparison star is used in photometry to correct for atmospheric effects. Observing a second star with a long slit spectrograph unfortunately comes with a trade-off. When no comparison star is observed, a parallactic slit angle is used such that the elongation of the image of the star by atmospheric dispersion[3] is along the slit. When one

[2]Information on the L3CCDs used at the WHT can be found at `http://www.ing.iac.es/Astronomy/instruments/isis/L3spectroscopy_v4.html` and pages linked from there.

[3]The atmosphere elongates the image of a star due to the blue part of the spectrum being refracted stronger than the red part. This effect is proportional to the airmass at the time of observation and will thus be quite substantial if one follows a target for many hours.

Date	UT	Instrument	Grating	Exp. time	Number
11-12/07/2008	22:05 - 01:40	ISIS blue arm	R1200B	2.0s	5640
		ISIS red arm	R600R	32.0s	290
12-13/07/2008	21:16 - 00:57	ISIS blue arm	R1200B	2.0s	5322
		ISIS red arm	R600R	32.0s	17
		ISIS red arm	R600R	64.0s	161
13-14/07/2008	23:18 - 01:06	ISIS blue arm	R1200B	2.0s	2646
		ISIS blue arm	R1200B	1.4s	384
		ISIS red arm	R600R	64.0s	88

Table 3.1: *Summary of our RXJ1730 dataset. The observations were performed with the ISIS spectrograph at the 4.2m William Herschel Telescope operated at the Observatorio del Roque de los Muchachos, La Palma, Spain. The blue arm was equipped with the L3CCD QUCAM2, the red arm with the conventional CCD.*

places two stars in the slit, the slit angle is fixed by the position of the stars and loss of light due to an elongation component perpendicular to the slit cannot be avoided. The spectrum of the comparison star can clearly be seen on the left side of Fig. 3.2. The spectrum of RXJ1730 itself is much weaker and located on the right. With a conventional CCD, the spectrum would totally have been lost in the noise. The spectral and spatial directions, as well as the bias region locations are equivalent to the case of DQ Her (Fig. 2.5). Each night, one or more flux calibration stars have been observed as well. These are stars with a well known spectral energy distribution, which we will use during the reduction to convert the number of counts in a CCD into an actual flux value.

3.2.3 Data reduction

Broadly speaking, the reduction procedure is the same as the one presented in the chapter on DQ Her. There are however some complications that arise from the low light level of the current target on the blue spectra. In addition, there are now spectra from a flux calibration star and an on chip comparison star available which allow us to perform a flux calibration for the spectra of both arms. These differences will be spotlighted in the following sections.

As discussed by Basden et al. (2003), L3CCD observations can sometimes be reduced without any variance by applying threshold strategies. When the detector is used in a photon counting regime, such that a maximum of one photon is expected per pixel, one can just treat all pixels with a value above a certain threshold as a pixel that caught one photon, and the others as pixels without photons. For regimes in which every pixel catches a few photons, thresholding strategies exist as well which can lead to a better S/N than a standard reduction method. For higher count levels, a normal reduction method as used for

Figure 3.2: *Example CCD frame taken with the L3CCD 'QUCAM2' on ISIS's blue arm. The spectrum of the comparison star is seen on the left, the spectrum of the target RXJ1730 on the right. RXJ1730 is so faint that it is not possible to trace the spectrum accurately on one frame.*

standard CCDs has to be be applied, with the drawback of having a variance that is twice as high as for a standard CCD, as discussed earlier. The count levels of our target star might qualify for a thresholding scheme, but the count levels of the comparison star are certainly too high. We therefore adopt the usual normal and optimal extraction routines, taking into consideration the doubled variance due to the stochastic nature of the gain.

We start off with a brief section on the bias subtraction and flatfielding in Section 3.2.3.1. Next, we determine the average gain of the L3CCD in Section 3.2.3.2. We then discuss the extraction of the slightly curved and tilted spectra in Section 3.2.3.3. The flux calibration will be discussed in Section 3.2.3.4. Setting up the extraction strategy, we will detect an odd telescope wobble, which we will further analyse in Section 3.2.3.5.

3.2.3.1 Bias subtraction and flatfielding

For the spectra taken with ISIS's blue arm, the bias level is subtracted by subtracting a constant determined from a bias region on every frame, as in the case of DQ Her. The bias frames of the red spectra show some structure. We therefore first subtracted a pixel-by-pixel mean of the available bias frames and then subtracted the usual constant to account for slight frame-to-frame differences in the bias level.

The flatfielding procedure we applied was a bit less sophisticated than explained in Section 2.2.2.5 because there were no twilight flats available. We thus followed the approach outlined in the latter section but without the correction for variations in sensitivity along

the spatial axis.

3.2.3.2 Gain determination

To determine the gain, we use bias frames and bias regions. These have no illumination, so the number of electrons will be zero in most pixels, except in some randomly distributed pixels because of clock induced charges. The number of input electrons will thus be zero or one in each pixel. The probablility distribution for the output of 1 input electron, which is given by the equation for $p(x)$ mentioned at the end of Section 3.2.1 for $n = 1$, is

$$p(x)_{n=1} = \frac{\exp\left(-x/g\right)}{g}.$$

The natural logarithm of the distribution will thus have a slope of $-1/g$. Figure 3.3 shows a histogram of the pixel values of the bias regions of all spectra taken during the first night. On the X-axis, the pixel values are shown, with the mean value of the lowest 90% of the pixels – the bias level – subtracted. This results in a gaussian distribution around zero with the RN as full-width-half-maximum, which comes from the pixels with no charges, and a linear tail that extends to very high values, produced by the pixels with one clock induced charge. The slope of this tail is $-1/g$, which allows us to estimate the gain at 172 ± 8. The RN derived from the width of the gaussian is 5.4 ± 0.6.

Apart from bias regions of science frames, also bias frames and dark frames can be used to determine the gain. Images with a lot of pixels that caught more than one photon are not useful because the distribution function would be much more complex: it would result in a distribution that is a sum of distributions $p(x)$ (see formula at the end of Section 3.2.1) for different values of n.

The gains determined from different regions on different frames are listed in Table 3.2 for the three nights. The dark frames of night 3 might not be completely dark after all, which can result in a number of pixels with more than 1 photon, and thus a misleading gain determination because our system expects zero or one photon per pixel. The gain determinations do not give exactly the same results, which is likely due to slight variations in the gain and because of a certain error margin that obviously has to be taken into account. Since a few percent differences in the gain won't have a significant influence on the extracted spectra (it will only slightly change the error bars), we chose to adopt the constant value of 170 as the gain for the further reduction. The value at the earlier mentioned website of the Isaac Newton Group of Telescopes is 160, which seems a little too low but such a difference is not surprising since a small change in the voltages applied in the serial register can drastically change the final gain.

Frame	Region	Gain N1	Gain N2	Gain N3
science	overscan	172	170	172
bias	whole frame	N/A	175	170
bias	overscan	N/A	167	169
dark	whole frame	174	175	204
dark	overscan	169	177	173

Table 3.2: *Gain values of QUCAM2 determined from different types of images and image regions. The uncertainty on the gain values is about 8.*

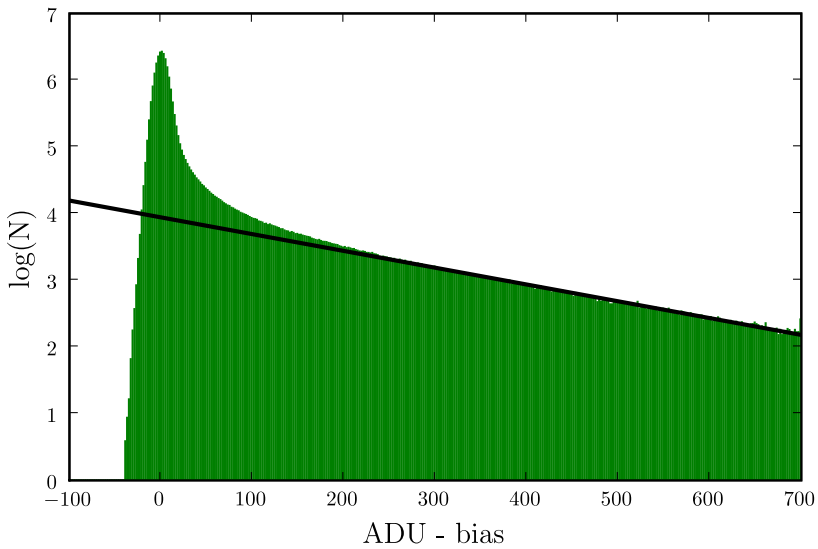

Figure 3.3: *Log-histogram of the pixel values minus the bias level for the overscan regions of the science frames of the first night. All pixels are expected to have had a charge of 0 or 1 electron. The gaussian distribution represents the pixels with a zero charge. The pixels with a charge of one electron give rise to the tail that extends to very high count values. The slope of a linear fit to this tail is* $1/g$ *and thus allows to determine the gain.*

3.2.3.3 Extraction of curved and tilted spectra with low count levels

In the case of DQ Her, the trace of the spectra was well aligned with the columns of the CCD. This time, this is no longer true. The solution is to fit a low order polynomial to the position of the spectrum on the CCD and extract the spectrum along this polynomial instead of along the columns of the chip. Marsh (1989) describes an adapted version of the optimal extraction presented by Horne (1986) to cope with this extra complication. It is implemented in the `PAMELA` commands `track`, `profit` and `optext`. `Track` fits a polynomial (called the *trace*) to the spectrum curve on the CCD image. `Profit` computes the profile of the amount of flux in the different pixels with light of the same wavelength, along the polynomial trace. `Optext` extracts the spectrum using that flux profile. The other `PAMELA` routines that are used in the extraction, like `regpic` to determine the sky and object regions and `skyfit` to interpolate the sky level in the object region, also offer the possibility to work along a trace.

The reduction of the spectra of the comparison star and the target star normally proceed independently and in an identical way. The low flux level in the target spectra however make it hard to determine an accurate trace and profile from one single image. In a first attempt to solve the issue, we made a stacked image by summing the hundreds of frames of one exposure and determined a trace and profile for both stars from that image. These traces and profiles were then used to extract the individual frames. Unfortunately, the result was poor. Comparing individual frames, we found out that the position of the spectra changed on very fast timescales in the spatial direction. This drift in the extract position is further explored in Section 3.2.3.5.

We thus had to come up with a strategy that could account for the rapidly changing spectrum location on the CCD. After checking many alternatives, the approach that was finally adopted for the extraction of the blue arm spectra is the following:

1. determine a 3rd order polynomial trace and a profile for both stars from a stacked image;

2. tweak the first order parameter of the trace (i.e. the extract position, not the curvature parameters) of the comparison star on each frame;

3. shift the frames to align the spectra of the comparison star, and thus also the spectra of the target assuming that the offset between the two does not vary during on short timescales;

4. make a new stack using the shifted spectra and recompute the traces and profiles from the new stack;

5. use these traces and profiles to extract the spectra from the original frames, tweaking the trace of the comparison star and applying the same shift to the trace of the target

star and to the chosen sky and object regions[4].

The extraction of the red spectra was less cumbersome. Due to the 15 to 30 times longer integration times, the signal in the spectra of the target star was high enough to follow the standard procedure of determining the trace and profile per frame for the two stars independently.

3.2.3.4 Wavelength and flux calibration

The wavelength calibration is completely analogous to the case of DQ Her. This time there are also spectra taken of flux standard stars, which are stars with a well-known flux per wavelength profile. HZ44 was observed during all the nights, so we used this star to flux calibrate our spectra.

The integration time clock of ISIS only starts after the previous image is read out from the buffer on the CCD, but the next image is already being taken at that time because the shutter is not closed in between two frames. The readout time for our window and binning settings, 0.8s, thus had to be added to the integration times mentioned in the headers of the spectra.

Flux calibration routines are built into `MOLLY` and can be applied directly after the wavelength calibration. By fitting a high order spline function to the spectrum of the flux star (to avoid using small spectral features of the star) and comparing the fitted CCD count levels with the tabulated fluxes[5], one can define a relation between counts and flux (e.g. expressed in mJy) at all wavelengths. This relation can then be used to flux calibrate the science spectra of both the comparison and target star.

The last step in the flux calibration is to correct the flux levels for fluctuations due to slit losses and seeing variations. These can be estimated by comparing the intensity of all narrow slit comparison star spectra with a wide slit comparison star spectrum. Wide slit spectra are taken once per night. They have a lower spectral resolution but catch all the light of the star whereas slit losses easily occur when one uses a narrow slit. Per night an average of the available wide slit spectra is made and used to correct the flux of the normal narrow slit spectra. The correction is determined by fitting a low order polynomial, in this case just a constant, to the ratio of the average wide slit to the narrow slit comparison star spectra. For each narrow slit comparison star spectrum, this results in a polynomial (here just a constant) which expresses the factor of the light that was lost at different wavelengths. The correction is then applied to the target spectra by multiplying the flux calibrated spectra by this polynomial.

[4]In theory, this last step is equivalent to extracting the shifted frames without tweaking the traces, but though this would have been easier, using the original frames is more accurate as the shifted frames are partly interpolated because they were shifted over a non-integer number of pixels.

[5]Calibration spectra of standard stars can be found at `http://www.eso.org/sci/observing/tools/standards/spectra/stanlis.html`.

3.2.3.5 Drifting track position

The variations in the position of the spectra on the L3CCD over the three nights are illustrated by Fig. 3.4. The long term variations within one night and between the nights are a normal consequence of the movements of the telescope while it is tracking the star on the sky. The small scale variations however are not supposed to be there. They are shown in detail on Fig. 3.5 for the blue spectra of night 1 and on Fig. 3.6 for the first 250 spectra of that night. We clearly see a periodic wobble in the extract position with a period of around 70s, which is likely due to an error in the drive mechanism of the telescope, which can be the result of a bad telescope balance. The observed drift over 5 to 6 pixels is equivalent to a 1 to 1.2 arcsecond movement of the telescope along the slit direction. We don't know the amplitude of the movement in the direction perpendicular to the slit, but as the slit is only 1 arcsecond wide, lightlosses are already expected when the telescope would move over a few tenths of an arcsecond off target. The light curve of the comparison star is expected to be flat, apart from changes in the atmospheric conditions. The light curve of the blue spectra of the first night and a zoom on the first 250 spectra are shown in Figs. 3.7 and 3.8. There are short term variations that are hard to explain by seeing differences, suggesting that we indeed suffer from the expected light losses.

The wobble is resolved in our data because of the 2s integration times of our spectra. When one uses longer exposure times, the spectrum would be smeared out. This explains why the drift is not easily seen on normal spectroscopy, though it lowers the S/N because more pixels are used to collect the same amount of light, in addition to possibly enhanced slit losses. The extract position of the red spectra (see Fig. 3.9) only drifts over 1 pixel on short timescales, which is the result of this smearing effect.

We reported our findings to the WHT staff, who confirmed the existence of the problem and promised to look into it in the near future.

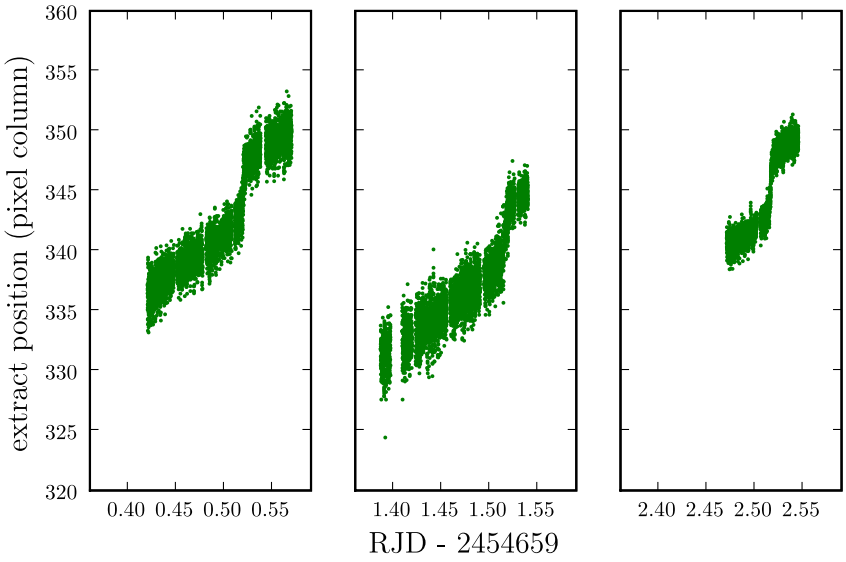

Figure 3.4: *Extract positions of the blue spectra of all three nights. The long term trends over the three nights are not unusual but the short term variations are surprising.*

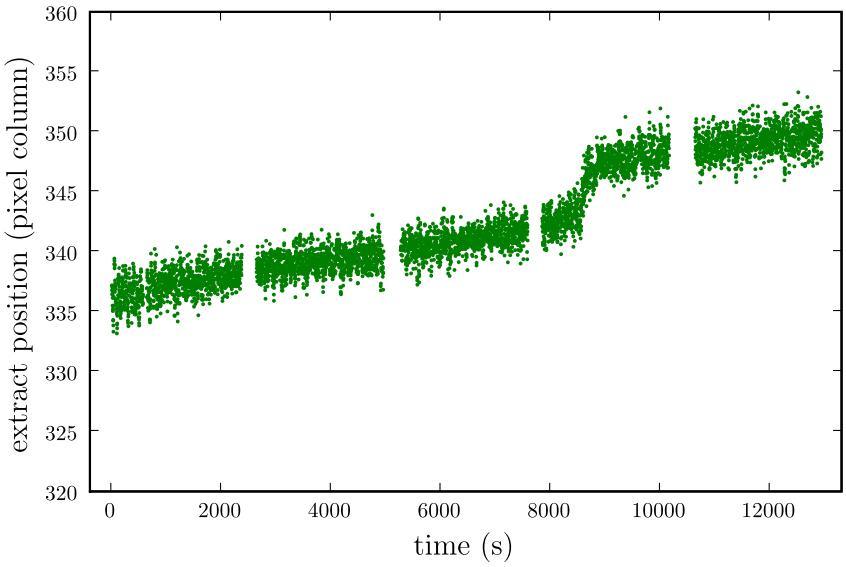

Figure 3.5: *Extract positions of the blue spectra of the first night. The variations on short timescales complicate the data reduction process and are probably due to a drive error of a telescope.*

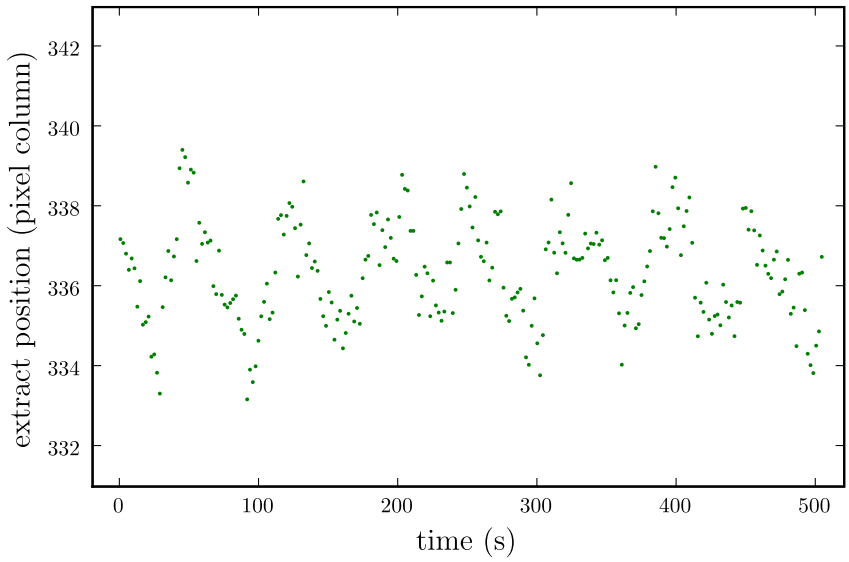

Figure 3.6: *Extract positions of the first 250 spectra of the first night. A variation with a period around 70s is present.*

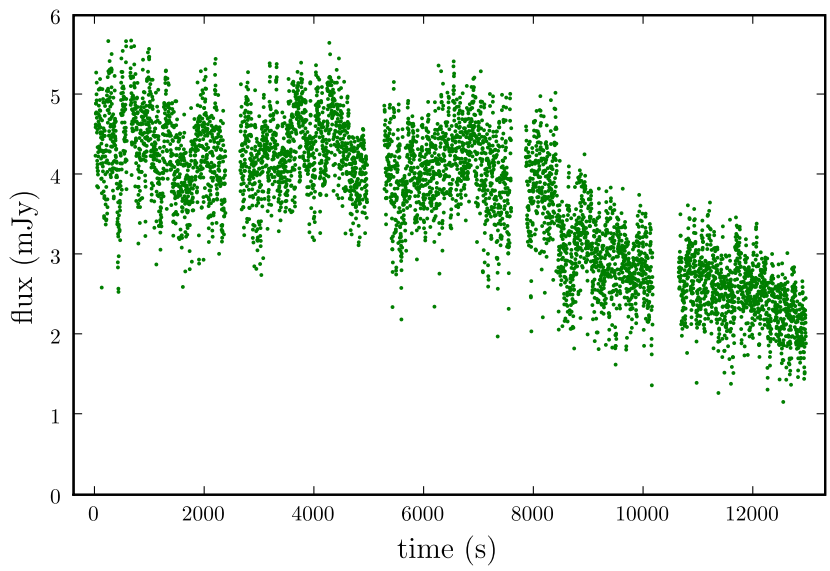

Figure 3.7: *Light curve of the continuum flux of the comparison star, which is supposed to be intrinsically unvariable, for the spectra of the first night. Variations in the light curve can occur due to seeing variations, but sine-like periodic variations are normally not to be expected. Due to the telescope wobble seen in the extract positions, the slit of the spectrograph can however slightly shift off target with light loss as a result. The statistical error on the datapoints is around 0.1 mJy, as shown on Figure 3.8.*

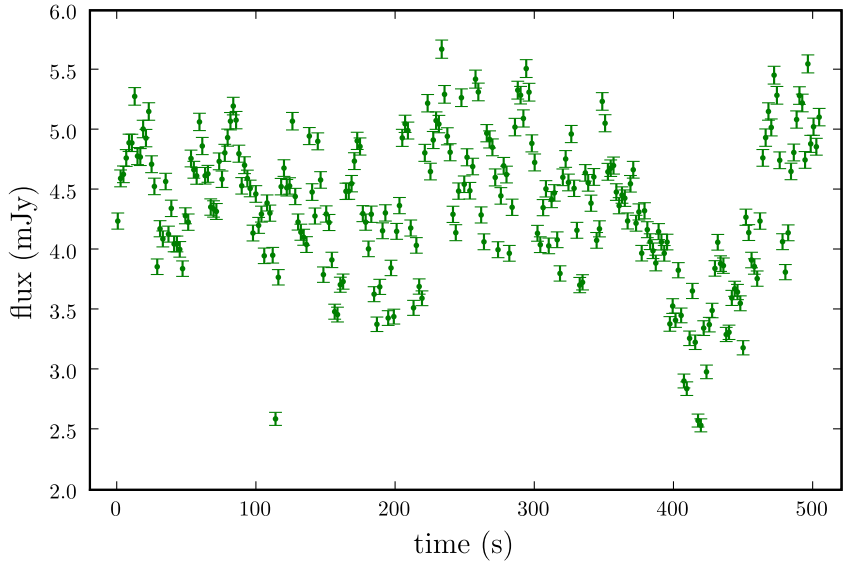

Figure 3.8: *Light curve of the continuum flux of the comparison star for the first 250 spectra of the first night. Some period variation seems to be present which is very likely caused by the telescope wobble.*

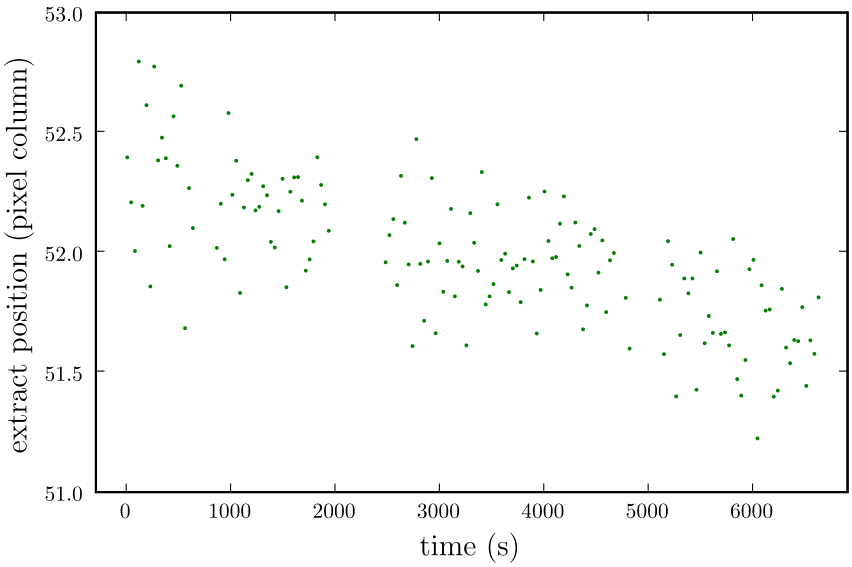

Figure 3.9: *Extract positions of the first 150 red spectra. The same global trend as for the blue spectra is seen but the periodic variations are less resolved because of the larger exposure times of 32s as compared to 2s in the case of the blue spectra.*

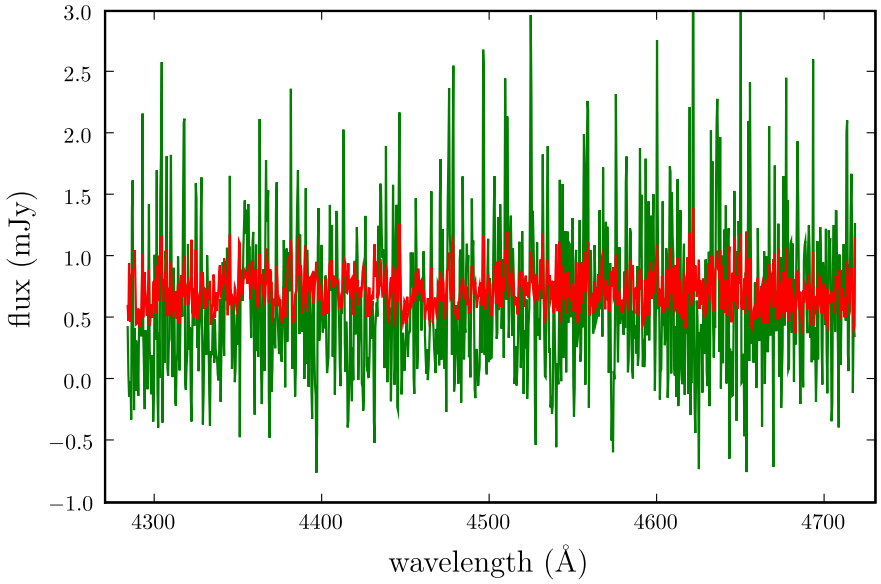

Figure 3.10: *Example blue arm spectrum of RXJ1730. The spectrum is shown in green, the errors in red. Because on average only 2 to 3 photons are incident on each pixel, many individual spectra have to be combined to see the actual spectrum of the star.*

3.2.4 Discussion of the extracted spectra

Figure 3.10 is an example of an extracted blue spectrum. The spectrum is depicted in green, the error estimates in red. No spectral lines can be seen in this spectrum, which is normal because we are dealing with extremely low light levels. On average, 3 to 4 photons were detected per angstrom per second. The exposure time calculator of the Isaac Newton Group of telescopes (ING) which operates the WHT, `SIGNAL`[6], predicts 5 to 6 photons per angstrom per second should be detected. We thus observed about 30% fewer photons than expected, probably due to extra slit losses caused by the telescope wobble that are not expected by `SIGNAL`. The average spectrum is shown in Fig. 3.11. It has a S/N of about 90 in the continuum, compared to 600 for the DQ Her spectra. The HeII line at 4685.75Å is about 20% brighter than the continuum. The only other line that is clearly detected is Hγ at 4340.47Å.

On Fig. 3.12 one can see an example of a red arm spectrum. The flux calibration is not accurate at the blue end of the spectrum and above 6800Å, which gives rise to higher error bars in these regions. The average red spectrum is shown in Fig. 3.13. The total S/N is around 100 in the continuum. Hβ can be seen at 6562.76Å and weak lines from the secondary are expected to be present in what could as well be the noise around the

[6]The ING exposure time calculator, `SIGNAL`, can be found at `http://catserver.ing.iac.es/signal/`. It contains models for the throughput and efficiency of the telescopes and instruments and allows to estimate the signal one would detect from a star with a given magnitude in certain weather conditions.

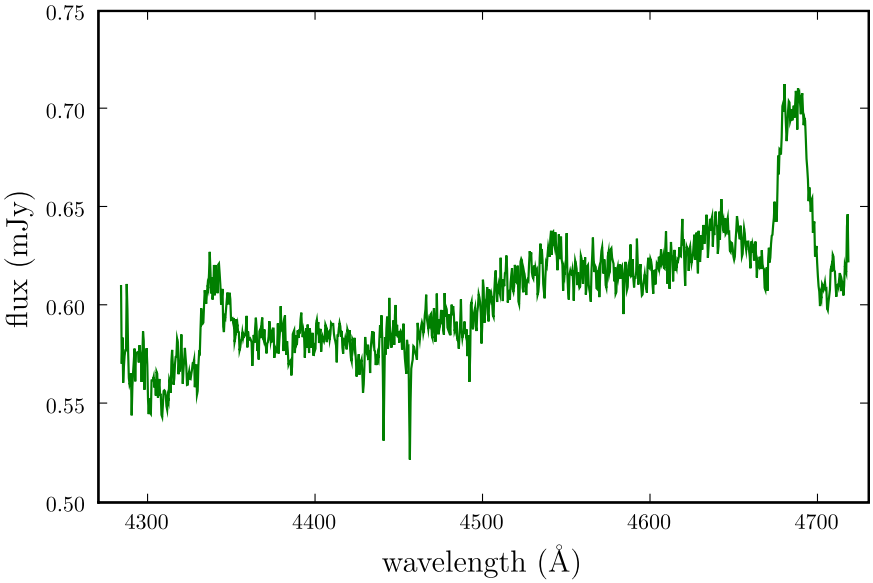

Figure 3.11: *Average blue spectrum of RXJ1730. The S/N is about 80 in the continuum. The HeII λ4686 and Hγ λ4340 lines are visible.*

continuum. We will try to pick these lines up to measure the radial velocity of the secondary in Section 3.3.2.

3.3 The binary orbit of RXJ1730 and the spin of its white dwarf

3.3.1 White dwarf spin period

As in the case of DQ Her, we expect variations in the flux level of the spectra on the spin frequency of the white dwarf, due to reprocessing of X-rays in the disc. A periodogram of the continuum light level of the blue spectra (Fig. 3.14) shows peaks at 675 c/d (equivalent to a period of 128s) and 1350 c/d (equivalent to a period of 256s). Gänsicke et al. (2005) determined the period to be 128s, which is consistent with our results if 675 c/d is the true frequency and 1350 c/d the first harmonic.

Let us revisit DQ Her for a moment. In DQ Her's periodogram (Fig. 2.29), only a frequency at 1217 c/d (period of 71s) was detected. If 142s would be the true period, this would be the first harmonic like 1350 c/d in the case of RXJ1730. The true spin frequency at 608.5 c/d would then be completely absent, which is only possible if two regions of the disc or two poles of the WD contribute in an almost identical way and with an exact 180 degrees phase difference. If the two contributions do not meet these criteria, two peaks would be observed as in RXJ1730.

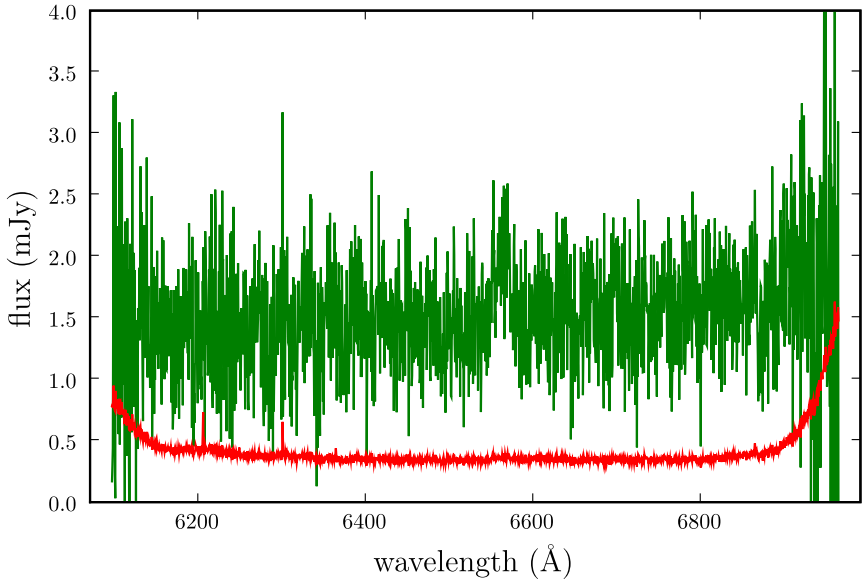

Figure 3.12: *Example red arm spectrum of RXJ1730. The spectrum is shown in green, the errors in red. The integration times are about 15 times longer than for the blue spectra, which results in a S/N of about 4 in the continuum. Hα λ6563 is weakly visible. Due to vignetting at the outer regions of the CCD, the extraction and flux calibration are not accurate at the blue and red ends of the spectrum, as shown by the larger error estimates.*

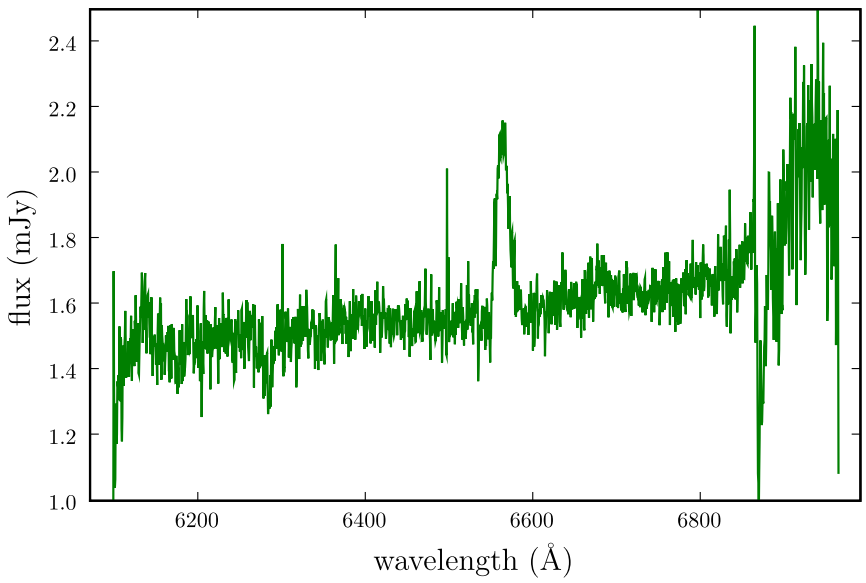

Figure 3.13: *Average red spectrum of RXJ1730. The spectrum has a S/N of around 100 in continuum in the centre of the spectrum. The outer parts are not accurately extracted and calibrated but are of limited use.*

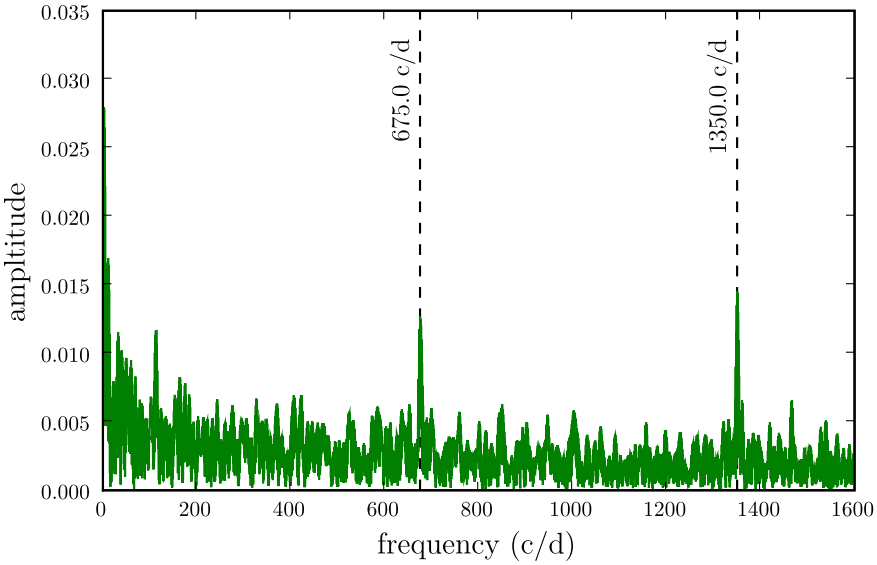

Figure 3.14: *Periodogram of the continuum light level of the blue spectra. Peaks are observed at 675 c/d, which corresponds to the white dwarf spin frequency of 128s, and at 1350 c/d which is the first harmonic of the latter frequency.*

In the case of DQ Her, we were not able to work with the continuum light level because there was no comparison star available to correct for seeing variations and slit losses. Instead, we analysed the light curves of the line fluxes determined after subtracting the continuum level. A similar approach for RXJ1730 leads to the periodogram shown in Fig. 3.15. There is no frequency left above noise level, which indicates that the line does not pulse significantly. The S/N of the average blue spectrum is now around 90, which is a factor 7 lower than for DQ Her. Furthermore, the HeII λ4686 line is only around 20% above the continuum, while DQ Her showed lines up to 80% above the continuum. These two facts are a very plausible explanation for the undetectability of the line pulsations. By adding an artificial line flux variation with the amplitude of the pulsation seen in DQ Her (i.e. $\approx$ 3% of the line flux) to the light curve of RXJ1730, it was found that a DQ Her-like reprocessing effect would not be detectable in the Fourier transform of the HeII line flux of RXJ1730.

Unfortunately, the range of analysis methods we can apply is now very limited. Spin trails will not show any pulsations in the lines, and Doppler maps are out of the question because the phase coverage is too low due to the orbital period of more than 15 hours. In the next section, we will nonetheless try to get an insight in the orbital parameters by attempting radial velocity determinations.

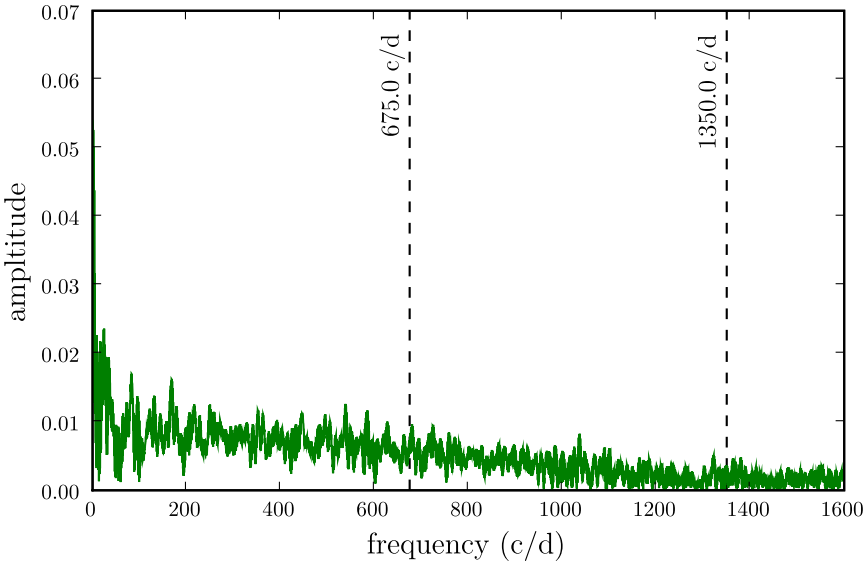

Figure 3.15: *Periodogram of the line flux of HeII λ4686. After subtraction of the continuum variations, the spin frequency of the white dwarf is not detected anymore.*

3.3.2 Radial velocity determinations

To get an idea about the basic parameters of the binary, it would be a good start to derive the radial velocity of the white dwarf and its disc on one hand and of the secondary on the other hand. The white dwarf and the accretion disc can be traced by looking at the HeII or Hα lines. The secondary is expected to have left a signature of weak absorption lines in the red arm spectra.

The signal-to-noise ratio of one blue spectrum is not high enough to see a spectral line, needless to say that it is not high enough to measure the Doppler shift of the line to determine a radial velocity. The long orbital period however allows us to group sequences of several hundreds of blue and tens of red spectra. We grouped the blue and red spectra into 4 spectra for the first night, 4 for the second and 3 for the third. Since a rotating disc is expected to produce a double peaked emission line, we fitted a double gaussian to the broad HeII λ4686 and Hα λ6563 lines to determine the radial velocities. To start off, we kept the separation between the two gaussians as a free parameter. For Hα, values between 360 and 440 km/s were obtained. A separation of 400 km/s was adopted for the final fits. In the case of HeII, the free separation parameter returned values between 560 and 640 km/s, and a value of 600 km/s was fixed for the fits. It is not surprising that the HeII line is a little broader. It requires 54.4 eV to further ionise HeII into HeIII, but only 13.6eV to ionise H. The HeII lines are thus produced closer to the hot white dwarf and therefore have higher velocities in their Keplerian orbit. The double gaussian fits are shown in Fig. 3.16.

Because the orbital period is known to be 925.27 mins, we can draw a sinusoidal radial

velocity curve through the measured velocities even though we only have 11 radial velocity determinations per line. The radial velocity curves are depicted in Fig. 3.17. For Hα, the best fit gives a radial velocity amplitude of $K_1 = 137 \pm 8$ km/s and a systemic velocity of $\gamma = 46 \pm 7$ km/s. From the HeII radial velocities, we found $K_1 = 136 \pm 19$ km/s and $\gamma = -20 \pm 16$ km/s. The fitted phase offset was identical up to less than 0.01 orbital cycles.

To trace the secondary, we tried to cross correlate template spectra of a K0V[7] star (HD 222366) with the observed spectra in a few wavelength regions in which no clear lines from the white dwarf or disc are visible. The spectrum of the template star was artificially broadened to mimic the rotational broadening of the lines of the secondary star, which we guessed at a typical value of 50 km/s. The radial velocity of the template star (≈ -32 km/s, Famaey et al. 2005) was subtracted from the velocity offset returned by the cross correlation to get the radial velocity of the secondary. Because the absorption lines of the secondary are very faint, we grouped the spectra into 1 spectrum for the first night, 2 for the second and 2 for the third. Even then, the determined velocities are not accurate at all. By eye it is impossible to recognise a single spectral line of the secondary star in the spectra. The correlation profile of the last spectrum was nearly flat. We therefore didn't use its result. With only 4 data points left, we had to use the phases as fitted to the Hα and HII lines to get rid of one free parameter by using the knowledge that the phase difference between the primary and the secondary is always 0.5 orbital cycles. Only K_2 and γ were left free, and determined to be $K_2 = 136 \pm 19$ km/s and $\gamma = 13 \pm 18$ km/s. The result is plotted in Fig. 3.18.

Though our values should be interpreted with caution because we had to group many spectra to be able to determine radial velocities such that only a few data points were left to fit the RV curve, it is interesting to note that the values we found for K_1 and K_2 are very close to being equal, which is not common. As mentioned in the introduction, unstable mass transfer is expected for $q = \frac{K_2}{K_1} \gtrsim 1.26$ (Warner 1995) when the secondary is a main sequence star. The mass ratio we find for RXJ1730 is $q = 0.99 \pm 0.15$. Assuming circular orbits, the masses of the two stars can now be estimated using the mass function (e.g. Hilditch 2001, Chapter 6):

$$M_{1,2} \sin^3 i = (1.0361 \cdot 10^{-7}) K_{2,1} (K_1 + K_2)^2 P$$

in which the mass is expressed in solar masses, the velocities in km/s and the period in days. The resulting masses in function of the inclination of the system are $M_1 = (\sin^{-3} i) \cdot 0.67 \pm 0.12 M_\odot$ and $M_2 = (\sin^{-3} i) \cdot 0.67 \pm 0.08 M_\odot$. de Martino et al. (2008) found the inclination to be between 50° and 70°. The maximum inclination leads to lower limits for the masses of the two stars: $M_{1,min} = 0.81 \pm 0.15 M_\odot$ and $M_{2,min} = 0.81 \pm 0.10 M_\odot$. The maximum mass of the white dwarf is set by the Chandrasekhar limit: $M_1 < M_{Ch} \approx 1.4 M_\odot$.

[7] A star with spectral type K0V is a main sequence star that is slightly cooler, lighter and smaller than the Sun.

The inclination is therefore $i \gtrsim 46^\circ$. Our results are in agreement with the recent X-ray study of IPs by Brunschweiger et al. (2009), which suggests that the mass of the white dwarf is $M_1 = 1.08 \pm 0.07 M_\odot$.

From the formula for the Roche lobe size given in Section 1.1 and Kepler's third law given in Section 1.1.1, the Roche lobe radius of the secondary is found to be $R_{L2} \approx 1.5 R_\odot$. If the secondary is a main sequence star, its mass would have to be around $1.6 M_\odot$ to fill the Roche lobe, which is necessary to get mass transfer via L_1. Given the value of q derived above, this would require the white dwarf to have a mass that is extremely close to M_{Ch}, which is unlikely. Furthermore, Gänsicke et al. (2005) concluded that the spectral type of the secondary should be G6V-G0V. This implies that the mass of the secondary is rather about $1 M_\odot$. The secondary star is thus probably not on the main sequence anymore but in a further evolved evolutionary state in which it is larger than its main sequence volume.

It is now clear that RXJ1730 indeed closely resembles AE Aqr, the only IP with a more extreme ratio of the spin period and the orbital period. Schenker et al. (2002) found that the secondary of AE Aqr is in an evolved state as well. They conclude that AE Aqr has recently passed a phase in which mass is transferred on a thermal time-scale, at rates that are high enough to get steady nuclear burning of the accreted material on the surface of the white dwarf. Such binaries are known as supersoft X-ray binaries. Mass transfer on a thermal time-scale requires $q \gtrsim 1$, which is another link with RXJ1730. Note that the mass ratio lowers due to mass transfer from the secondary to the primary. This implies that the current mass ratio need not be greater than 1 for the binary to have recently passed a phase with mass transfer on a thermal time-scale, but it cannot be to far below 1 either. According to Schenker et al. (2002), a recent phase with a high mass transfer rate also explains the high spin frequency of the white dwarf. AE Aqr was considered to be the first member that was found of a much larger population of post-supersoft binaries. It seems that RXJ1730 is another member of this group.

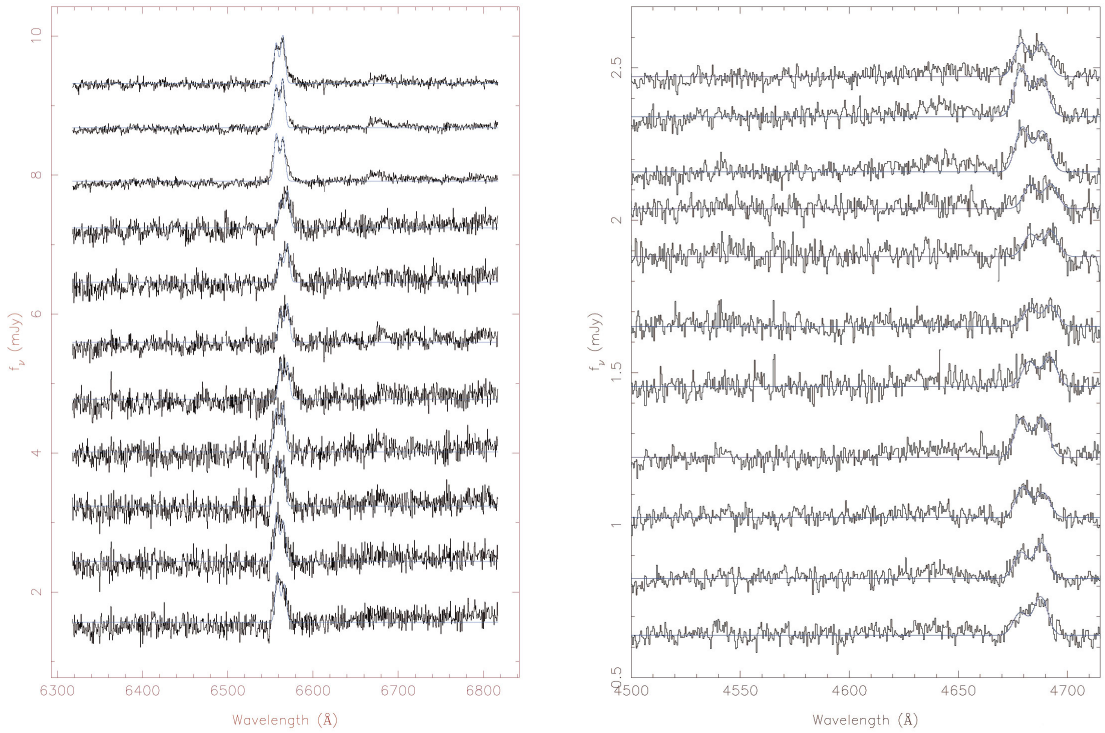

Figure 3.16: *Gaussian fits to the Hα (left) and HeII (right) line profiles.*

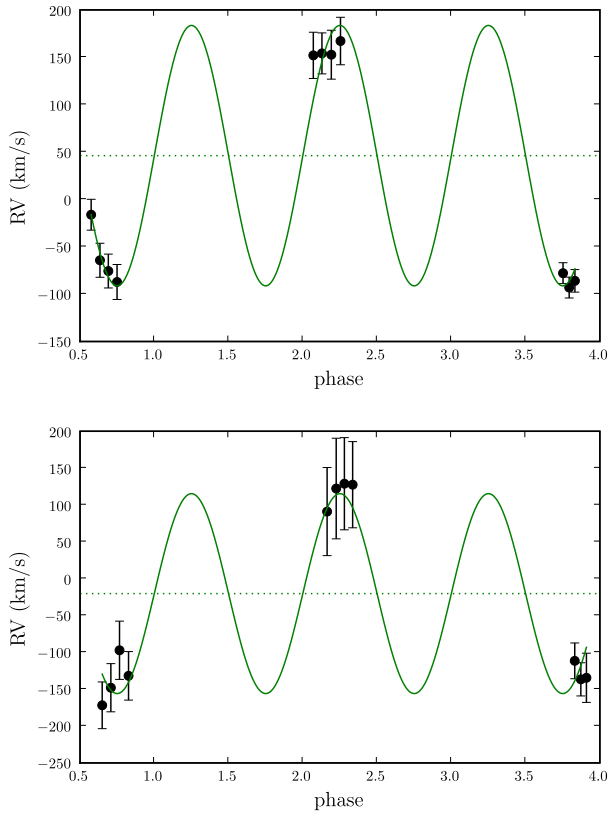

Figure 3.17: *Radial velocity curves of Hα (top) and HeII λ4686 (bottom).*

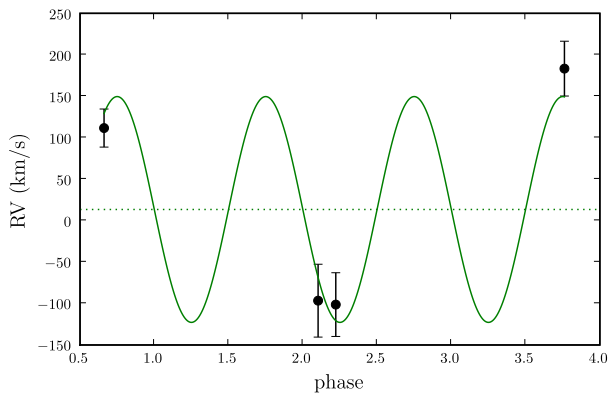

Figure 3.18: *Radial velocity curve of the secondary, determined from cross correlation with a template spectrum of a K star.*

Chapter 4

Conclusions

4.1 Mysterious pulsation pattern and spiral arms in DQ Her

We studied high speed spectroscopy of DQ Her, which was the first intermediate polar to be detected about 50 years ago and therefore serves as the prototype of the class. The observations were performed with the ISIS spectrograph on the WHT. A special low smear drift readout mode was used to reduce the large dead times that limit high speed work with standard CCDs.

We report the first detection of spiral arms in the accretion disc of an intermediate polar. Spiral arms are seen on Doppler maps of Hγ, HeI λ4472 and HeI λ6678. Spirals arise from tidal effects from the secondary star on the accretion disc. They were found before in dwarf novae in outburst and in classical novae. Since spiral shocks are believed to be an alternative mechanism for the transport of angular momentum in a disc besides viscosity effects, they can form a crucial clue in the understanding of disc related accretion processes and other astrophysical phenomena like planet and star formation. If spiral arms can propagate far enough into the disc, as indicated by the simulations of Murray et al. (1999), they can modulate the accretion rate onto the white dwarf. Spirals can therefore possibly explain the sidebands of the spin frequency that are often observed in X-ray and optical light curves of IPs. Until now, it was believed that these sidebands indicate that (part of) the accretion goes via a direct stream from the first Lagrangian point to the white dwarf rather than through the disc. If spiral arms in accretion discs can explain the sidebands equally well, accretion streams might be less frequent than currently thought.

We repeated the study of the pulsation pattern on emission lines from the accretion disc as presented earlier by Martell et al. (1995). We can confirm with greater significance that reprocessed light from the WD beam is only visible in HeII λ4686 when the beam points to the redshifted back side of the disc. The slope of the pulsation on a spin trail does not match with what would be expected from a simple model for a spin period of 71s in which a small region of the disc reprocesses the X-rays from the WD beam. The same

model for two reprocessing spots and a 142s spin period results in a better fit. However, the Doppler map of HeII λ4686 suggests that the line emitting region has a substantial non-Keplerian component. Reprocessing in accretion curtains might be a solution to fit both the slope of the pattern and the absence of observed pulsations in the blueshifted part of the line, but further modelling is required to check this assumption. The lack of a good model thus currently prevents us from settling the discussion as to whether 71s or 142s is the true white dwarf spin period. The spin trails of the HeI and Balmer lines show weak pulsation components as well, with puzzling slopes. We are not aware of any fully developed IP model that can explain our observations. The spin trails clearly provide much more information than can be derived from photometric studies and provide a strong test for enhanced IP accretion models in the future.

Pulsations are still observed at a 71s periodicity in the redshifted wing of HeII λ4686 at orbital phases where the bright spot is in the blueshifted part of the disc. We therefore refute the assertion by Saito & Baptista (2009) that most of the reprocessed light comes from the bright spot, such that the observed 71s periodicity is effectively the beat period.

Finally, we found that the shell that was ejected in the 1934 nova outburst still influences the shape of the Hα line.

4.2 Use of an L3CCD to observe the faint IP RXJ1730

Fast optical spectroscopy was also performed for RXJ1730, which is an intermediate polar with a very extreme white dwarf spin period to orbital period ratio. The system might represent a short lived phase in the evolution of an IP.

The data were obtained with the L3CCD 'QUCAM2' on the blue arm of the ISIS spectrograph on the WHT. Only a handful of papers have been published so far using L3CCD data. It was the first science run with the new CCD on the WHT. An annoying telescope wobble was detected that caused the spectra to drift over the CCD at a period of around 70s, over more than 1 arcsec along the slit. To take full advantage of an L3CCD, one has to limit the exposure time such that only a few photons of the target star are captured in each pixel. This makes it difficult to determine the trace and the profile of the spectrum on one exposure. We set up a reduction strategy that makes full use of an on chip comparison star that is brighter than the target to reduce the target spectra as well as possible. The number of photons detected was approximately 30% lower than expected, which is probably due to extra slit losses caused by the telescope wobble.

The total continuum signal to noise ratio of the spectra was only around 90, which was 7 times lower than for the DQ Her spectra. The strength of the HeII λ4686 line was 4 times lower than for DQ Her. These two factors prevented us from doing the same line pulsation analysis as done for DQ Her. Period analysis of the continuum confirmed the established white dwarf spin period of 128s but no significant pulses were detected in the flux of HeII

λ4686. It was found that a line flux variation with the amplitude of the variation that is seen in the case of DQ Her would not be detectable with our dataset of RXJ1730. It is thus perfectly possible that RXJ1730 intrinsically has the same kind of line pulsations.

We attempted a radial velocity study of the primary by measuring the Doppler shifts of the Hα line on the red arm spectra and the HeII λ4686 line on the blue arm spectra. Radial velocities of the secondary were determined from cross correlation of the red arm spectra with a K0V template spectrum. Unfortunately we had to group many spectra to achieve a high enough S/N. This, together with an unfavourable phase sampling over the orbital period, limits the accuracy of our RV curve fits. The resulting radial velocity amplitudes ($K_1 = 137 \pm 8$ km/s and $K_2 = 136 \pm 19$ km/s) however suggest that the mass ratio of the two stars of the binary is close to 1, which is exceptional and therefore deserves more attention in the future. The fact that the secondary is most likely an evolved star, the high mass ratio and the extreme ratio of the WD spin period to the orbital period suggest that RXJ1730 is a sibling to AE Aqr. The latter system is thought to be a post-supersoft X-ray binary. RXJ1730 is probably another member of this group. With an inclination $i \leq 70°$, the lower limits of the masses of the two stars are found to be $M_{1,min} = 0.81 \pm 0.15 M_\odot$ and $M_{2,min} = 0.81 \pm 0.10 M_\odot$ which is in agreement with other studies.

We can conclude that the L3CCD performed as expected, which illustrates that these CCDs make it possible to do science with only 3 or 4 incident photons per second per angstrom. The spectra of our faint target (B-magnitude of 16.3) would have been buried completely under readout noise with a conventional detector. Unfortunately, the target did not show large enough line pulsations to allow a study like the one we performed for DQ Her, despite the use of an L3CCD. Our work was interesting from a technical point of view because it was the first science use of an L3CCD for high speed spectroscopy at the WHT. We came up with a successful data reduction strategy that can be used in the future to handle similar data, even if the telescope wobble problem we detected cannot easily be solved. Meanwhile, the red arm of ISIS has been equipped with an L3CCD as well, which opens the gate to a wide of range of new possibilities in high-speed spectroscopic applications.

Summary in Dutch

S.1 Inleiding

S.1.1 Cataclysmische variabelen

De meeste sterren aan de hemel zijn in werkelijkheid geen alleenstaande sterren maar systemen met meerdere sterren die gravitationeel gebonden zijn (Carroll & Ostlie 2007, Hoofdstuk 18). Ze bewegen in een baan rond hun gemeenschappelijk massacentrum. Systemen met twee componenten (dubbelsterren) hebben een belangrijke functie in astrofysisch onderzoek. De beweging van de sterren in hun baan maakt het namelijk mogelijk om de systemen te bestuderen met een waaier van technieken die voor alleenstaande sterren niet gebruikt kunnen worden.

Cataclysmische variabelen *(cataclysmic variables, CVs)* zijn nauwe dubbelsterren *(close binaries)* met een witte dwerg *(white dwarf, WD)* die massa aantrekt van de begeleiderster. In ongeveer één vierde van de CVs heeft de witte dwerg een aanzienlijk magnetisch veld (de Martino et al. 2008). De magnetische CVs kunnen opgedeeld worden in twee groepen. Enerzijds zijn er de CVs met een witte dwerg met een magnetisch veld dat groot genoeg is om de spin van de WD te synchroniseren met de dubbelsteromwenteling. Deze CVs worden *polars* genoemd[1]. Anderzijds zijn er de CVs met zwakker magnetische witte dwergen. In deze systemen is de spin van de witte dwerg niet gesynchroniseerd met de beweging van de sterren in hun baan rond het massacentrum van de dubbelster. Zulke dubbelsterren worden *intermediate polars (IPs)* genoemd. In dit werk bestuderen we twee IPs: DQ Her en RXJ1730.

In een dubbelstersysteem oefenen beide sterren een gravitationele aantrekkingskracht uit op massadeeltjes in hun buurt. Beschouwt men de oppervlakken van gelijke potentiaal *(equipotential surfaces)* rond beide sterren, dan kan men de zogenaamde *Roche lobe* definiëren die gelijk is aan de eerste oppervlakken van gelijke potentiaal rond beide sterren die elkaar raken. Materiaal dat binnen de Roche lobe van een ster zit, is gravitationeel aan

[1]Voor een aantal jargontermen, zoals polars en intermediate polars, bestaat geen specifiek equivalent in het Nederlands. Voor zulke woorden zal in deze samenvatting uit noodzaak toch de Engelstalige terminologie gebruikt worden.

de ster gebonden. Wanneer één van beide sterren tijdens haar evolutie groter wordt dan de Roche lobe (doordat de ster groeit of de Roche lobe verkleint), kan materiaal via het raakpunt van de Roche lobes naar de andere ster vliegen.

Indien de aantrekkende ster klein genoeg is (bijvoorbeeld een witte dwerg in een CV), dan zal de getransfereerde materie in een baan rond de ster terechtkomen en door energieverlies (straling) langzaamaan naar de ster toe spiraleren. Om behoud van draaimoment te vrijwaren zal een ander deel van de materie zich verder van de ster verwijderen, waardoor een accretieschijf *(accretion disc)* gevormd wordt rond de ster. De fysica die van belang is voor het gedrag en de evolutie van dergelijke schijven is zeer gelijkaardig aan die van schijven rond T-Tauri-sterren, waarin planeten zich vormen, en aan die van schijven rond de superzware zwarte gaten *(supermassive black holes)* in quasars. Aangezien quasars zich op enorme afstanden van ons bevinden en de schijven rond T-Tauri-sterren dikwijls aan het zicht onttrokken worden door de overblijfselen van de gaswolk waaruit de ster aan het ontstaan is, vormen binaries met accretieschijven een interessant alternatief om de fysische processen die zich in dergelijke discs afspelen, te bestuderen. Vooral het systeem van angulair momentum transport doorheen de schijf is nog niet goed begrepen.

CVs zijn daarnaast mogelijke voorlopers van supernova's van Type Ia. Deze supernova's worden gebruikt om afstanden te bepalen op kosmologische schaal, maar de heersende twijfel over hoe de WDs in CVs precies tot ontploffing kunnen komen, bemoeilijkt deze toepassing. Meer inzicht in CVs kan dus ook voor de kosmologie nuttig zijn.

In een accretieschijf beweegt de materie in eerste benadering op circulaire banen aan Kepleriaanse snelheden, volgens dezelfde wetten die ook gelden voor de beweging van planeten rond een ster. Materiaal aan de buitenkant van de schijf heeft de laagste snelheid, materiaal aan de binnenkant de hoogste. In een CV met een magnetische witte dwerg wordt de Kepleriaanse baan evenwel verstoord door de invloed van het magneetveld op de geïoniseerde materie in de warme schijf. Afhankelijk van de sterkte van het magneetveld wordt schijfvorming gedeeltelijk (bij IPs) of volledig (bij polars) verhinderd. Materiaal wordt via de veldlijnen op de magnetische polen van de witte dwerg getrokken. Hierbij komt energie vrij in de vorm van UV-straling en röntgenstraling. De stralenbundel die op deze manier ontstaat, kan in vele gevallen geobserveerd worden. De bundels kunnen ook, wanneer de oriëntatie gunstig is, onderdelen van het dubbelstersysteem aanstralen. Wanneer de stralenbundel de schijf bestraalt, zorgt dit voor een periodische verandering in de lichtkracht van de IP met de frequentie van de spin van de witte dwerg. Als onderdelen bestraald worden die zelf met een bepaalde snelheid roteren, zoals de begeleiderster of de *bright spot* op de schijf waar de materiaalstroom van de begeleiderster op de schijf valt, kunnen we een variabiliteit waarnemen met een zogenaamde *beat* frequentie. De beat frequentie is gelijk aan het verschil tussen de spinfrequentie en de rotatiefrequentie van de bestraalde materie.

Naast een effect op de continuümstraling heeft de aanstraling ook een effect op de sterkte van absorptie en emissielijnen. De hoog-energetische straling kan immers aanleiding geven

tot extra lijnovergangen door bijvoorbeeld foto-ionisatie. Hogetijdsresolutiespectroscopie is bijgevolg een zeer geschikte techniek om IPs te observeren.

S.1.2 Hogesnelheidsspectroscopie van cataclysmische variabelen

Spectroscopie is één van de meest gebruikte technieken om sterren waar te nemen. In het spectrum van een CV kunnen drie onderdelen vrij goed onderscheiden worden: de accretieschijf, de begeleiderster en de witte dwerg. De beweging van het materiaal in de accretieschijf door middel van het Doppler-effect geeft aanleiding tot zeer karakteristieke dubbelgepiekte spectraallijnen. De schijf straalt voornamelijk op visuele golflengten. De begeleiderster is een hoofdreeksster van een laat spectraal type en straalt voornamelijk op rodere golflengten. De witte dwerg is warmer en is zichtbaar in het UV.

Spectra die genomen zijn met lange integratietijden geven weliswaar nuttige informatie over de samenstelling van het waargenomen object en over het type object, maar laten niet toe om dynamische effecten op korte tijdsschalen te bestuderen. Om de dynamica van een CV spectroscopisch te analyseren, is hogesnelheidsspectroscopie nodig. Dergelijke waarnemingen zijn gecompliceerder dan gewone spectroscopie omdat men door de korte integratietijden veel minder fotonen kan opvangen. Daardoor kan het signaal verloren gaan in de steeds aanwezige ruis. Bovendien hebben standaard-CCDs al snel tientallen seconden nodig om uitgelezen te worden na een waarneming. Als men slechts enkele seconden wil integreren, gaat zo dus enorm veel kostbare telescooptijd verloren. Gelukkig zijn er oplossingen om het uitlezen en verwerken van de gegevens sneller te laten verlopen. De eenvoudigste techniek is het aantal gebruikte pixels te verminderen door een kleiner deel van de chip te gebruiken *(windowing)* of door pixels te groeperen *(binning)*. Voor ultrasnelle toepassingen (integratietijden van enkele seconden of minder) is de tijdswinst echter nog steeds onvoldoende. Daarom werden meer gesofisticeerde technieken toegepast bij de waarnemingen van de twee sterren die in dit werk besproken worden. Bij de DQ Her-observaties werd het tijdsverlies tussen twee beelden beperkt door het toepassen van een speciale uitleestechniek. Voor RXJ1730 werd een vrij recent ontwikkeld CCD-type, een L3CCD *(Low Light Level CCD)*, gebruikt dat naast de uitleestijd ook het ruisniveau minimaliseert zodat zelfs een enkel foton detecteerbaar is, wat een must is bij het waarnemen van lichtzwakke sterren.

S.2 DQ Herculis

S.2.1 Inleiding

De eerste ster die we bestuderen is DQ Her. Deze dubbelster was de eerste intermediate polar die ontdekt werd en was 24 jaar lang de enige ster in deze klasse (Patterson 1994).

Ook al werd DQ Her tijdens de afgelopen 50 jaar vrij intensief bestudeerd, toch heeft het systeem duidelijk nog vele geheimen niet prijsgegeven. DQ Her is ook gekend als 'Nova Her 1934', omdat in 1934 een *nova outburst* plaatsvond in het systeem. Bij deze ontploffing werd een schil van materiaal uitgestoten die nog steeds zichtbaar is rond de dubbelster. De twee componenten van DQ Her draaien rond hun massacentrum in 4:39u. en de inclinatie t.o.v. onze gezichtslijn is 89°, wat impliceert dat de begeleiderster de witte dwerg en zijn accretieschijf eclipseert. De spinperiode van de witte dwerg is nog onderwerp van discussie. De meeste studies concluderen dat de periode 71s is. Een aantal onderzoeken wijzen echter eerder in de richting van een periode van 142s, waarbij de waargenomen 71s variaties in de lichtcurves van DQ Her te wijten zouden zijn aan een contributie van beide magnetische polen met een faseverschil van exact 180 graden.

S.2.2 Hogesnelheidsspectroscopie van DQ Her

Voor ons onderzoek gebruikten we spectra die genomen werden met de ISIS spectrograaf van de William Herschel Telescoop (WHT). De telescoop heeft een diameter van 4.2m en maakt deel uit van het 'Observatorio del Roque de los Muchachos' op het Canarische eiland La Palma. De ISIS spectrograaf is een twee-armig toestel dat toelaat om tegelijkertijd spectra te nemen op blauwe en rode visuele golflengten. De dataset bestond uit 7392 blauwe spectra met een integratietijd van 5s en 2858 rode spectra met een integratietijd van 15s. De blauwe spectra omvatten een golflengtebereik van 4200 tot 5000Å en de rode van 6320 tot 6710Å.

De spectra werden geëxtraheerd uit de CCD beelden en golflengtegecalibreerd met behulp van de datareductiesoftwarepakketten `STARLINK`, `PAMELA` en `MOLLY`. De sterkste spectraallijnen op de blauwe spectra zijn Hγ, HeII λ4686 en Hβ. Op de rode spectra zijn Hα en HeI λ6678 het duidelijkst waar te nemen.

S.2.3 Doppler tomografie van DQ Her

Om inzicht te krijgen in de structuren die bijdragen tot de vorming van de verschillende lijnen gebruikten we Doppler tomografie. Omdat de spectra genomen werden op steeds verschillende orbitale fases *(orbital phases)* van de IP, beschikken we in feite over waarnemingen die het systeem van steeds verschillende kanten bekijken. Als we aannemen dat al het materiaal min of meer op circulaire Keplerbanen beweegt, laat deze informatie, in combinatie met de waargenomen Dopplershifts op al die verschillende posities, toe om een 2D-afbeelding van het systeem te maken in snelheidscoördinaten. De accretieschijf verschijnt op een dergelijk beeld als het ware binnenstebuiten gekeerd, omdat de hoogste snelheden kenmerkend zijn voor het materiaal dat het dichtst bij de witte dwerg roteert en de laagste snelheden voor het materiaal aan de buitenkant van de schijf.

De Doppler-afbeeldingen *(Doppler maps)* van de Balmerlijnen en de HeI- en HeII-lijnen vertonen zoals verwacht de begeleiderster en de accretieschijf. Op de Hγ- en HeI-afbeeldingen is bovendien een spiraalstructuur te zien in de accretieschijf. Deze structuur is, voor zover we weten, nooit eerder ontdekt in de schijf van een IP. Het fenomeen werd wel al waargenomen bij *dwarf novae* wanneer deze tijdelijk een zeer hoog massatransfer van de schijf naar de WD kennen *(outburst)* en bij nova-CVs *(novalike CVs)*. De spiraalarmen worden vermoedelijk veroorzaakt door getijdenkrachten van de begeleiderster op de buitenste delen van de accretieschijf rond de WD en kunnen voorkomen wanneer de accretieschijf groot genoeg is. De getijdenkrachten creëren in twee delen van de schijf een groter dan gemiddelde dichtheid en in twee delen daartussen een lager dan gemiddelde dichtheid, vergelijkbaar met het effect van de aantrekkingskracht van de maan op de oceanen op aarde. Wanneer het materiaal in de schijf richting de WD spiraleert, gaat het naar banen met een hogere Keplersnelheid, wat aanleiding geeft tot spiraalvormige dichtheidsstructuren in de schijf. Dergelijke spiraalstructuren zijn interessant omdat ze waarschijnlijk aanleiding kunnen geven tot transport van draaimoment doorheen de schijf, een proces dat nog niet goed begrepen is maar wel belangrijk is omdat het ook een cruciale rol speelt in bijvoorbeeld de schijven rond jonge sterren, waarin planeten gevormd worden. Nu spiraalstructuren gevonden zijn in de accretieschijf van DQ Her, beschikt men over een ideaal laboratorium om ze te bestuderen, aangezien de ster vrij lichtkrachtig is (B-magnitude van ongeveer 14) en omdat de structuur waarschijnlijk continu aanwezig, in tegenstelling tot bij de dwarf novae. Het vinden van de spiraalarmen bevestigt ook het resultaat van de simulaties van Murray et al. (1999) die voorspelden dat dergelijke spiraalstructuur aanwezig zou zijn in de accretieschijven van IPs. Spiraalarmen zouden de nevenfrequenties *(sidebands)* aan de spinfrequentie en omwentelingsfrequentie kunnen verklaren die dikwijls gevonden worden in X-stralen en optische lichtcurves van IPs. Eerdere conclusies dat deze afkomstig 'moeten' zijn van directe accretie (i.e. zonder inspiralering via de accretieschijf) moeten wellicht opnieuw bekeken worden (zie b.v. Norton et al. 1996 en Hellier 2007).

De HeII λ4686 afbeelding toont enkel een gevulde ring. Dit doet vermoeden dat de HeII-emissie deels afkomstig is van materiaal dat niet voldoet aan de Doppler tomografie-aanname van Kepleriaanse snelheden. Aangezien HeII-emissie een vrij hoge temperatuur vereist, is deze vooral afkomstig van het binnenste deel van de accretieschijf. Het recentste beeld van IPs voorspelt dat de materie accretiegordijnen *(accretion curtains)* vormt wanneer ze via de magnetische veldlijnen op de witte dwerg valt. Materiaal in deze accretiegordijnen heeft uiteraard snelheden die lang niet voldoen aan de veronderstelling van Keplersnelheden op circulaire banen. Een belangrijke emissiecomponent in deze gordijnen zou dus de 'gekke' Doppler-afbeelding kunnen verklaren.

In een poging om de aanstraling van de schijf door de X-stralenbundel van de witte dwerg te zien, werden ook Doppler-afbeeldingen gemaakt met enkel spectra die genomen werden van een gelijkaardige spinfase van de witte dwerg. Er konden echter geen noemenswaardige verschillen gedetecteerd worden tussen Doppler-afbeeldingen voor verschillende spinfases.

S.2.4 Variaties met een periode van 71s of 142s in de spectra van DQ Her

De lichtcurve van DQ Her vertoont variaties met een periode van 71s of 142s die afkomstig zijn van aanstraling van (delen van) de accretieschijf door de hoogenergetische stralenbundel van de witte dwerg die ontstaat door accretie van materiaal op de magnetische polen. Of de spinperiode van de witte dwerg 71s is, dan wel 142s, is niet geweten. De meeste fotometrische studies vinden geen signaal in het Fourierspectrum op 142s (zie bijvoorbeeld Kiplinger & Nather 1975; Wood et al. 2005). Dit maakt de 71s periode de meest waarschijnlijke, maar sluit de 142s periode niet volledig uit. Het is immers mogelijk om een signaal te verkrijgen met een periodiciteit van 71s van een systeem dat op 142s roteert, indien er twee (nagenoeg) identieke stralenbundels in het spel zijn. Fysisch gezien is het niet zo evident om de herkomst daarvan te verklaren, maar het is niet onmogelijk. Op basis van modellen van de lichtcurve tijdens eclipse besloten Zhang et al. (1995) wel dat 142s de meest waarschijnlijke spinperiode was, maar het geleverde bewijs is niet geheel overtuigend. Spectroscopische studies neigen in de richting van 71s maar sluiten 142s niet uit (Chanan et al. 1978; Martell et al. 1995). Recent claimden Saito & Baptista (2009) dat een periode van 142s niet mogelijk is en dat de 71s pulsatie in werkelijkheid overeenkomt met de beatperiode en dus niet met de spinperiode. Zij trokken deze conclusie op basis van *eclipse mapping*.

In de dataset die in dit werk gebruikt werd, werd geen signaal gedetecteerd op de 142s periode in het Fourier spectrum van de lijnflux van HeII λ4686. De 71s periodiciteit leidt wel tot een duidelijke piek. Door trails te bestuderen van de spectra, gevouwen op de 71s en 142s periodes, was het mogelijk om een beeld te krijgen van de snelheden van de componenten die aangestraald worden op verschillende spinfases. Een simpel model waarbij een kleine regio met een Kepleriaanse snelheid, aan de binnenkant van schijf, aangestraald wordt, komt het best overeen met de trails die gevouwen werden op de 142s periode. Het is echter niet mogelijk om op basis hiervan te claimen dat de echte spinperiode 142s moet zijn, omdat we in de vorige sectie reeds ontdekten dat een aanzienlijk deel van de straling (en dus mogelijkerwijs ook van de extra aanstraling) afkomstig is van materiaal dat niet op Keplerbanen beweegt, bv. van accretiegordijnen. Het is bijgevolg duidelijk dat het eenvoudige model sterk kan afwijken van de realiteit. We kunnen ook de observatie van Martell et al. (1995) bevestigen dat de aanstraling niet zichtbaar is in HeII λ4686 op blauwverschoven golflengten. Ook dit is niet te verklaren met een simpel model. Een meer uitgewerkt model is dus absoluut noodzakelijk om conclusies te kunnen trekken, en het is duidelijk dat spintrails een sterkere test vormen voor IP-modellen dan bv. fotometrische data.

De mogelijkheid dat de 71s periode eigenlijk de beatperiode is, kan op basis van onze dataset uitgesloten worden. Indien de meeste straling van de X-stralenbundels ons bereikt via de bright spot, dan zou de spinperiode 70.8s zijn en dan zou de aanstraling niet zichtbaar mogen zijn in bv. het roodverschoven stuk van de schijf op orbitale fases waarop de bright spot in het blauwverschoven deel van de schijf zit. Door spintrails te vergelijken voor

verschillende orbitale fases wordt het echter duidelijk dat de pulsaties continu zichtbaar zijn, ongeacht de orbitale fase waarin het systeem zich bevindt. Dit bewijst dat aanstraling van de bright spot niet de voornaamste oorzaak van de variaties in de lichtcurve kan zijn en dat de echte spinperiode niet 70.8s maar wel 71s of 142s is.

S.2.5 Het driedubbel gepiekte lijnprofiel van Hα

Bianchini et al. (2004) vonden componenten in de Hα-lijn die op alle orbitale fases dezelfde Dopplerverschuiving hebben. Deze stralingscomponenten kunnen bijgevolg niet afkomstig zijn van de dubbelster zelf, aangezien deze roteert rond haar massacentrum en dus tot variabele snelheden leidt. Uit de 2D-frames kunnen we afleiden dat deze lijnemissie afkomstig is van een expanderende schil *(nova shell)* die bij de nova in 1934 werd uitgestoten.

S.3 RXJ1730

S.3.1 Inleiding

De tweede ster die in dit werk besproken wordt, is 1RXS J173021.5-055933, ook gekend als RXJ1730. Deze werd vrij recent geïdentificeerd als IP (Gänsicke et al. 2005). Enkel geklopt door AE Aqr is het vandaag de dag van de gekende IPs diegene met de op één na extreemste verhouding tussen de orbitale periode (P_{orb} = 925.27 minuten) en de spinperiode (P_{spin} = 127.9999 seconden). AE Aqr is een zogenaamd *propellor* systeem, waarbij materiaal door het magnetisch veld van de witte dwerg eerder wordt weggeslingerd dan dat het op de witte dwerg terechtkomt. Deze speciale eigenschap van de IP die het meest op RXJ1730 gelijkt, is de motivatie om de ster te bestuderen aan de hand van hogesnelheidsspectroscopie.

S.3.2 De speurtocht naar fotonen van RXJ1730 met een L3CCD

RXJ1730 heeft een B-magnitude van 16.3, wat ongeveer 2 magnituden zwakker is dan DQ Her. Hogesnelheidsspectroscopie met een 4m-klasse telescoop zoals de WHT is bijgevolg niet evident, omdat het signaal bij korte integratietijden al snel zwakker wordt dan het ruisniveau. Daarom werd voor de observatie van RXJ1730 een L3CCD gebruikt, wat meteen ook het eerste gebruik van een dergelijke CCD was voor wetenschappelijke doeleinden op de WHT. Een L3CCD heeft een *frame transfer buffer* waarin een beeld tijdelijk kan worden opgeslagen, zodat het volgende beeld genomen kan worden terwijl het vorige nog wordt uitgelezen. Dit reduceert de tijd tussen twee observaties tot enkele milliseconden. De belangrijkste nieuwigheid van de L3CCDs is echter een elektronmultiplicatieregister waarin de elektronen die afkomstig zijn van invallende fotonen, vermenigvuldigd worden

alvorens het signaal uitgelezen wordt. Hierdoor wordt de ruis die bij het uitlezen wordt toegevoegd, verwaarloosbaar ten opzichte van het signaal, zelfs als er maar één foton in een pixel gedetecteerd werd.

Het nadeel van L3CCDs is dat de multiplicatie een stochastisch proces is. Het is met andere woorden niet eenduidig te bepalen hoeveel elektronen er na de multiplicatie aanwezig zullen zijn per initieel elektron. Het resultaat is dat de signaal tot ruis-verhouding met een factor twee daalt ten opzichte van een standaard CCD. Het feit dat de uitleesruis *(readout noise)* als het ware nul is, is echter veel belangrijker bij lage belichtingsniveaus. Zolang het aantal fotonen per pixel kleiner is dan het kwadraat van de uitleesruis, is een L3CCD in het voordeel.

Onze dataset bestond uit 13992 spectra genomen met de blauwe arm van de ISIS spectrograaf en 556 spectra genomen met de rode arm. De blauwe arm was uitgerust met een L3CCD, de rode met een standaard CCD. De integratietijd van de blauwe spectra was 1.4s tot 2s, die van de rode 32s tot 64s. De datareductie werd uitgevoerd met dezelfde software als deze gebruikt voor DQ Her. De reductie van de blauwe spectra was gecompliceerder dan bij DQ Her, omdat de belichting per beeld te zwak was om het spectrum precies te lokaliseren op de 2D-beelden. Toch was het nodig om de spectrumpositie steeds opnieuw te bepalen, omdat deze sterk van beeld tot beeld verschilde doordat de telescoop niet perfect uitgebalanceerd was. Daarom werd een strategie uitgewerkt waarbij de positie van het spectrum per beeld bepaald wordt aan de hand van de positie op een gesommeerd beeld van enkele honderden normale beelden, en de positie van de (niet-variabele en helderdere) referentiester die naast RXJ1730 in de spleet van de spectrograaf stond. Deze strategie zal nuttig zijn voor reductie van L3CCD-spectra in de toekomst, omdat deze steeds gekenmerkt zijn door een lage belichting.

De uiteindelijke 1D-spectra bevatten 3 tot 4 fotonen per seconde per ångström, wat ongeveer 30% minder is dan verwacht. Dit kan te wijten zijn aan groter dan voorziene slitverliezen *(slit losses)* als gevolg van de 'wiebelende' telescoop.

S.3.3 De baan van RXJ1730 en de spin van de witte dwerg

Een Fourier-getransformeerde van de continuümlichtcurve van de blauwe spectra vertoont duidelijke pieken op de spinfrequentie en de eerste harmonische. Als we het continuümniveau van de spectra aftrekken, is de variatie in tegenstelling tot bij DQ Her echter niet meer zichtbaar. Aangezien HeII λ4686 bij RXJ1730 intrinsiek 4 keer zwakker is dan bij DQ Her en de signaal tot ruis-verhouding van de RXJ1730-data 7 keer lager is, is dat niet erg verwonderlijk.

We kunnen in dit geval dus geen spintrails maken. Ook Doppler-tomografie is niet mogelijk, omdat de dekking van orbitale fases niet groot genoeg is door de lange orbitale periode van meer dan 15 uur. Wat we wel konden doen, is de amplitude van de radiale snelheden

(radial velocity amplitudes) van de twee sterren bepalen. We vonden $K_1 = 137 \pm 8$ km/s en $K_2 = 136 \pm 19$ km/s. Hieruit leiden we af dat de verhouding van de massa's van de twee sterren, $q = \frac{K_2}{K_1} = 0.99 \pm 0.15$, dicht bij 1 ligt, wat niet veel voorkomt. Veronderstellen we dat de sterren op circulaire banen bewegen dan kunnen we massa's van de twee componenten bepalen in functie van de inclinatie: $M_1 = (\sin^{-3} i) \cdot 0.67 \pm 0.12 M_\odot$ en $M_2 = (\sin^{-3} i) \cdot 0.67 \pm 0.08 M_\odot$. Met de schatting van de Martino et al. (2008) dat de inclinatie maximum 70° is, kunnen we besluiten dat de massa's van de twee sterren minstens $M_{1,min} = 0.81 \pm 0.15 M_\odot$ en $M_{2,min} = 0.81 \pm 0.10 M_\odot$ zijn. Aangezien een witte dwerg niet zwaarder kan zijn dan de Chandrasekhar massa ($M_{Ch} \approx 1.4 M_\odot$) is de inclinatie minstens 46°.

S.4 Conclusies

S.4.1 Het mysterieuze pulsatiepatroon en de spiraalarmen in de accretieschijf van DQ Her

Uit het onderzoek naar DQ Her kunnen we twee belangrijke besluiten trekken. Eerst en vooral hebben we spiraalstructuren waargenomen in de accretieschijf, wat de eerste detectie is van dergelijke spiraalarmen bij IPs. Spiraalarmen kunnen naar alle waarschijnlijkheid bijdragen tot het transport van draaimoment in de accretieschijf. Dit transport is nog niet goed begrepen, maar is een cruciaal aspect van de fysica van astrofysische schijven in het algemeen, bijvoorbeeld ook die rond jonge sterren en superzware zwarte gaten in quasars. Aangezien de spiraalstructuur in DQ Her waarschijnlijk continu zichtbaar is, in tegenstelling tot de spiralen bij dwarf novae, is DQ Her een zeer geschikt systeem om dit fenomeen verder te bestuderen. Daarnaast kunnen spiraalarmen een alternatieve verklaring geven voor de sideband variaties die dikwijls in optische en X-stralen lichtcurves gevonden worden. Eerdere conclusies dat dergelijke frequenties afkomstig zijn van directe accretie zonder inspiralering via een accretieschijf zijn dus niet noodzakelijk correct.

Een tweede belangrijk besluit van ons DQ Her-werk is dat accretiegordijnen zeer waarschijnlijk een belangrijke bijdrage leveren tot (de variatie in) de flux van HeII λ4686. Dit kunnen we afleiden uit de Doppler-afbeelding voor deze lijn en uit de spintrails. Voor zover we weten bestaat er vandaag de dag geen model voor IPs dat onze observaties kan verklaren. De spintrails zijn duidelijk een sterke test voor geavanceerdere modellen in de toekomst. De spintrails stellen ons ook in staat om de claim van Saito & Baptista (2009) dat de geobserveerde 71s periodiciteit overeenkomt met de beatperiode in plaats van de spinperiode, te verwerpen. De spinperiode is dus duidelijk 71s of 142s. Het gebrek aan een goed model weerhoudt ons ervan om tussen deze twee mogelijkheden te kiezen.

S.4.2 Gebruik van een L3CCD voor de observatie van de lichtzwakke dubbelster RXJ1730

Om hogesnelheidsspectroscopie van de lichtzwakkere IP RXJ1730 mogelijk te maken, werd een L3CCD gebruikt. Het was de eerste keer dat een L3CCD gebruikt werd voor wetenschappelijke waarnemingen in de William Herschel Telescoop. Tijdens de waarnemingen hadden we af te rekenen met een vervelend wiebelende telescoop, wat tot effect had dat de spectra bij opeenvolgende waarnemingen niet op dezelfde plaats op de CCD lagen. Omdat één spectrum van RXJ1730 niet genoeg fotonen bevatte om de positie van het spectrum nauwkeurig te bepalen, werd een nieuwe reductiestrategie ontworpen waarbij de positie bepaald werd met behulp van de lichtkrachtigere referentiester.

In tegenstelling tot bij DQ Her konden we geen lijnvariaties op de spinperiode detecteren. Dit is verklaarbaar door de 7 keer lagere signaal tot ruis-verhouding en 4 keer lagere lijnflux in vergelijking met DQ Her. Uit metingen van de radiale snelheden van de twee sterren kunnen we concluderen dat beide componenten van RXJ1730 ongeveer gelijke massa's hebben ($q = 0.99 \pm 0.15$), wat vrij uitzonderlijk is en nieuwe observaties in de toekomst rechtvaardigt. Uit het feit dat inclinatie maximaal 70° is, kunnen we afleiden dat de minimum massa's van de componenten $M_{1,min} = 0.81 \pm 0.15 M_{\odot}$ en $M_{2,min} = 0.81 \pm 0.10 M_{\odot}$ zijn.

De L3CCD presteerde goed. De reductiestrategie die we uitwerkten, laat toe om spectra van lichtzwakke objecten succesvol te reduceren. Intussen is ook de rode arm van de ISIS spectrograaf van de WHT uitgerust met een L3CCD, wat een waaier aan mogelijkheden opent voor hogesnelheidsspectroscopie in de toekomst.

Bibliography

Basden A. G., Haniff C. A., Mackay C. D., 2003, MNRAS, 345, 985

Berriman G., 1988, Observations of DQ HER stars, in Polarized Radiation of Circumstellar Origin. Vatican Observatory / University of Arizona Press, p. 281

Bianchini A., Mastrantonio E., Canterna R., Stute J., Cantrell K., 2004, A&A, 426, 669

Boffin H. M. J., 2001, in Boffin H. M. J., Steeghs D., Cuypers J., eds, Astrotomography, Indirect Imaging Methods in Observational Astronomy Vol. 573 of Lecture Notes in Physics, Berlin Springer Verlag, Spiral Waves in Accretion Discs - Theory. p. 69

Brunschweiger J., Greiner J., Ajello M., Osborne J., 2009, A&A, 496, 121

Butters O. W., Katajainen S., Norton A. J., Lehto H. J., Piirola V., 2009, A&A, 496, 891

Carroll B. W., Ostlie D. A., 2007, An introduction to modern astrophysics, 2nd edition. Addison-Wesley

Chanan G. A., Nelson J. E., Margon B., 1978, ApJ, 226, 963

Chester T. J., 1979, ApJ, 230, 167

Cordova F. A., Mason K. O., 1984, MNRAS, 206, 879

Cordova F. A., Mason K. O., Nelson J. E., 1981, ApJ, 245, 609

de Martino D., Matt G., Mukai K., Bonnet-Bidaud J.-M., Falanga M., Gänsicke B. T., Haberl F., Marsh T. R., Mouchet M., Littlefair S. P., Dhillon V., 2008, A&A, 481, 149

Downes R. A., Webbink R. F., Shara M. M., Ritter H., Kolb U., Duerbeck H. W., 2006, VizieR Online Data Catalog

Famaey B., Jorissen A., Luri X., Mayor M., Udry S., Dejonghe H., Turon C., 2005, A&A, 430, 165

Ferland G. J., 1980, The Observatory, 100, 166

Gänsicke B. T., Marsh T. R., Edge A., Rodríguez-Gil P., Steeghs D., Araujo-Betancor S., Harlaftis E., Giannakis O., Pyrzas S., Morales-Rueda L., Aungwerojwit A., 2005, MNRAS, 361, 141

Greenstein J. L., Kraft R. P., 1959, ApJ, 130, 99

Harrop-Allin M. K., Warner B., 1996, MNRAS, 279, 219

Hellier C., 1996, in Evans A., Wood J. H., eds, IAU Colloq. 158: Cataclysmic Variables and Related Objects Vol. 208 of Astrophysics and Space Science Library, The intermediate polars. p. 143

Hellier C., 2001, Cataclysmic Variable Stars. Springer-Praxis books in astronomy and space sciences

Hellier C., 2007, in Bouvier J., Appenzeller I., eds, IAU Symposium Vol. 243 of IAU Symposium, Disc magnetosphere interactions in cataclysmic variable stars. p. 325

Herbig G. H., Smak J. I., 1992, Acta Astronomica, 42, 17

Hilditch R. W., 2001, An Introduction to Close Binary Stars. Cambridge University Press

Horne K., 1986, PASP, 98, 609

Horne K., 1995, A&A, 297, 273

Horne K., Marsh T. R., 1986, MNRAS, 218, 761

Horne K., Welsh W. F., Wade R. A., 1993, ApJ, 410, 357

Hutchings J. B., Cowley A. P., Crampton D., 1979, ApJ, 232, 500

Iben I. J., Livio M., 1993, PASP, 105, 1373

Kemp J. C., Swedlund J. B., Wolstencroft R. D., 1974, ApJ, 193, L15

Kiplinger A. L., Nather R. E., 1975, Nature, 255, 125

Marsh T. R., 1989, PASP, 101, 1032

Marsh T. R., 2008, in Phelan D., Ryan O., Shearer A., eds, Astrophysics and Space Science Library Vol. 351 of Astrophysics and Space Science Library, High-Speed Optical Spectroscopy. p. 75

Marsh T. R., Horne K., 1988, MNRAS, 235, 269

Martell P. J., Horne K., Price C. M., Gomer R. H., 1995, ApJ, 448, 380

Mason P. A., 2004, in Tovmassian G., Sion E., eds, Revista Mexicana de Astronomia y Astrofisica Conference Series Vol. 20, On the Classification of Magnetic Cataclysmic Variables. pp 180–181

Mukai K., Still M., Ringwald F. A., 2003, ApJ, 594, 428

Murray J. R., Armitage P. J., Ferrario L., Wickramasinghe D. T., 1999, in Hellier C., Mukai K., eds, Annapolis Workshop on Magnetic Cataclysmic Variables Vol. 157 of

Astronomical Society of the Pacific Conference Series, Spiral waves and periodic accretion in intermediate polars. p. 25

Nather R. E., Warner B., 1969, MNRAS, 143, 145

Nelson M. R., 1975, ApJ, 196, L113

Norton A. J., Beardmore A. P., Taylor P., 1996, MNRAS, 280, 937

Norton A. J., Wynn G. A., Somerscales R. V., 2004, ApJ, 614, 349

Paczyński B., 1971, ARA&A, 9, 183

Patterson J., 1994, PASP, 106, 209

Patterson J., Robinson E. L., Nather R. E., 1978, ApJ, 224, 570

Petterson J. A., 1980, ApJ, 241, 247

Saito R. K., Baptista R., 2009, ApJ, 693, L16

Sawada K., Matsuda T., Hachisu I., 1986, MNRAS, 219, 75

Schenker K., King A. R., Kolb U., Wynn G. A., Zhang Z., 2002, MNRAS, 337, 1105

Schoembs R., Rebhan H., 1989, A&A, 224, 42

Shakura N. I., Syunyaev R. A., 1973, A&A, 24, 337

Silber A. D., Anderson S. F., Margon B., Downes R. A., 1996a, ApJ, 462, 428

Silber A. D., Anderson S. F., Margon B., Downes R. A., 1996b, AJ, 112, 1174

Steeghs D., 2001, in Boffin H. M. J., Steeghs D., Cuypers J., eds, Astrotomography, Indirect Imaging Methods in Observational Astronomy Vol. 573 of Lecture Notes in Physics, Berlin Springer Verlag, Spiral Waves in Accretion Discs - Observations. p. 45

Steeghs D., Harlaftis E. T., Horne K., 1997, MNRAS, 290, L28

Swedlund J. B., Kemp J. C., Wolstencroft R. D., 1974, ApJ, 193, L11

Tubbs R. N., 2003, PhD thesis, Cambridge University

Vaytet N. M. H., O'Brien T. J., Rushton A. P., 2007, MNRAS, 380, 175

Verbunt F., 1982, Space Science Reviews, 32, 379

Walker M. F., 1954, PASP, 66, 230

Walker M. F., 1956, ApJ, 123, 68

Walker M. F., 1958, ApJ, 127, 319

Warner B., 1995, Cataclysmic variable stars. Cambridge Astrophysics Series, Cambridge, New York: Cambridge University Press

Warner B., Peters W. L., Hubbard W. B., Nather R. E., 1972, MNRAS, 159, 321

Wood M. A., Robertson J. R., Simpson J. C., Kawaler S. D., O'Brien M. S., Nather R. E. e. a., 2005, ApJ, 634, 570

Zhang E., Robinson E. L., Stiening R. F., Horne K., 1995, ApJ, 454, 447